DESIGN AND CHARACTERIZATION OF COMPLIANT BACKPLATE HELMHOLTZ RESONATORS

By

STEPHEN BRIAN HOROWITZ

A THESIS PRESENTED TO THE GRADUATE SCHOOL
OF THE UNIVERSITY OF FLORIDA IN PARTIAL FULFILLMENT
OF THE REQUIREMENTS FOR THE DEGREE OF
MASTER OF SCIENCE

UNIVERSITY OF FLORIDA

2001

To my sweetie,
Liz

ACKNOWLEDGMENTS

Financial support for this project is provided by NASA Langley Research Center (Grant #NAG-1-2261) and is monitored by Dr. Michael G. Jones.

I would like to thank my advisors, Dr. Mark Sheplak and Dr. Toshikazu Nishida, for giving me some freedom in my research, while constantly pushing me to learn subjects until I own them. Their ideas and encouragement made this research possible. I would also like to thank Dr. Louis Cattafesta for his guidance and support throughout my research. Additionally, I am deeply indebted to all of my fellow students in the Interdisciplinary Microsystems Group, for their support and friendship.

Special thanks go to my family for always encouraging me to pursue my interests and for making that pursuit possible. Finally I would like to thank my fiancé, Megan Elizabeth Elliott, for her constant love and support.

TABLE OF CONTENTS

page

ACKNOWLEDGMENTS iv

LIST OF FIGURES vii

ABSTRACT xii

CHAPTERS

1 INTRODUCTION 1

Passive Acoustic Liners 1
Adaptive and Active Acoustic Liners 3
Other Work in the Field 3
Electromechanical Acoustic Liner 3

2 THEORETICAL BACKGROUND 6

Conventional Helmholtz Resonator 6
Lumped Element Model 6
Equivalent Circuit 10
Compliant-Backplate Helmholtz Resonator 11
Lumped Element Model 11
Equivalent Circuit 16
Mass Ratio Dependence of Coupled Resonant Frequencies 24

3 EXPERIMENTAL SETUP 28

Overview 28
Measurements and Equipment 28
Device Construction 33

4 EXPERIMENTAL RESULTS 37

Pressure Amplification 37
Helmholtz Resonator with Half-Inch Diameter, Clamped Backplates 37
Helmholtz Resonator with One-Inch Diameter, Clamped Backplates 47
Input Impedance 55
Helmholtz Resonator with Half-Inch Diameter, Clamped Backplates 55
Helmholtz Resonator with One-Inch Diameter, Clamped Backplates 61
Discussion of Results 68
Low-Frequency Mode Shapes 69

5 CONCLUSION 71
Summary of Results 71
Future Work 72
APPENDICES
A DRAWINGS 73
B MATHCAD CODE 76
LIST OF REFERENCES 79
BIOGRAPHICAL SKETCH 81

LIST OF FIGURES

Figure Page

1: Three conventional types of passive acoustic liners (Source: Motsinger and Kraft [1] pg. 167). 2

2: Single element of an electromechanical acoustic liner. 4

3: Diagram showing (a) side view and (b) top view of a conventional Helmholtz resonator. 7

4: Equivalent circuit representation of a conventional Helmholtz resonator. 11

5: (a) Magnitude and (b) phase of theoretical frequency response of a conventional Helmholtz resonator. 12

6: Diagram of a compliant backplate Helmholtz resonator. 12

7: Acoustical and mechanical equivalent circuit representation of a Helmholtz resonator with a compliant backplate 16

8: Equivalent acoustic circuit representation of a Helmholtz resonator with a compliant backplate. 19

9: Magnitude and phase of the theoretical pressure amplification of a compliant-backplate Helmholtz resonator with a 0.0015 in. thick, 0.5 in. diameter, aluminium backplate. 21

10: Contour plot of pressure amplification for various thickness of backplate. Bright areas are peaks in the frequency response, while dark areas are troughs. 22

11: Magnitude and phase of the theoretical, normalized input impedance of a compliant-backplate Helmholtz resonator 23

12: Theoretical normalized resistance and reactance of a compliant-backplate Helmholtz resonator. 23

13: Schematic of impedance tube terminated by compliant-backplate Helmholtz resonator. 29

14: Normal impedance tube showing rotating microphone plugs, and end-mounted Helmholtz resonator. 30

15: Photograph of the compliant backplate Helmholtz resonator showing compliant backplate clamped by circular clamping ring and incident and cavity microphone plugs. 34

16: Magnitude and phase of pressure amplification spectrum for Helmholtz resonator with 0.001 in., aluminum backplate clamped at 0.5 in. diameter. 39

17: Magnitude and phase of pressure amplification spectrum for Helmholtz resonator with 0.002 in., aluminum backplate clamped at 0.5 in. diameter. 40

18: Magnitude and phase of pressure amplification spectrum for Helmholtz resonator with 0.003 in., aluminum backplate clamped at 0.5 in. diameter. 40

19: Magnitude and phase of pressure amplification spectrum for Helmholtz resonator with 0.005 in., aluminum backplate clamped at 0.5 in. diameter. 41

20: Magnitude and phase of pressure amplification spectrum for Helmholtz resonator with 0.001 in., brass backplate clamped at 0.5 in. diameter. 41

21: Magnitude and phase of pressure amplification spectrum for Helmholtz resonator with 0.002 in., brass backplate clamped at 0.5 in. diameter. 42

22: Magnitude and phase of pressure amplification spectrum for Helmholtz resonator with 0.003 in., brass backplate clamped at 0.5 in. diameter. 42

23: Magnitude and phase of pressure amplification spectrum for Helmholtz resonator with 0.005 in., brass backplate clamped at 0.5 in. diameter. 43

24: Magnitude and phase of pressure amplification spectrum for Helmholtz resonator with 0.001 in., stainless steel backplate clamped at 0.5 in. diameter..... 43

25: Magnitude and phase of pressure amplification spectrum for Helmholtz resonator with 0.002 in., stainless steel backplate clamped at 0.5 in. diameter..... 44

26: Magnitude and phase of pressure amplification spectrum for Helmholtz resonator with 0.003 in., stainless steel backplate clamped at 0.5 in. diameter..... 44

27: Magnitude and phase of pressure amplification spectrum for Helmholtz resonator with 0.005 in., stainless steel backplate clamped at 0.5 in. diameter..... 45

28: Coherence between cavity and incident microphone for Helmholtz resonator with 0.001 in. thick aluminum backplate clamped at 0.5 in. diameter. 47

29: Coherence between cavity and incident microphone for Helmholtz resonator with 0.005 in. thick stainless steel backplate clamped at 0.5 in. diameter..... 47

30: Magnitude and phase of pressure amplification spectrum for Helmholtz resonator with 0.002 in., aluminum backplate clamped at 0.96 in. diameter. 48

31: Magnitude and phase of pressure amplification spectrum for Helmholtz resonator with 0.003 in., aluminum backplate clamped at 0.96 in. diameter. 49

32: Magnitude and phase of pressure amplification spectrum for Helmholtz resonator with 0.005 in., aluminum backplate clamped at 0.96 in. diameter. 49

33: Magnitude and phase of pressure amplification spectrum for Helmholtz resonator with 0.010 in., aluminum backplate clamped at 0.96 in. diameter. 50

34: Magnitude and phase of pressure amplification spectrum for Helmholtz resonator with 0.002 in., brass backplate clamped at 0.96 in. diameter. 50

35: Magnitude and phase of pressure amplification spectrum for Helmholtz resonator with 0.003 in., brass backplate clamped at 0.96 in. diameter. 51

36: Magnitude and phase of pressure amplification spectrum for Helmholtz resonator with 0.005 in., brass backplate clamped at 0.96 in. diameter. 51

37: Magnitude and phase of pressure amplification spectrum for Helmholtz resonator with 0.010 in., brass backplate clamped at 0.96 in. diameter. 52

38: Magnitude and phase of pressure amplification spectrum for Helmholtz resonator with 0.002 in., stainless steel backplate clamped at 0.96 in. diameter.....52

39: Magnitude and phase of pressure amplification spectrum for Helmholtz resonator with 0.003 in., stainless steel backplate clamped at 0.96 in. diameter.....53

40: Magnitude and phase of pressure amplification spectrum for Helmholtz resonator with 0.005 in., stainless steel backplate clamped at 0.96 in. diameter.....53

41: Magnitude and phase of pressure amplification spectrum for Helmholtz resonator with 0.010 in., stainless steel backplate clamped at 0.96 in. diameter.....54

42: Normalized resistance and reactance for Helmholtz resonator with 0.001 in. aluminum backplate clamped at 0.5 in. diameter.....55

43: Normalized resistance and reactance for Helmholtz resonator with 0.002 in., aluminum backplate clamped at 0.5 in. diameter.....56

44: Normalized resistance and reactance for Helmholtz resonator with 0.003 in., aluminum backplate clamped at 0.5 in. diameter.....56

45: Normalized resistance and reactance for Helmholtz resonator with 0.005 in., aluminum backplate clamped at 0.5 in. diameter.....57

46: Normalized resistance and reactance for Helmholtz resonator with 0.001 in., brass backplate clamped at 0.5 in. diameter. 57

47: Normalized resistance and reactance for Helmholtz resonator with 0.002 in., brass backplate clamped at 0.5 in. diameter. 58

48: Normalized resistance and reactance for Helmholtz resonator with 0.003 in., brass backplate clamped at 0.5 in. diameter. 58

49: Normalized resistance and reactance for Helmholtz resonator with 0.005 in., brass backplate clamped at 0.5 in. diameter. 59

50: Normalized resistance and reactance for Helmholtz resonator with 0.001 in., stainless steel backplate clamped at 0.5 in. diameter. 59

51: Normalized resistance and reactance for Helmholtz resonator with 0.002 in., stainless steel backplate clamped at 0.5 in. diameter. 60

52: Normalized resistance and reactance for Helmholtz resonator with 0.003 in., stainless steel backplate clamped at 0.5 in. diameter. 60

53: Normalized resistance and reactance for Helmholtz resonator with 0.005 in., stainless steel backplate clamped at 0.5 in. diameter. 61

54: Normalized resistance and reactance for Helmholtz resonator with 0.002 in. aluminum backplate clamped at 0.96 in. diameter 62

55: Normalized resistance and reactance for Helmholtz resonator with 0.003 in. aluminum backplate clamped at 0.96 in. diameter 62

56: Normalized resistance and reactance for Helmholtz resonator with 0.005 in. aluminum backplate clamped at 0.96 in. diameter 63

57: Normalized resistance and reactance for Helmholtz resonator with 0.010 in. aluminum backplate clamped at 0.96 in. diameter 63

58: Normalized resistance and reactance for Helmholtz resonator with 0.002 in. brass backplate clamped at 0.96 in. diameter. 64

59: Normalized resistance and reactance for Helmholtz resonator with 0.003 in. brass backplate clamped at 0.96 in. diameter. 64

60: Normalized resistance and reactance for Helmholtz resonator with 0.005 in. brass backplate clamped at 0.96 in. diameter. 65

61: Normalized resistance and reactance for Helmholtz resonator 0.010 in., brass backplate clamped at 0.96 in. diameter. 65

62: Normalized resistance and reactance for Helmholtz resonator with 0.002 in., stainless steel backplate clamped at 0.96 in. diameter. 66

63: Normalized resistance and reactance for Helmholtz resonator with 0.003 in., stainless steel backplate clamped at 0.96 in. diameter. 66

64: Normalized resistance and reactance for Helmholtz resonator with 0.005, stainless steel backplate clamped at 0.96 in. diameter. 67

65: Normalized resistance and reactance for Helmholtz resonator with 0.010 in., stainless steel backplate clamped at 0.96 in. diameter. 67

67: Measured mode shapes for each backplate along with a theoretical mode shape for a clamped circular plate, as given by Equation 2.10. 70

68 Schematic of neck and cavity plate for 0.5 in. diameter compliant backplate Helmholtz resonator. 73

69: Schematic of incident microphone (Left) and cavity microphone (Right). 73

70: Schematic of 0.5 in. clamping ring and placement of clamping ring with incident microphone.....74

71: Schematic of cavity plate for 0.96 in. diameter compliant backplate Helmholtz resonator. 74

72: Schematic of spacer ring, clamping ring, and placement of rings relative to incident microphone for 0.96 in. diameter compliant backplate Helmholtz resonator..75

Abstract of Thesis Presented to the Graduate School
of the University of Florida in Partial Fulfillment of the
Requirements for the Degree of Master of Science

DESIGN AND CHARACTERIZATION OF COMPLIANT BACKPLATE HELMHOLTZ RESONATORS

By

Stephen Brian Horowitz

August 2001

Chairman: Dr. Toshikazu Nishida
Cochairman: Dr. Mark Sheplak
Major Department: Electrical and Computer Engineering

To meet increasingly stringent government regulations on noise emitted from aircraft engines, improved methods are needed to reduce the level of noise emanating from aircraft engine nacelles. Noise suppression is achieved through appropriate impedance boundary conditions that reduce the propagation of engine noise. If the engine conditions change, a different impedance boundary condition is necessary to optimally suppress the noise. The ultimate goal of the research presented in this thesis is to design and build an in-situ, tunable-impedance, electromechanical acoustic liner to optimally suppress noise under changing engine conditions.

To further this end, an investigation was conducted into compliant-backplate Helmholtz resonators, which will later serve as fundamental components of the electromechanical acoustic liner. This thesis presents the analytical and experimental characterization of Helmholtz resonators using isotropic metal plates as a compliant

backplate. Lumped element models are developed and used to design a prototype Helmholtz resonator with a cavity backed by one of 24 different isotropic compliant backplates. Each configuration is then characterized from 1 kHz to 6.4 kHz in an impedance tube using pressure amplification and normal-incidence, acoustic impedance measurements. The experimental results demonstrate an additional resonance and an anti-resonance in the impedance caused by adding degrees-of-freedom to a conventional Helmholtz resonator. These extrema depend in part on the resonant frequency of the compliant backplate and can later be utilized for impedance tuning by using a piezoelectric-composite backplate in place of the isotropic backplates presented in this research. Overall, the results confirm the multi-degree of freedom nature of the compliant-backplate Helmholtz resonators and their equivalence to double-layer acoustic liners.

CHAPTER 1
INTRODUCTION

Noise suppression within aircraft engine ducts is necessary to meet government regulations that limit noise radiated from both commercial and private aircraft [1]. Suppression of noise is achieved by lining the engine duct with an appropriately designed acoustic liner. The acoustic liner is designed to provide an impedance boundary condition in the engine duct that reduces the propagation of engine noise through the duct.

Passive Acoustic Liners

Early designs focused on single layer, passive liners, that generally consist of a perforated faceplate and a rigid backplate, separated by a honeycomb structure [1], as shown in Figure 1a. These operate together as a conventional Helmholtz resonator, possessing a resonant frequency dependent upon the geometry of the faceplate holes and honeycomb shaped cavity. The noise-reduction bandwidth in single-layer liners is limited to one octave, which is tuned early in the design process to correspond to the blade passage frequency of the intended application [1].

To meet increasingly stringent government regulations, more advanced designs are necessary. Two approaches have generally been followed to achieve increased noise suppression. The first approach relies on improving passive liner technology, while the second approach uses adaptive techniques to allow for continued improvement in noise suppression.

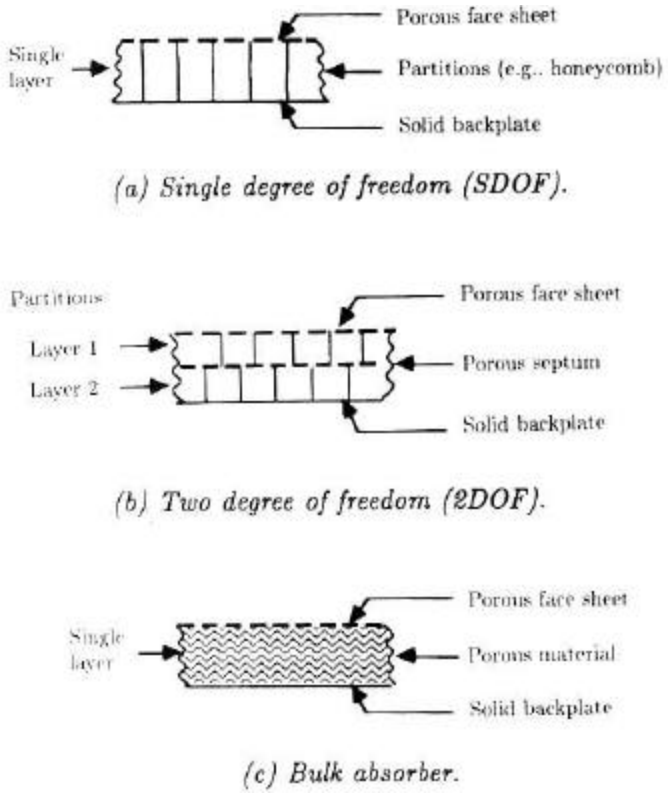

Figure 1: Three conventional types of passive acoustic liners (Source: Motsinger and Kraft [1] *pg. 167).*

Several techniques exist for increasing the attenuation bandwidth and level of maximum attenuation of passive acoustic liners, including parallel element and multi-layer liners. Multi-layer liners provide additional degrees of freedom that can be optimized to achieve a target impedance over a larger bandwidth than is possible with a single-layer [2]. A two-layer liner, as shown in Figure 1b for example, can achieve an attenuation bandwidth of about two octaves [1]. A third type of passive acoustic liner, known as a bulk absorber, contains a porous material in the cavity, as shown in Figure 1c. A bulk absorber offers the widest bandwidth attenuation of the passive techniques,

however it cannot be used in aircraft engine ducts due to high levels of jet fuel absorption by the porous material.

Once a passive acoustic liner is fabricated, the peak suppression frequency is fixed, and the bandwidth of effective attenuation is limited to one octave centered around the peak frequency. Changing engine conditions, such as at take-off and landing, pose a problem for optimization, since the optimum impedance spectrum may vary, but the liner impedance spectrum is fixed by the geometry of the design.

Adaptive and Active Acoustic Liners

Other Work in the Field

Various adaptive techniques have been investigated to modify the acoustic properties of liners for improved attenuation under changing engine conditions. One method uses a steady bias flow through the perforate faceplate to adjust the acoustic resistance [2-6]. A second method seeks to change the density near the liner via heating thereby controlling the resistance [2]. These techniques are adaptive and seek to improve the attenuation characteristics of a liner by directly modifying the impedance of one or more of the acoustic components of the liner. Another adaptive technique that has been investigated involves using a volume-variable cavity for a Helmholtz resonator [7, 8]. Other techniques seek to reduce noise by actively canceling the incident sound field with an out-of-phase, generated sound field [9].

Electromechanical Acoustic Liner

The liner presented in this thesis uses an alternative method of impedance tuning. The primary element of this liner is a Helmholtz resonator containing a compliant

piezoelectric composite backplate, as shown in Figure 2. The backplate provides acoustical-to-electrical transduction via the mechanical energy domain.

Figure 2: Single element of an electromechanical acoustic liner.

The impedance of this liner is not only a function of the acoustical components, but the mechanical and electrical components as well. While this complicates the impedance function, it provides an opportunity to tune the impedance by varying an electrical filter network. Additionally, more degrees of freedom are added to the system that can be optimized to improve the attenuation bandwidth. In fact, the impedance of this electromechanical acoustic liner takes on the same form and structure as existing multi-layer liners. The impedance of the basic electromechanical acoustic liner, with no electrical components connected, exactly parallels a double layer liner. In this liner, the aspects of the impedance typically caused by a second layer are instead due to mechanical components. Because of the piezoelectric transduction, this concept can be extended to provide as many degrees of freedom as desired, simply by adding an appropriate electrical network of inductors and capacitors across the electrodes of the piezoelectric material. Thus the benefits of multi-layer liners are achievable with electromechanical acoustic liners.

The impedance of the electromechanical acoustic liner can be tuned in-situ and in real-time. The initial goal is to have three distinct liner impedance spectra, each optimized for a specific engine condition, such as take-off, cut-back, and landing. This can be achieved with three separate electrical networks and a simple three-way switch to select the appropriate network.

In order to achieve this goal, a thorough understanding of the properties of an electromechanical acoustic liner is necessary. The fundamental element of this liner is a compliant-backplate Helmholtz resonator. In this thesis, the theoretical analysis of compliant-backplate Helmholtz resonators is developed and experimental verification of the concept is presented.

CHAPTER 2
THEORETICAL BACKGROUND

Understanding the influence of individual parameters of a given system is critical to efficient and accurate design. An intuitive and analytical understanding of the system is necessary to achieve the desired performance specifications. Furthermore, the design of an electromechanical acoustic liner presents a multi-domain modeling challenge.

Lumped element modeling provides an effective means of analyzing and designing a system involving multiple energy domains. Lumped element modeling has been used in the past for analysis of acoustic liners [10,11]. The convenience of lumped element modeling lies in the explicit relationship between individual design parameters and the frequency response of the system. Lumped element modeling must be used with care, to ensure that necessary assumptions are true. In particular, the wavelength of interest must be significantly larger than the characteristic length scale of the system, for the lumped assumption to be valid. When this criterion is met, the lumped element model is a reasonably accurate model of the distributed physical system. For the design and analysis of rigid and compliant-backplate Helmholtz resonators presented in this paper, lumped-element modeling is used extensively.

Conventional Helmholtz Resonator

Lumped Element Model

The dynamic response of a Helmholtz resonator can be conveniently modeled using an equivalent circuit representation. This representation relates mechanical and

acoustic quantities to their electrical equivalents. In circuit theory, distributed electrical parameters are lumped into specific components, based on how they interact with energy [12]. Using this criterion, a resistor represents dissipation of energy, while inductors and capacitors represent storage of kinetic and potential energy, respectively.

The techniques developed for circuit theory can be applied towards mechanical and acoustical systems by generalizing the fundamental circuit components [13,14]. A schematic diagram of a conventional Helmholtz resonator is shown below in Figure 3, where V is the cavity volume, L and S are the length and cross-sectional area of the neck, respectively, P_1 is the incident acoustic pressure, and P_2 is the cavity acoustic pressure. Both acoustic pressures are considered to be functions of the radian frequency, w.

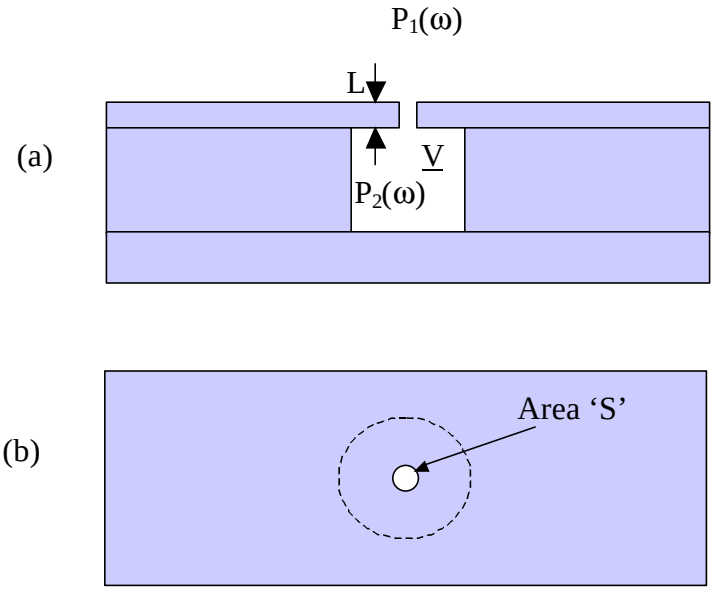

Figure 3: Diagram showing (a) side view and (b) top view of a conventional Helmholtz resonator.

A conventional Helmholtz resonator can be lumped into three distinct elements. The neck of the resonator constitutes a pipe through which frictional losses are incurred.

Additionally the air that is moving through the neck possesses a finite mass and thus kinetic energy. Thus the neck has both dissipative and inertial components. The air in the cavity is compressible and stores potential energy, and is therefore modeled as a compliance.

The acoustic compliance of the cavity and effective mass of the neck can be derived from first principles [11]. As mass flows into the bulb, the volume, *V*, remains constant and so the pressure must rise, by continuity of mass.

$$\frac{dM}{dt} = V\frac{d\,\rho_{air}}{dt} \equiv Q \rightarrow \text{ mass flow rate } \left[\frac{\text{kg}}{\text{s}}\right] \tag{2.1}$$

where *M* is the mass in the bulb and ρ_{air} is the density of the medium. If the disturbance is harmonic and isentropic then

$$P_2' = c^2\,\rho_{air} = \frac{c^2 Q}{j\omega V} \tag{2.2}$$

where *c* is the speed of sound of the medium, ω is the radian frequency, and $j = \sqrt{-1}$.

The linearized momentum equation for a lossless medium is given by

$$\rho_{air}\frac{\partial u}{\partial t} = -\nabla P'. \tag{2.3}$$

Assuming a linear pressure gradient yields

$$P_1' - P_2' = \rho_{air}\frac{\partial u}{\partial t}L, \tag{2.4}$$

where *L* is the length of the neck. Substituting for P_2' yields the following equation.

$$P_1' = \frac{Qc^2}{j\omega V} + \frac{Qj\omega L}{S}. \tag{2.5}$$

Defining the volumetric flow rate as

$$q = \frac{Q}{\rho_{air}}, \tag{2.6}$$

yields a relation between the effort P_1' and the flow q as shown below to be

$$P_1' = q\left(\frac{1}{jwC_a} + jwM_a \right). \tag{2.7}$$

In the above expression, the effective compliance C_a of the cavity is

$$C_a = \frac{V}{\rho_{air} c^2} \quad \left[\frac{m^3}{Pa} \right]. \tag{2.8}$$

The effective mass of the air in the neck is given by

$$M_a = \frac{4\rho_{air} L}{3S} \quad \left[\frac{kg}{m^4} \right]. \tag{2.9}$$

where L and S are the length and cross-sectional area of the neck, respectively.

The factor of 4/3 in the above expression for effective mass comes from a non-uniform axial velocity profile in the neck, due to viscous damping. The viscous damping represents a resistance, whose resistance can be approximated from pressure driven, laminar pipe flow as

$$R_a = \frac{8\pi\mu L}{S^2} \quad \left[\frac{kg}{m^4 s} \right]. \tag{2.10}$$

where μ is the viscosity of the air.

The effective resistance and mass values of the neck are, in fact, non-linear due to turbulence and entrance/exit effects [10]. These are a result of the high sound pressure levels present in the engine nacelle environment. In order to keep this analysis straightforward, these non-linear effects will be ignored in this thesis, along with any grazing flow dependence. The non-linear effects are small at the sound pressure levels, around 100 dBSPL, used in the experiments presented in this thesis [10].

The expression for cavity compliance given by (2.8) can be compared to an approximation based on the exact expression for the impedance in a short closed tube as given on page 149-50 of Blackstock [15]. The exact expression is given by

$$Z_{in} = \frac{\rho_{air} c}{j \tan kl} \tag{2.11}$$

where $k = \frac{\omega}{c}$, and l is then length of the tube. Using a Maclaurin series expansion of the tangent function yields

$$\tan kl = kl + \frac{1}{3}k^3 l^3 + \mathrm{L} \quad . \tag{2.12}$$

For kl << 1, the impedance can be approximated by keeping only the first couple of terms in the expansion, yielding

$$\begin{aligned} Z_{in} &= \frac{\rho_{air} c}{jkl\pi a^2} + j\frac{kl\,\rho_{air} c}{3\pi a^2} \\ &= \frac{\rho_{air} c^2}{j\omega V} + j\omega \frac{\rho_{air} V}{3\left(\pi a^2\right)^2} \end{aligned} \quad . \tag{2.13}$$

From this expression, we once again see that

$$C_a = \frac{V}{\rho_{air} c^2} \quad \left[\frac{m^3}{Pa}\right] \tag{2.14}$$

We now also have an additional mass term, given by

$$M_{cav} = \frac{\rho_{air} V}{3\left(\pi a^2\right)^2} \quad \left[\frac{\mathrm{kg}}{\mathrm{m}^4}\right] \tag{2.15}$$

which is equal to one-third the acoustic mass of the cavity. This correction term is small for kl = 1 but becomes more prominent as kl increases. At $kl = 1$, the correction term is 33.3% of the primary term.

Equivalent Circuit

To create an equivalent circuit model for the Helmholtz resonator, we also need to know how to connect these lumped elements. Connection rules between elements are defined based on whether an effort-type variable or a flow-type variable is shared between them. Whenever an effort variable, such as force, voltage or pressure, is shared between two or more elements, those elements are connected in parallel in the equivalent

circuit. Conversely, whenever a common flow (i.e., velocity, current, or volume velocity) is shared between elements, those elements are connected in series. These connection rules are used to obtain the equivalent circuit representation for the Helmholtz resonator, as shown in Figure 4.

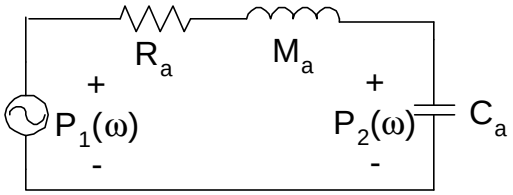

Figure 4: Equivalent circuit representation of a conventional Helmholtz resonator.

The frequency response function P_2/P_1, represents the pressure amplification of the resonator. It is the ratio of cavity pressure to incident pressure. From an analysis of the above circuit, a single resonant peak is expected in this frequency response function, when the sum of the reactances is zero, as is given by

$$f_{res} = \frac{1}{2\pi\sqrt{M_a C_a}} \tag{2.16}$$

This is shown in Figure 5, for a conventional Helmholtz resonator having a neck length and diameter of 3.18 *mm* and 4.72 *mm*, respectively, and a cavity volume of 1950 mm^3.

Compliant-Backplate Helmholtz Resonator

Lumped Element Model

In the analysis of the conventional Helmholtz resonator, it was implicitly assumed that the walls of the cavity were rigid. In the following analysis, the effect of a compliant wall in the cavity is examined. When one of the cavity walls is thin enough to flex under an applied pressure, as shown in Figure 6, the compliance and mass of the thin wall must

be accounted for to accurately model the system. This introduces two additional lumped elements.

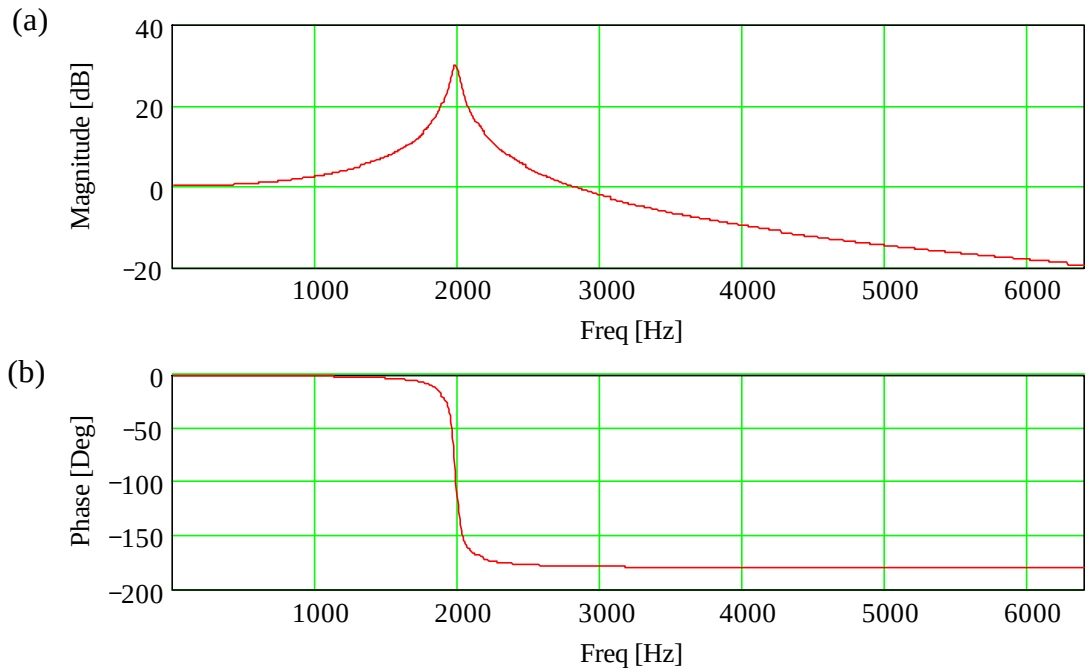

Figure 5: (a) Magnitude and (b) phase of theoretical frequency response of a conventional Helmholtz resonator.

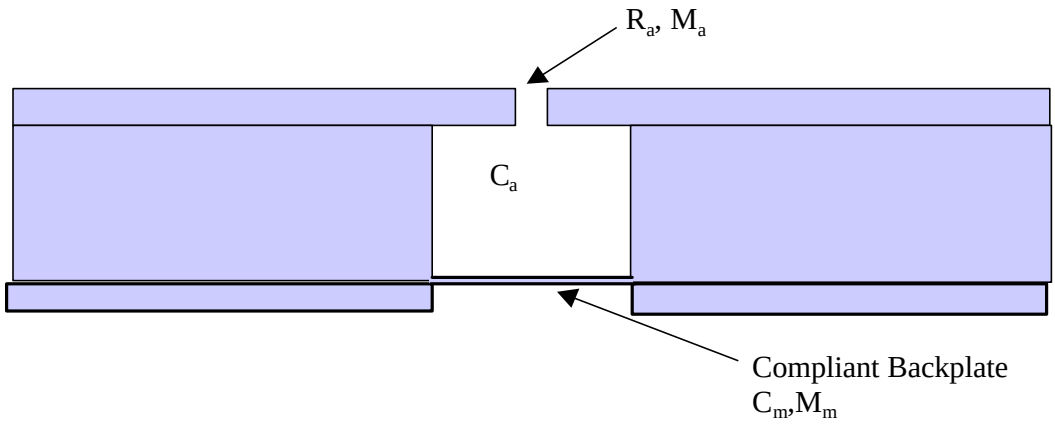

Figure 6: Diagram of a compliant backplate Helmholtz resonator.

By modeling the compliant backplate as a clamped circular plate, the lumped element parameters can then be derived. The physically distributed backplate is lumped into an equivalent mass and compliance at a single point in space. The center of the plate (i.e., where the radius, $r = 0$) is chosen as the point about which the system is lumped because of the circular geometry of the plate. The deflection of a clamped circular plate of radius, a, and thickness, h, under a uniform pressure P is given by [13]

$$w(r) = w_o\left(1-\left(\frac{r}{a}\right)^2\right)^2 \tag{2.17}$$

where the center deflection $w(0) = w_o$ is given by

$$w_o = \frac{Pa^4}{64D} \tag{2.18}$$

and D, the flexural rigidity, is defined as

$$D = \frac{Eh^3}{12\left(1-\boldsymbol{n}^2\right)} \tag{2.19}$$

Additionally, in (2.19), E is the elastic modulus, and $\boldsymbol{n}$ is the Poisson's ratio of the material. Similarly, the differential of the plate deflection is given by

$$dw(r) = \frac{\partial w(r)}{\partial w(0)}\partial w(0) = \left(1-\left(\frac{r}{a}\right)^2\right)^2 dw(0) \tag{2.20}$$

To find the effective compliance of the backplate, the potential energy stored in the backplate for a given displacement must first be calculated [13]. This can then be equated to the general expression for the potential energy in a spring, where the spring displacement is defined as the center deflection. The potential energy is then given by

$$W_{PE} = \frac{w(0)^2 k}{2} \tag{2.21}$$

where k is the spring stiffness.

From this relation, the effective stiffness, which is the inverse of the effective compliance, can be extracted. The potential energy stored in a differential element of the backplate is given by

$$dW_{PE} = Fdx = PdAdw(r) = P2\pi rdrdw(r) \tag{2.22}$$

where F is the force, and the pressure P can be found from (2.18) to be

$$P = \frac{64D}{a^4} w(0) \tag{2.23}$$

This yields a total potential energy of

$$\begin{aligned} W_{PE} &= \frac{128\pi D}{a^4} \int_0^{w(0)} \int_0^a rw(0)\left(1-\left(\frac{r}{a}\right)^2\right)^2 drdw(0) \\ &= \frac{128\pi D}{a^4} w(0)^2 \frac{1}{2} = \frac{1}{2}\frac{w(0)^2}{C_{me}} \end{aligned} \tag{2.24}$$

Thus the effective mechanical compliance of the backplate is found to be

$$C_{me} = \frac{3a^2}{64\pi D} = \frac{9a^2\left(1-\nu^2\right)}{16\pi Eh^3} \left[\frac{m}{N}\right] \tag{2.25}$$

A similar method is used to compute the effective mass of the compliant backplate [13]. Instead of finding the potential energy, however, the kinetic energy is computed and equated to

$$W_{KE} = \frac{1}{2} mu^2 \tag{2.26}$$

where u is the velocity of the backplate and for harmonic motion is given by

$$u(r) = j\omega w(r)\,. \tag{2.27}$$

The kinetic energy stored in a differential element of the plate is found to be

$$dW_{KE}^* = \frac{\rho h}{2} u(0)^2 \left(1-\left(\frac{r}{a}\right)^2\right)^4 2\pi rdr \tag{2.28}$$

Integrating this expression over the area of the plate yields the total kinetic energy, given by

$$W_{KE}^{*} = \frac{1}{2}\rho h u(0)^2 2\pi \int_0^a \left(1-\left(\frac{r}{a}\right)^2\right)^4 r\,dr$$
$$= \frac{1}{2}u(0)^2 \rho h\left(\frac{\pi a^2}{5}\right) \tag{2.29}$$

This yields an effective mechanical inertance of

$$M_{me} = \rho h\left(\frac{\pi a^2}{5}\right) = \frac{1}{5}M_{actual}\ \ [\mathrm{kg}]. \tag{2.30}$$

The effective mass of the compliant plate is therefore equivalent to 1/5th of the actual mass. Physically, this is due to the variation of deflection and hence kinetic energy over the radius of the circular plate.

In addition to the compliance and mass of the membrane, another element must now be included in the model. Since the clamped circular plate is vibrating in a medium, the radiation impedance of the plate must be taken into account. The circular plate will be modeled here as a piston in an infinite baffle, for the purposes of calculating a radiation impedance. The radiation impedance of a piston in an infinite baffle is given on page 459 of Blackstock [15] as

$$Z_p = \rho_{air} c\left[1-\frac{2J_1(2ka)}{2ka}+j\frac{2K_1(2ka)}{2ka}\right]$$
$$= \rho_{air} c\left[R_1(2ka)+jX_1(2ka)\right] \tag{2.31}$$

where $k=\frac{\omega}{c}$, a is the radius of the piston, J_1 is Bessel function of the first kind of order one, and K_1 is first-order Struve function. The Maclaurin expansions of (2.31) are also given by [15] as

$$R_1 = \frac{(ka)^2}{1\cdot 2}-\frac{(ka)^4}{1\cdot 2^2\cdot 3}+\frac{(ka)^6}{1\cdot 2^2\cdot 3^2\cdot 4}\mathrm{L} \tag{2.32}$$

$$X_1 = \frac{4}{\pi}\left[\frac{2ka}{3}-\frac{(2ka)^3}{3^2\cdot 5}+\frac{(2ka)^5}{3^2\cdot 5^2\cdot 7}\mathrm{L}\ \right]. \tag{2.33}$$

Under a low frequency approximation (ka <<1), only the first terms in each series are kept, and a lumped radiation resistance and mass are given, respectively, in the acoustic domain as

$$R_{rad} = \frac{(ka)^2}{2} \cdot \frac{\rho_{air} c}{\pi a^2} \left[\frac{kg}{m^4 s}\right] = \frac{k^2 \rho_{air} c}{2\pi} \left[\frac{kg}{m^4 s}\right] \tag{2.34}$$

and

$$M_{rad} = \frac{8a}{3\pi c} \cdot \frac{\rho_{air} c}{\pi a^2} \left[\frac{kg}{m^4}\right] = \frac{8\rho_{air}}{3\pi^2 a} \left[\frac{kg}{m^4}\right]. \tag{2.35}$$

Equivalent Circuit

The two mechanical lumped elements can easily be incorporated into the overall equivalent circuit. The new elements are in series with each other because they both are subject to the same motion. Additionally, the series combination of these two elements is in parallel with the acoustic compliance. A portion of the flow entering the cavity through the neck of the resonator will contribute to an increase in cavity pressure, while the remainder of the flow contributes to the motion of the compliant backplate.

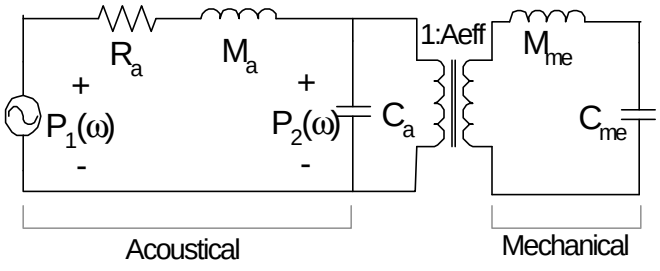

Figure 7: Acoustical and mechanical equivalent circuit representation of a Helmholtz resonator with a compliant backplate

The equivalent circuit in Figure 7 shows the additional mechanical lumped elements that appear in a compliant backplate Helmholtz resonator. Also, an acoustical to mechanical transduction factor is necessary to account for the transduction of acoustical energy to mechanical energy and vice-versa. The acoustical to mechanical transduction factor can be defined as the effective area through which the transduction occurs, and is given by

$$A_{eff} = \frac{F}{P} \tag{2.36}$$

where P is the pressure applied and F is the equivalent force. This is represented by a transformer with the turns ratio given by A_{eff}. For a lumped mechanical spring the force is related to the displacement by

$$F = Kx \tag{2.37}$$

The spring stiffness, K, is the inverse of the spring compliance, C. For a clamped circular plate, the compliance was found to be

$$C_{me} = \frac{3a^2}{64\pi D} \tag{2.38}$$

The circular plate is lumped about its center, therefore the displacement indicated in (2.37) represents the center deflection of the plate. The center deflection of the plate is given by

$$x(0) = \frac{Pa^4}{64D} \tag{2.39}$$

Substituting (2.38) and (2.39) into (2.37) yields

$$\begin{aligned} F &= \frac{Pa^4}{64D}\frac{64\pi D}{3a^2} = \frac{1}{3}\pi a^2 P \\ &= \frac{1}{3} Area * P \end{aligned} \tag{2.40}$$

The effective area is then given by

$$A_{eff} = \frac{1}{3} Area \tag{2.41}$$

for a clamped circular plate.

Another method can be used for determining the effective area. This method relies on conservation of volume velocity. Volume velocity, for any acousto-mechanical interface, is defined as [13]

$$Q = \int v_n dS \tag{2.42}$$

where v_n is the velocity normal to the surface.

For a clamped circular plate, (2.42) can be written as

$$\begin{aligned} Q &= \int_0^a \omega x(0) \left[1 - \left(\frac{r}{a} \right)^2 \right]^2 2\pi r dr \\ &= \frac{1}{3} \pi a^2 \omega x(0) \\ &= \frac{1}{3} Area * v(0) \end{aligned} \tag{2.43}$$

where *v(0)* is the velocity at the center of the plate.

For a piston, the volume velocity relationship to velocity is given by

$$Q = v * Area \tag{2.44}$$

Since the plate is lumped as a rigid piston moving at velocity *v(0)*, the volume velocity of the plate can be written as

$$Q = A_{eff} v(0) \tag{2.45}$$

where

$$A_{eff} = \frac{1}{3} Area \tag{2.46}$$

As expected, either method produces the same transduction factor. Therefore, in addition to lumping a clamped circular plate as a rigid piston attached to a spring, the area of transduction must be reduced by a factor of three to account for the effective transduction of pressure to force, or velocity to volume-velocity that is actually taking

place. Physically, this factor is because the plate does not deflect like a piston, since it is clamped at the edges. The pressure near the edges does not create as effective of a deflection-causing force as the pressure at the center. Similarly, the total volume velocity is reduced when compared to the piston of equal area moving with a velocity equal to the center velocity of the plate.

The equivalent circuit shown in Figure 8 is defined strictly in terms of acoustical parameters. The representation of the mechanical inertance and compliance of the backplate in the acoustical energy domain requires use of the transduction factor, given by the squared magnitude of the effective backplate area, A_{eff} [13]. The transduction factor is needed for conservation of energy when an impedance is reflected from one energy domain into another.

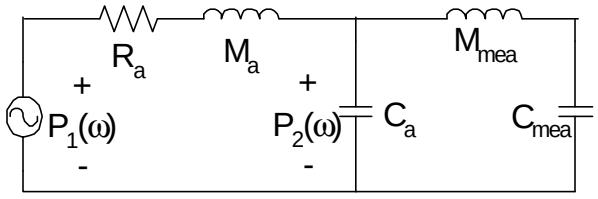

Figure 8: Equivalent acoustic circuit representation of a Helmholtz resonator with a compliant backplate.

The transduction of impedance from the mechanical to acoustical energy domain is given by

$$Z_a = \frac{Z_m}{A_{eff}^{\ 2}}. \tag{2.47}$$

The acoustical equivalent circuit elements of the mechanical inertance and compliance are given by

$$M_{mea} = \frac{M_{me}}{A_{eff}^{\ 2}} \tag{2.48}$$

$$C_{mea} = C_{me} A_{eff}^{\ 2}. \tag{2.49}$$

This relationship between the acoustical and mechanical energy domains is evident via a dimensional analysis of the two energy domains.

Relating the effective mass and compliance to their acoustical representations yields the following expressions for the effective mass and compliance of the backplate, in the acoustical energy domain.

$$M_{mea} = \left(\frac{\rho a^2 \rho h}{5 A_{eff}^{\ 2}} \right) \tag{2.50}$$

$$C_{mea} = \frac{9a^2 \left(1 - \nu^2\right) A_{eff}^{\ 2}}{16 \pi E h^3} \tag{2.51}$$

The transfer function of the cavity pressure to the incident pressure is now given by

$$\frac{P_2}{P_1} = \frac{\dfrac{s^2 M_{mea} C_{mea} + 1}{s\left(C_{mea} + s^2 M_{mea} C_{mea} C_a + C_a\right)}}{R_a + s M_a + \dfrac{s^2 M_{mea} C_{mea} + 1}{s\left(C_{mea} + s^2 M_{mea} C_{mea} C_a + C_a\right)}} \tag{2.52}$$

From this expression, the anti-resonance, which occurs at the frequency at which the numerator equals zero, is dependent only upon the effective mass and compliance of the backplate. This makes physical sense, as the anti-resonance of this transfer function is due to the mechanical resonance of the backplate that prevents sound pressure from building up in the cavity.

For a Helmholtz resonator with a compliant backplate consisting of an aluminum shim with 1 mil thickness, but otherwise identical in geometry to the conventional Helmholtz resonator described earlier, a frequency response function is obtained similar

to the one shown in Figure 9. The frequency response shows two resonant peaks separated by an anti-resonance.

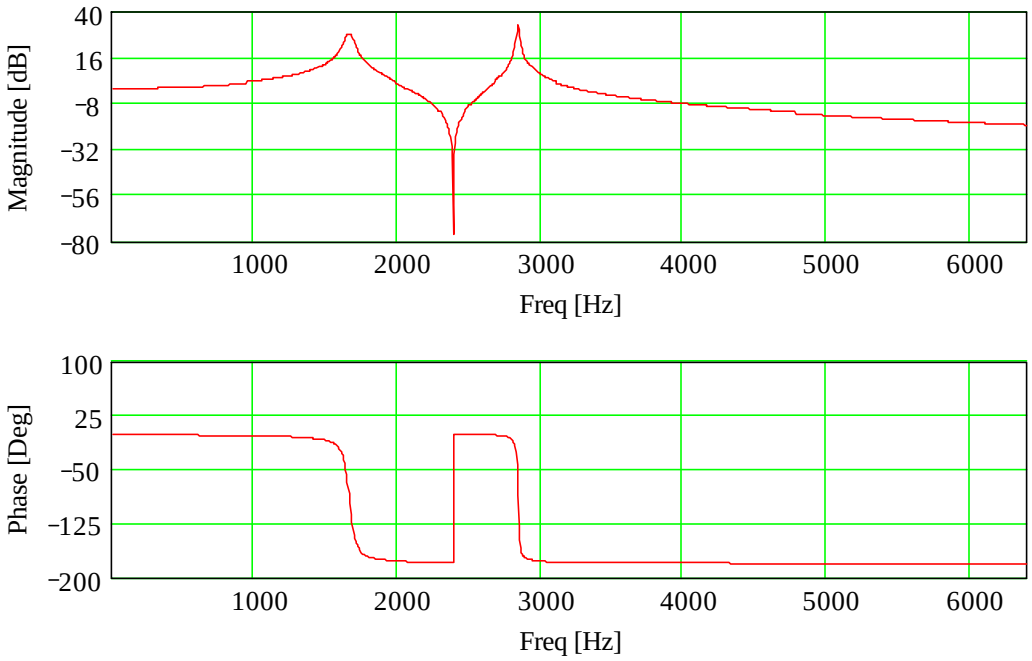

Figure 9: Magnitude and phase of the theoretical pressure amplification of a compliant-backplate Helmholtz resonator with a 0.0015 in. thick, 0.5 in. diameter, aluminium backplate.

The frequency response depends upon the thickness and radius of the backplate. Shown in Figure 10 is a contour plot displaying the effect of varying the thickness on the frequency response. The anti-resonance can be seen to vary linearly with the backplate thickness. Additionally, for thick backplates, shown near the top of the plot, the second resonance depends more on the mechanical properties of the backplate and also varies linearly with thickness, while the first resonance is primarily due to the acoustic elements of the system and does not vary much with thickness. As the thickness is decreased to where the anti-resonance approaches the first resonance, stronger coupling occurs

between the mechanical and acoustical elements, leading to a variation in both resonant frequencies with decreasing thickness.

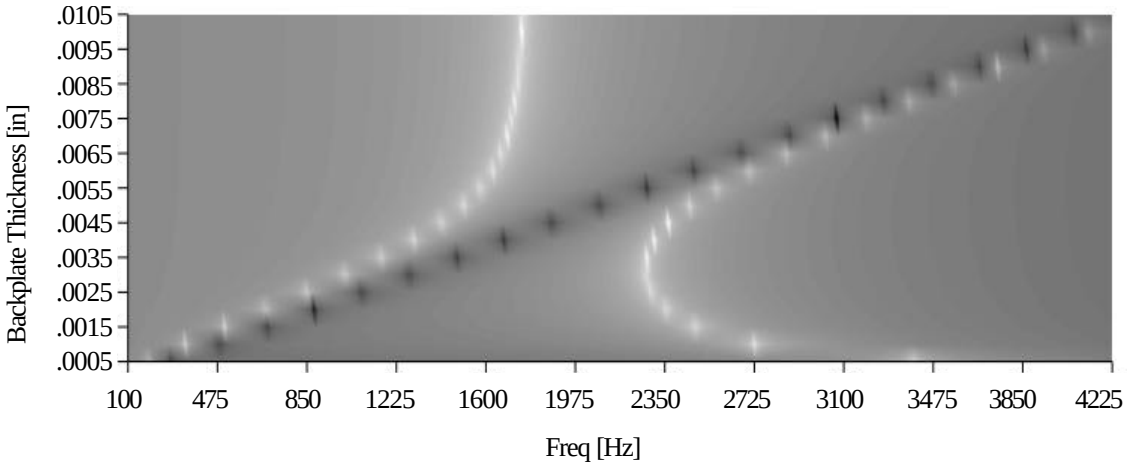

Figure 10: Contour plot of pressure amplification for various thickness of backplate. Bright areas are peaks in the frequency response, while dark areas are troughs.

The input impedance of the compliant-backplate Helmholtz resonator is given by,

$$Z_a = \frac{\left(sM_{mea} + \frac{1}{sC_{mea}}\right)\frac{1}{sC_a}}{sM_{mea} + \frac{1}{sC_{mea}} + \frac{1}{sC_a}} + sM_a + R_a \qquad (2.53)$$

This expression, which can be derived directly from the equivalent circuit, results from a series combination of the backplate mass and compliance in parallel with the cavity compliance and all in series with the mass and resistance of the neck. A plot of the magnitude and phase of the input impedance for a 0.0017 in. thick backplate is shown below in Figure 11. The impedance is also shown in terms of resistance and reactance in Figure 12. In the plot, the acoustic input impedance is multiplied by the area of the neck A_n to yield the specific acoustic impedance, and is then normalized by ρc to yield a non-dimensional result.

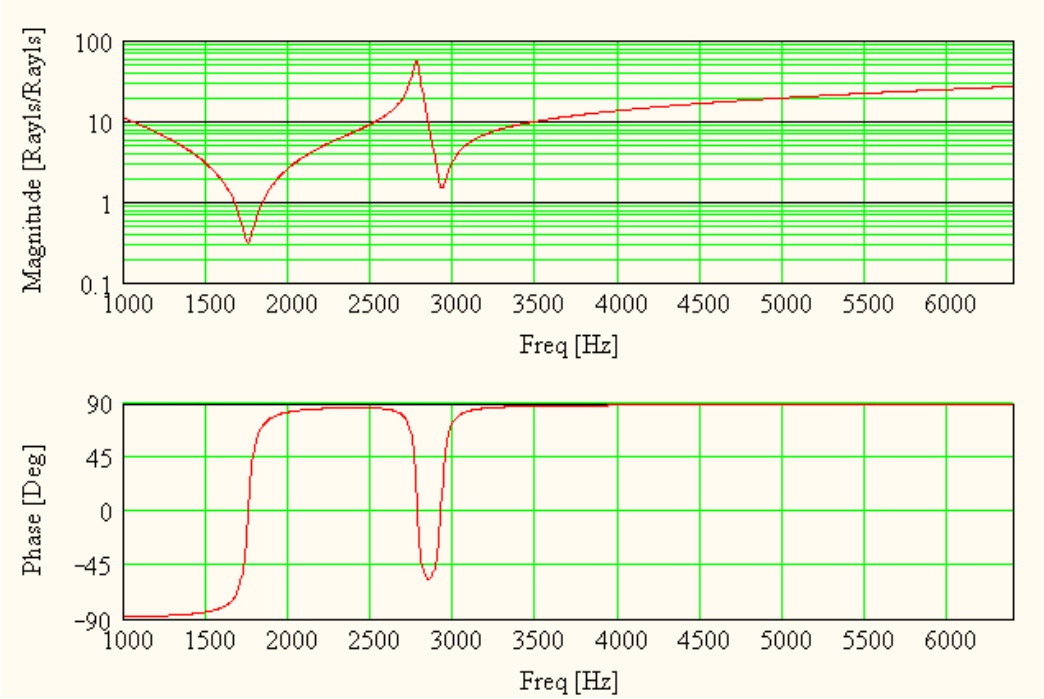

Figure 11: Magnitude and phase of the theoretical, normalized input impedance of a compliant-backplate Helmholtz resonator.

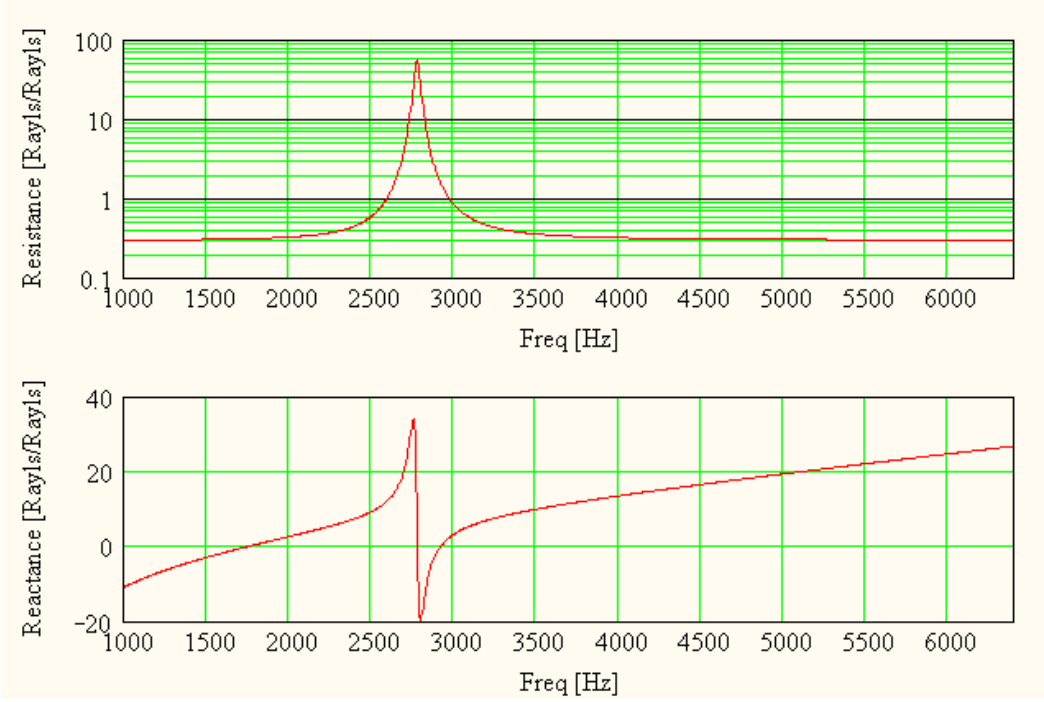

Figure 12: Theoretical normalized resistance and reactance of a compliant-backplate Helmholtz resonator.

As can be seen in Figure 11 and Figure 12, there are two resonances in the impedance. At these frequencies, the magnitude tends towards the value of the resistance, since the phase goes to zero and the impedance is then purely resistive. Note that resonant frequencies, in this thesis, refer to the frequencies at which the reactance goes to zero. This corresponds to minima on an impedance plot. A pressure amplification plot, however, indicates the acoustic response of the system, and therefore maxima are labeled as the resonant frequencies.

In the impedance plot of Figure 11, an anti-resonance occurs between the two resonant frequencies. It should be noted that, due to the topology of the circuit, this anti-resonance does not coincide with the anti-resonance present in the transfer function of the cavity to incident SPL. This can be understood by looking at the expression for the input impedance (2.53) at the frequency at which the anti-resonance is seen in the transfer function of the cavity to incident SPL. The transfer function heads toward zero at this point because the reactance of the backplate, which is in parallel with the cavity compliance heads toward zero. The total input impedance, however, does not become purely resistive at this point, because of the mass of the neck. Instead, the anti-resonance of the impedance occurs at a higher frequency, where the parallel combination of the backplate impedance and the cavity compliance cancels the reactance of the mass in the neck.

Mass Ratio Dependence of Coupled Resonant Frequencies

In the compliant backplate Helmholtz resonator, there are two resonant frequencies, separated by an anti-resonance. The analytical expression for the two resonances are too complex to provide much insight in general; however, when the

mechanical resonance is matched to the acoustical resonance, the analytical expression can be greatly simplified, leading to a useful expression.

Analytical expressions for the two resonances can be found by looking at the input impedance, and solving for the frequencies at which it equals zero. As originally given in (2.53) and repeated here for convenience, the input impedance to the compliant backplate Helmholtz resonator is given by

$$Z_a = \frac{\left(sM_{mea} + \frac{1}{sC_{mea}}\right)\frac{1}{sC_a}}{sM_{mea} + \frac{1}{sC_{mea}} + \frac{1}{sC_a}} + sM_a + R_a \tag{2.54}$$

which can be simplified to

$$Z_a = \frac{1}{s}\frac{\left(s^4 M_a C_a M_{mea} C_{mea} + s^2 M_{mea} C_{mea} + s^2 M_a C_a + s^2 M_a C_m + 1\right)}{\left(s^2 M_{mea} C_{mea} C_a + C_a + C_{mea}\right)} \tag{2.55}$$

The anti-resonant frequency, which occurs when the denominator approaches zero, is given by

$$f_{ar} = \frac{1}{2\pi}\frac{1}{M_{mea} C_{mea} C_a}\sqrt{M_{mea} C_{mea} C_a \left(C_a + C_{mea}\right)} \tag{2.56}$$

The two resonant frequencies occur when the numerator approaches zero, and are given by

$$f_{res1} = \frac{1}{2\pi}\frac{1}{2M_a M_{mea} C_a C_{mea}}\left\{2M_a M_{mea} C_a C_{mea}\left[\begin{array}{l} M_{mea} C_{mea} + M_a C_a + M_a C_{mea} - \\ \left(M_{mea}{}^2 C_{mea}{}^2 - 2M_a M_{mea} C_a C_{mea} + \right. \\ \left. 2M_{mea} C_{mea}{}^2 M_a + M_a{}^2 C_a{}^2 + \right. \\ \left. 2M_a{}^2 C_a C_{mea} + M_a{}^2 C_{mea}{}^2\right)^{\frac{1}{2}} \end{array}\right]\right\}^{\frac{1}{2}} \tag{2.57}$$

and

$$f_{res2} = \frac{1}{2\pi}\frac{1}{2M_a M_{mea} C_a C_{mea}}\left\{2M_a M_{mea} C_a C_{mea}\left[\begin{array}{l} M_{mea}C_{mea} + M_a C_a + M_a C_{mea} + \\ \left(\begin{array}{l} {M_{mea}}^2 {C_{mea}}^2 - 2M_a M_{mea} C_a C_{mea} + \\ 2M_{mea}{C_{mea}}^2 M_a + {M_a}^2 {C_a}^2 + \\ 2{M_a}^2 C_a C_{mea} + {M_a}^2 {C_{mea}}^2 \end{array}\right)^{\frac{1}{2}} \end{array}\right]\right\}^{\frac{1}{2}} \quad (2.58)$$

These expressions do not provide much insight into the dependence of the resonant frequencies on the various parameters. However, for a system in which the uncoupled resonant frequency of the mechanical components matches the uncoupled resonant frequency of the acoustical components, these expressions can be greatly simplified. The matched uncoupled resonant frequencies are given by

$$f_{resA} = \frac{1}{2\pi\sqrt{M_a C_a}} = f_{resM} = \frac{1}{2\pi\sqrt{M_{mea} C_{mea}}} \quad (2.59)$$

which yields a relationship between the acoustical and mechanical components of

$$M_{mea} C_{mea} = M_a C_a \quad (2.60)$$

Substituting this equality into (2.57) and (2.58) greatly simplifies the expressions for the two resonant frequencies, which can be shown to be

$$f_{res1} = \frac{1}{2\pi}\frac{1}{2M_a C_a}\left\{2M_a\left[2C_a + C_{mea} - \left(4C_a C_{mea} + {C_{mea}}^2\right)^{\frac{1}{2}}\right]\right\}^{\frac{1}{2}} \quad (2.61)$$

and

$$f_{res2} = \frac{1}{2\pi}\frac{1}{2M_a C_a}\left\{2M_a\left[2C_a + C_{mea} + \left(4C_a C_{mea} + {C_{mea}}^2\right)^{\frac{1}{2}}\right]\right\}^{\frac{1}{2}} \quad (2.62)$$

Furthermore, we can define a mass ratio, α, that relates the acoustical to mechanical mass, as well as the mechanical to acoustical compliance.

$$\alpha = \frac{M_a}{M_{mea}} = \frac{C_{mea}}{C_a} \quad (2.63)$$

Making appropriate substitutions, (2.61) and (2.62) can be expressed in terms of the mass ratio as

$$f_{\text{res1}} = \frac{f_0}{\sqrt{2}}\left\{2+\alpha-\left[4\alpha+\alpha^2\right]^{\frac{1}{2}}\right\}^{\frac{1}{2}} \tag{2.64}$$

and

$$f_{\text{res2}} = \frac{f_0}{\sqrt{2}}\left\{2+\alpha+\left[4\alpha+\alpha^2\right]^{\frac{1}{2}}\right\}^{\frac{1}{2}} \tag{2.65}$$

where f_0 is the original uncoupled resonant frequency of each subsystem, given by

$$f_0 = f_{resA} = f_{resM} \tag{2.66}$$

From the above expressions, it is now evident that the resonant frequencies can be expressed solely as a function of the original resonant frequency and the mass ratio, alpha. Furthermore, the bandwidth between these two resonant frequencies is given by

$$\begin{aligned} f_{res2} - f_{res1} &= \frac{f_0}{\sqrt{2}}\left\{2+\alpha+\left[4\alpha+\alpha^2\right]^{\frac{1}{2}}\right\}^{\frac{1}{2}} - \frac{f_0}{\sqrt{2}}\left\{2+\alpha-\left[4\alpha+\alpha^2\right]^{\frac{1}{2}}\right\}^{\frac{1}{2}} \\ &= f_0\sqrt{\alpha} \end{aligned} \tag{2.67}$$

Although desirable from an analytical perspective, the condition of matched uncoupled resonance is necessary for this simplification. Most of the designs tested in this thesis do not have uncoupled resonance frequencies that match or are close to matching.

Additionally, by using the mass ratio, α, the expression for the anti-resonance can also be simplified, as shown below. If the resonances are not matched, this expression can still be used, however α would then only equal the compliance ratio, rather than both ratios.

$$\begin{aligned} f_{ar} &= f_{resM}\left(1+\frac{C_{mea}}{C_a}\right)^{\frac{1}{2}} \\ &= f_0\sqrt{1+\alpha} \end{aligned} \tag{2.68}$$

CHAPTER 3
EXPERIMENTAL SETUP

Overview

After developing the lumped element models used to predict frequency response and input impedance, experiments were designed to provide verification of the models. The verification is necessary as a first experimental step in order to demonstrate the validity of the modeling. Initial verification was provided through the pressure amplification frequency response function, which is a quick, easy measurement to perform. Furthermore, in order to validate the assumption that the compliant backplate behaves as a clamped circular plate, additional experiments were performed to measure the mode shape.

After verification of the models, further characterization was performed through measurement of the acoustic input impedance to the resonator. When the compliant backplate Helmholtz resonator is later implemented as part of an electromechanical acoustic liner, the impedance will be important in predicting the liner's effect on the propagation of noise through an aircraft engine duct.

Measurements and Equipment

Characterization of the compliant backplate Helmholtz resonator was conducted at the Interdisciplinary Microsystems Laboratory at the University of Florida. Twenty-four different compliant-backplate Helmholtz resonators were tested in a normal incidence impedance tube. The impedance tube consists of a 38 in. long, 1 in. by 1 in.

square duct, which permits characterization in a known, plane wave acoustic field at frequencies up to 6.7 kHz.

Input impedance and pressure amplification measurements were taken for the compliant-backplate Helmholtz resonator for a range of backplate thicknesses, radii, and materials. Additionally, low frequency mode shapes were measured for some of the backplates using laser vibrometry. For each set of measurements, the resonator was mounted flush to the end of the impedance tube, as shown in Figure 13. This setup permits simultaneous measurements of resonator impedance, pressure amplification and mode shape, although the mode shape data was actually collected at a later time.

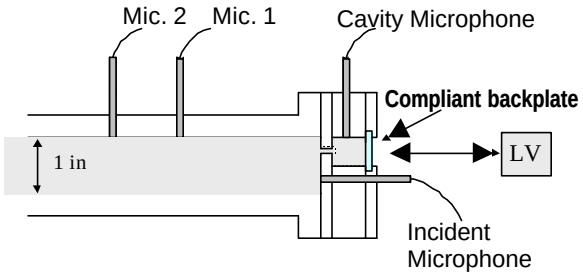

Figure 13: Schematic of impedance tube terminated by compliant-backplate Helmholtz resonator.

Four Bruel and Kjær (B&K) type 4138 microphones were used for simultaneous acoustic pressure measurements. Two microphones were flush mounted, in a rotating plug, to the side of the impedance tube, as shown in Figure 14. The plug allowed for convenient microphone switching between impedance measurements to average out any amplitude or phase calibration differences between the microphones [17]. The other two microphones were used to measure the pressure amplification frequency response function. One microphone was flush mounted in the side wall of the resonator cavity to measure the cavity pressure. The second microphone was flush mounted to the end face

of the impedance tube to measure the acoustic pressure incident to the resonator. This microphone also served as a reference to ensure a nearly constant SPL, with respect to frequency, at the neck of the resonator for each backplate configuration. The pressure amplification frequency response function was then obtained as the ratio of cavity to incident acoustic pressure as a function of frequency.

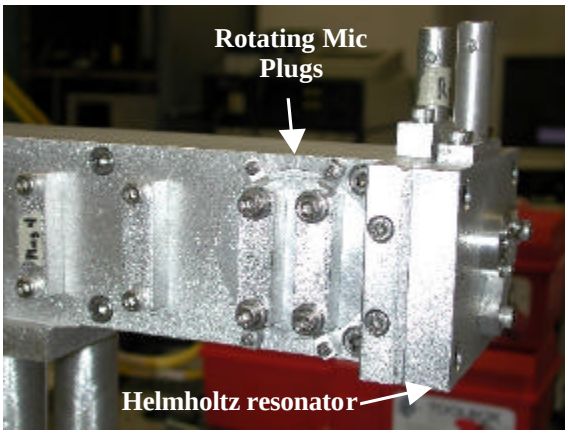

Figure 14: Normal impedance tube showing rotating microphone plugs, and end-mounted Helmholtz resonator.

The microphones were connected through Bruel and Kjær Type 2669 preamplifiers to a Bruel and Kjær PULSE Multi-Analyzer System Type 3560. The PULSE system served as the power supply and data acquisition unit for the microphones, and generated the source waveform. The source was fed through a Techron 7540 power supply amplifier to drive a JBL Pro 2426H compression driver, which is capable of producing acoustic waves between 1 kHz and 20 kHz. The compression driver was connected to a tapered transition piece and mounted to the far end of the impedance tube. The transition piece served to couple the circular throat of the compression driver to the square duct of the impedance tube.

A pseudo random waveform was generated using the PULSE Multi-Analyzer system. The waveform was internally bandpass filtered from 1 kHz to 6.4 kHz to avoid exciting the compression driver beyond its intended frequency range. A 3200 bin FFT with 8000 ensemble averages was performed on each incoming microphone signal. The FFT spanned from 0 to 6.4 kHz, yielding a 2 Hz binwidth. Data recorded at frequencies below 1 kHz was discarded because it was below the excitation frequency range. Using the method above, coherence between the two microphones in the rotating plug was typically close to unity, dropping only as low as 0.954 at frequencies where pressure nodes occurred at one of the microphone locations. The coherence between the cavity and incident microphones was similarly close to unity, typically residing at 0.999, except at the resonant frequency of the backplate where it would routinely fall as low as 0.2. This is believed to be caused by the large decrease in acoustic pressure in the cavity at the backplate resonant frequency, along with near-field effects causing by the large amplitude backplate deflection at these frequencies and the proximity of the cavity microphone. Coherence plots for some of the backplates are shown in the next chapter.

To determine the normal incidence acoustic impedance, frequency response measurements were taken using the two microphones in the rotating plug [18, 20]. The plug was then rotated and the measurement repeated. The two measurements were then averaged to remove any differences due to the individual microphone calibrations. This averaged frequency response was then used with the multi-point method to determine the acoustic impedance. The multi-point method essentially uses measurements from multiple microphones to create an overdetermined curve fit to the standing wave pattern inside the tube. When used with only two microphones, the multi-point method reduces

to the two-microphone method of impedance measurement [16-19]. The two-microphone method requires less than a half-wavelength spacing between the two microphone locations [17-19]. Although the tube is physically capable of supporting plane waves up to 6.7 kHz, testing was limited to 6.4 kHz because of this microphone spacing constraint. An alternative, single-microphone method [21] exists but was not used due to greater errors associated with the technique.

Using the multi-point method, the incident and reflected acoustic pressures [18, 20] are

$$P_i = \frac{CE - AB}{DE - A^2} \tag{3.1}$$

and

$$P_r = \frac{C - P_i D}{A} \tag{3.2}$$

where

$$A = \sum_{j=1}^{N} (1), \quad B = \sum_{j=1}^{N} P_j e^{-i\Gamma x_j}, \quad C = \sum_{j=1}^{N} P_j e^{i\Gamma x_j}$$
$$D = \sum_{j=1}^{N} e^{2i\Gamma x_j}, \quad \mathrm{E} = \sum_{\mathrm{j}=1}^{\mathrm{N}} e^{-i\Gamma x_j} \tag{3.3}$$

In (3.3), N is the number of microphone locations, x_j is the distance from the sample to each microphone location, $i = \sqrt{-1}$ and P_j is the measured complex acoustic pressure at each microphone location. Furthermore, Γ, the plane-wave propagation constant, is given by

$$\Gamma = k + i\beta_v \tag{3.4}$$

where $k = \frac{\omega}{c}$ and β_v is the attenuation constant due to viscothermal dissipation, given by

$$\beta_v = \frac{\sqrt{2}}{4a_0}\left(\frac{\omega}{c}\right)\left[\sqrt{\frac{\mu}{\rho\omega}} + (\gamma - 1)\sqrt{\frac{k}{\rho\omega c_p}}\right]. \tag{3.5}$$

In (3.5), a_o is the ratio of the duct area to perimeter, m is the absolute viscosity, k is the heat conduction coefficient, c_p is the constant of specific heat at constant pressure, r is the density of the medium, and g is the ratio of specific heats.

Using the measured transfer functions of one microphone location to another, the relative amplitudes and phases of the acoustic pressure are known, and can be inserted into P_j above, yielding relative values for the incident and reflected acoustic pressures. The normalized acoustic impedance can then be found as

$$z = \frac{1+R}{1-R} = q + ic \tag{3.6}$$

where

$$R = \frac{P_r}{P_i} \tag{3.7}$$

and θ and χ are the normalized resistance and reactance, respectively. This procedure was used to obtain the normalized resistance and reactance results shown in Chapter 4.

To measure the backplate mode shapes, a Polytec PI Vibrascan Laser Vibrometer with an OFV 055 vibrometer scanning head was used[22]. The scanning head was controlled by a Polytec PI OFV 3001 S vibrometer controller. The backplate was deflected under an acoustic pressure, which was supplied via an HP 33120A function generator connected through a Crown K1 balanced current amplifier to the JBL speaker at the end of the impedance tube. The frequency of excitation was kept below the resonant frequency of each backplate to ensure excitation of primarily the first mode.

Device Construction

The Helmholtz resonators were constructed of modular aluminum plates, as shown in Figure 15. The modular design allows for parts to be interchanged to test a

variety of resonator geometries. The resonators were designed to have a first resonant frequency and most second resonant frequencies occuring within the testable frequency range of 1 kHz to 6.4 kHz.

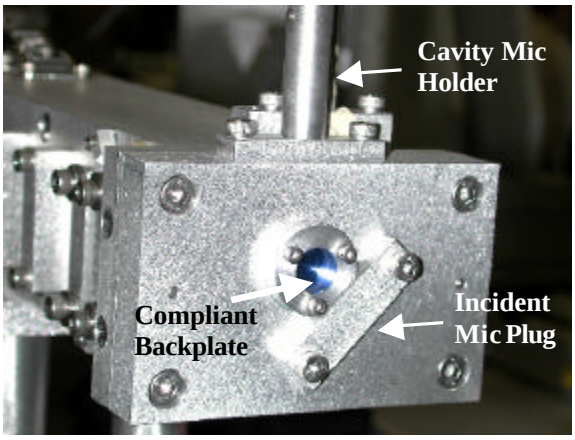

Figure 15: Photograph of the compliant backplate Helmholtz resonator showing compliant backplate clamped by circular clamping ring and incident and cavity microphone plugs.

The front plate consists of a 4.3 in. x 2.8 in. x 0.125 in. aluminum plate. It contains one 0.188 in. diameter, 0.125 in. deep hole that serves as the neck of the resonator. The cavity plate, contains a 0.5 in. diameter, 0.6 in. deep hole that serves as the resonator cavity. There were 24 different backplate configurations tested, consisting of various combinations of material, radius, and thickness as shown in Table 1. The three materials tested were aluminum, brass, and stainless steel, each with material properties as shown in Table 2.

To provide proper clamping of the 0.25 in. radius compliant backplates, a 0.25 in. thick, 1 in. diameter ring containing a 0.5 in. diameter hole was mounted to the backside of each compliant sheet and tightened against the cavity plate. A similar ring but of 1.5

in. outer diameter with a 0.96 in. diameter hole was used to clamp the 0.5 in. radius backplates. For the 0.5 in. radius backplates, an additional .02 in. thick ring was used underneath each plate, to suspend the backplate above the cavity plate and prevent contact during vibration. The rigid clamping rings allowed for an approximation of the compliant sheet as a clamped circular plate. Schematics of all devices are shown in Figure 68 through Figure 72 in Appendix A.

Table 1: Backplate configurations that were tested

Plate #	Material	Radius [in]	Thick [in]	Cmea [m^3/Pa]	Mmea [kg/m^4]
Al25-1	Aluminum	0.25	0.0013	4.618E-12	1.272E+03
Al25-2	Aluminum	0.25	0.0023	8.338E-13	2.250E+03
Al25-3	Aluminum	0.25	0.0032	3.096E-13	3.130E+03
Al25-5	Aluminum	0.25	0.005	8.116E-14	4.890E+03
Al50-2	Aluminum	0.5	0.0024	4.697E-11	5.869E+02
Al50-3	Aluminum	0.5	0.0031	2.179E-11	7.580E+02
Al50-5	Aluminum	0.5	0.0048	5.871E-12	1.174E+03
Al50-10	Aluminum	0.5	0.0105	5.609E-13	2.567E+03
Br25-1	Brass	0.25	0.0013	3.107E-12	3.974E+03
Br25-2	Brass	0.25	0.0023	5.610E-13	7.031E+03
Br25-3	Brass	0.25	0.003	2.528E-13	9.171E+03
Br25-5	Brass	0.25	0.0052	4.855E-14	1.590E+04
Br50-2	Brass	0.5	0.0021	4.717E-11	1.605E+03
Br50-3	Brass	0.5	0.0031	1.466E-11	2.369E+03
Br50-5	Brass	0.5	0.0051	3.293E-12	3.898E+03
Br50-10	Brass	0.5	0.0102	4.117E-13	7.795E+03
St25-1	Stainless Steel	0.25	0.0014	1.350E-12	3.972E+03
St25-2	Stainless Steel	0.25	0.0023	3.044E-13	6.525E+03
St25-3	Stainless Steel	0.25	0.0033	1.031E-13	9.361E+03
St25-5	Stainless Steel	0.25	0.0055	2.226E-14	1.560E+04
St50-2	Stainless Steel	0.5	0.0021	2.234E-13	1.489E+03
St50-3	Stainless Steel	0.5	0.0032	7.234E-12	2.269E+03
St50-5	Stainless Steel	0.5	0.0053	1.592E-12	3.759E+03
St50-10	Stainless Steel	0.5	0.0107	1.935E-13	7.588E+03

Table 2 : Material properties for backplates.

	Type	Density [g/cm^3]	Young's Modulus [GPa]	Poisson's Ratio
Aluminum	1100-H-18	2.71	69	0.33
Brass	ASTM: B19	8.47	103	0.3
Stainless Steel	ASTM: A666	7.86	193	0.3

Pressure amplification and impedance spectra were obtained for the Helmholtz resonator with each of the 24 different backplate configurations, along with mode shapes for one particular set of backplates. These data, along with a discussion of the results, are given in the next chapter.

CHAPTER 4
EXPERIMENTAL RESULTS

Measurement results were obtained for the Helmholtz resonator with each of 24 different backplate configurations. These results consisted of pressure amplification and impedance spectra. Additionally, mode shapes were obtained for the 0.25 in. radius, aluminum plates, to confirm their behavior as clamped circular plates.

Pressure Amplification

The pressure amplification measurements were obtained using the cavity and incident microphones, as described earlier in the experimental setup. The measurement results are shown below, sorted first by diameter of clamped backplate, then material type, followed by backplate thickness.

Helmholtz Resonator with Half-Inch Diameter, Clamped Backplates

The results obtained for the Helmholtz resonator with half-inch diameter, clamped backplates show overall good agreement with the theory, for the two thickest backplates, but displayed more significant discrepancies for the two thinnest backplates. This was consistent among all three material types. In Figure 16 through Figure 27, each graph displays the experimental results overlaid with two theoretical curves. The theoretical curves are based on the lumped element model of the compliant-backplate Helmholtz resonator using measured dimensions of the constructed devices. Two curves are shown because of the significant effect caused by a small uncertainty in the measurement of

backplate thickness. One theoretical curve uses the measured dimensions with uncertainty added to it, while the other curve used the measured dimensions with the uncertainty subtracted from it.

The effect of the uncertainty shows up more severely in the thinnest plates, as it comprises a larger percentage of the measured thickness. The thickness of each plate was measured using a Sears Craftsman precision micrometer. The vernier scale on the micrometer can theoretically provide results down to 0.0001 in.. Thickness measurements at various places over the surface of each backplate often yielded variations greater than this 0.0001 in. precision of the micrometer. Five thickness measurements were taken of each backplate. From these measurements, the mean thickness was computed along with the standard deviation for each backplate. From the standard deviation, σ, the uncertainty was calculated as

$$U = \pm t s \tag{4.1}$$

where $t = 2.776$ when only five data points are taken [23]. The mean thickness and uncertainty are shown in Table 3. The lumped element model is very sensitive to thickness, as the compliance of the backplate depends on the thickness to the third power. The large theoretical range shown in each graph below demonstrates this sensitivity.

Table 3 : Mean thickness and uncertainty in thickness measurement for all backplates

Plate #	Mean Thickness [in]	Uncertainty [in]
Al25-1	1.26E-03	1.52E-04
Al25-2	2.28E-03	1.24E-04
Al25-3	3.32E-03	3.62E-04
Al25-5	5.08E-03	3.62E-04
Br25-1	1.36E-03	6.97E-04
Br25-2	2.16E-03	1.52E-04
Br25-3	3.02E-03	1.24E-04
Br25-5	5.22E-03	3.04E-04
St25-1	1.38E-03	2.32E-04
St25-2	2.14E-03	2.48E-04
St25-3	3.26E-03	2.48E-04
St25-5	5.26E-03	2.48E-04
Al50-2	2.30E-03	3.40E-04
Al50-3	3.22E-03	2.32E-04
Al50-5	4.86E-03	1.52E-04
Al50-10	0.0105	2.32E-04
Br50-2	2.12E-03	1.24E-04
Br50-3	3.14E-03	2.32E-04
Br50-5	5.34E-03	1.52E-04
Br50-10	0.0104	2.32E-04
St50-2	2.40E-03	3.40E-04
St50-3	3.56E-03	4.21E-04
St50-5	5.28E-03	4.12E-04
St50-10	0.0106	3.17E-04

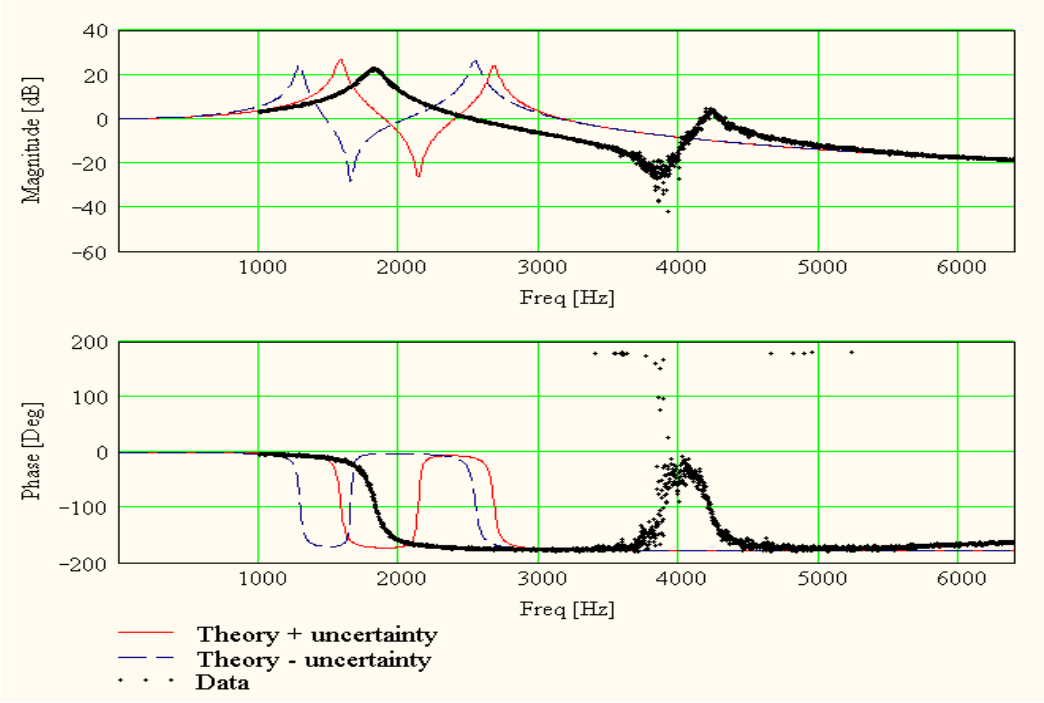

Figure 16: Magnitude and phase of pressure amplification spectrum for Helmholtz resonator with 0.001 in., aluminum backplate clamped at 0.5 in. diameter.

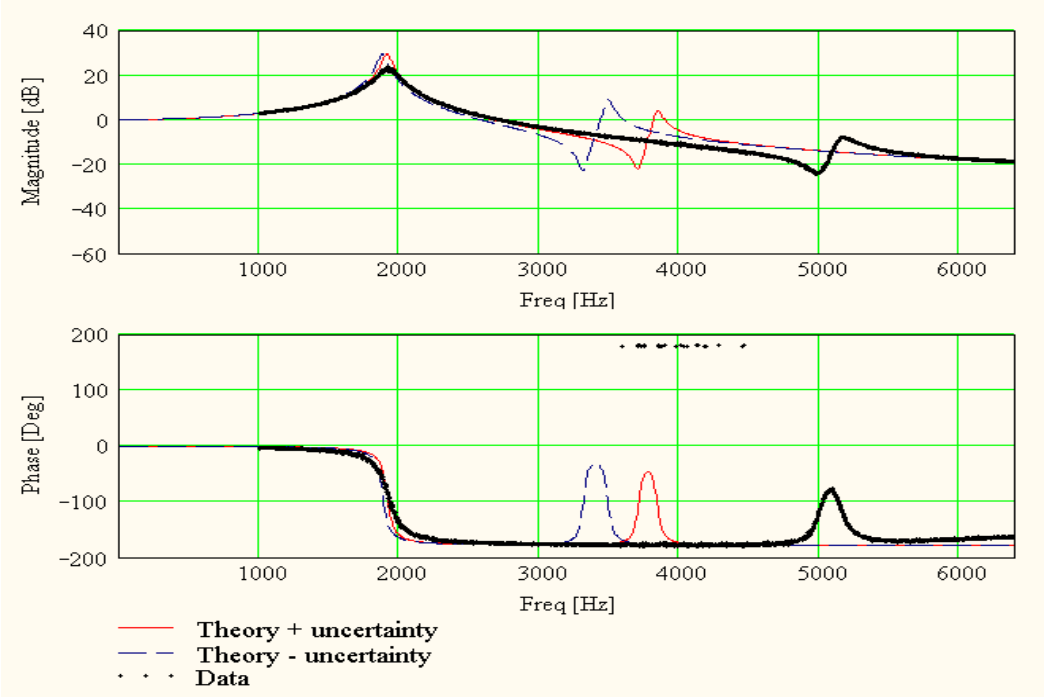

Figure 17: Magnitude and phase of pressure amplification spectrum for Helmholtz resonator with 0.002 in., aluminum backplate clamped at 0.5 in. diameter.

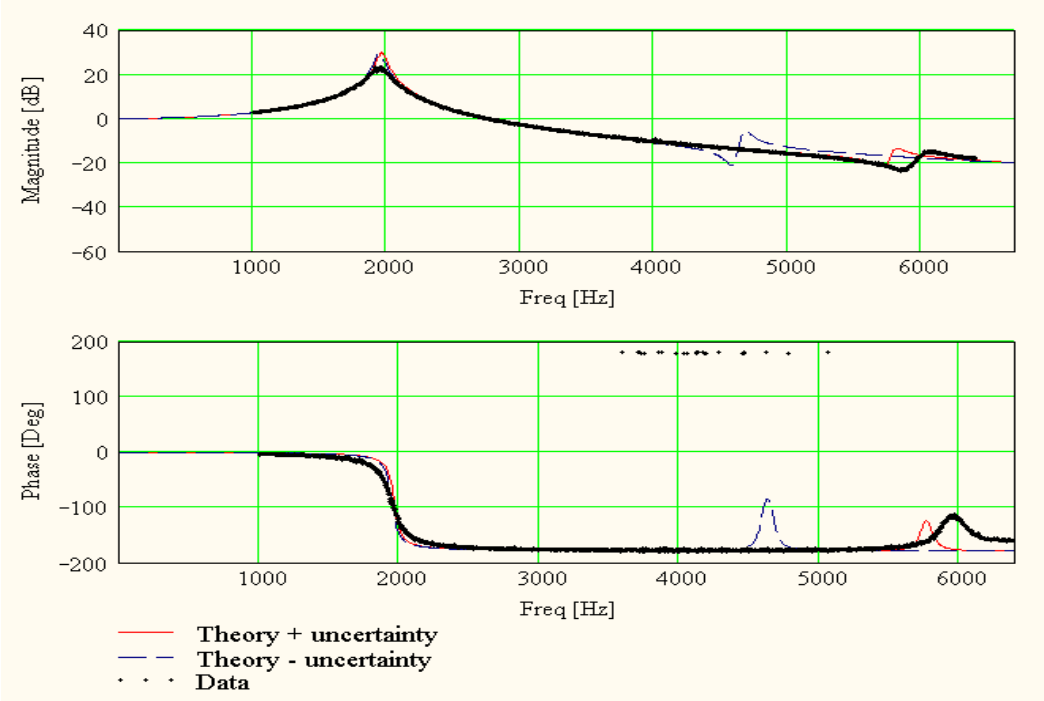

Figure 18: Magnitude and phase of pressure amplification spectrum for Helmholtz resonator with 0.003 in., aluminum backplate clamped at 0.5 in. diameter.

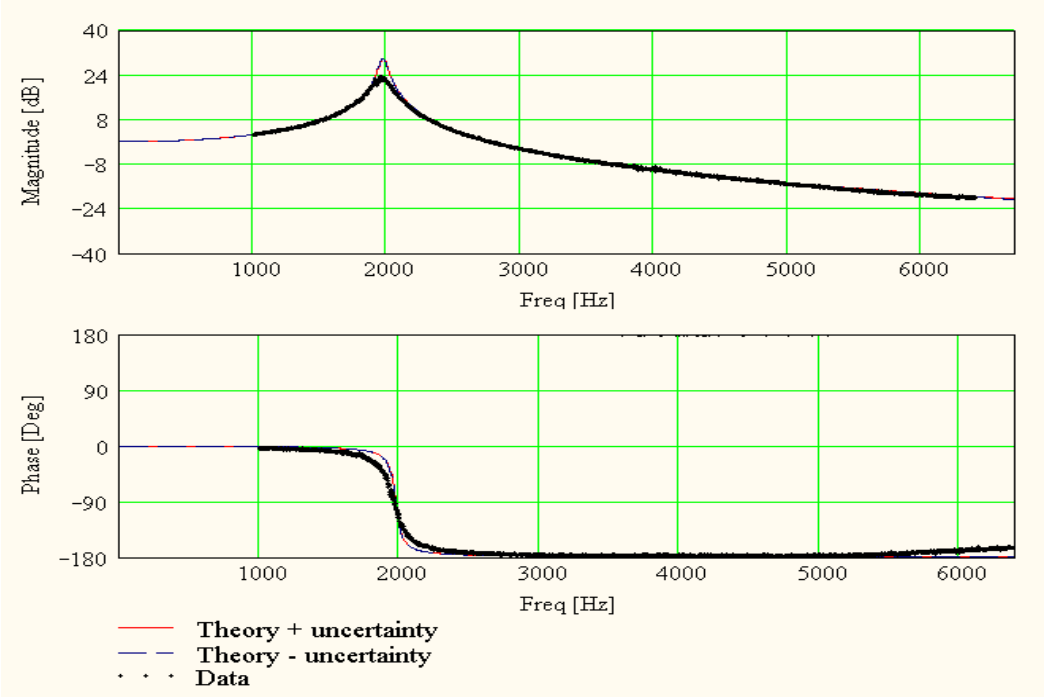

Figure 19: Magnitude and phase of pressure amplification spectrum for Helmholtz resonator with 0.005 in., aluminum backplate clamped at 0.5 in. diameter.

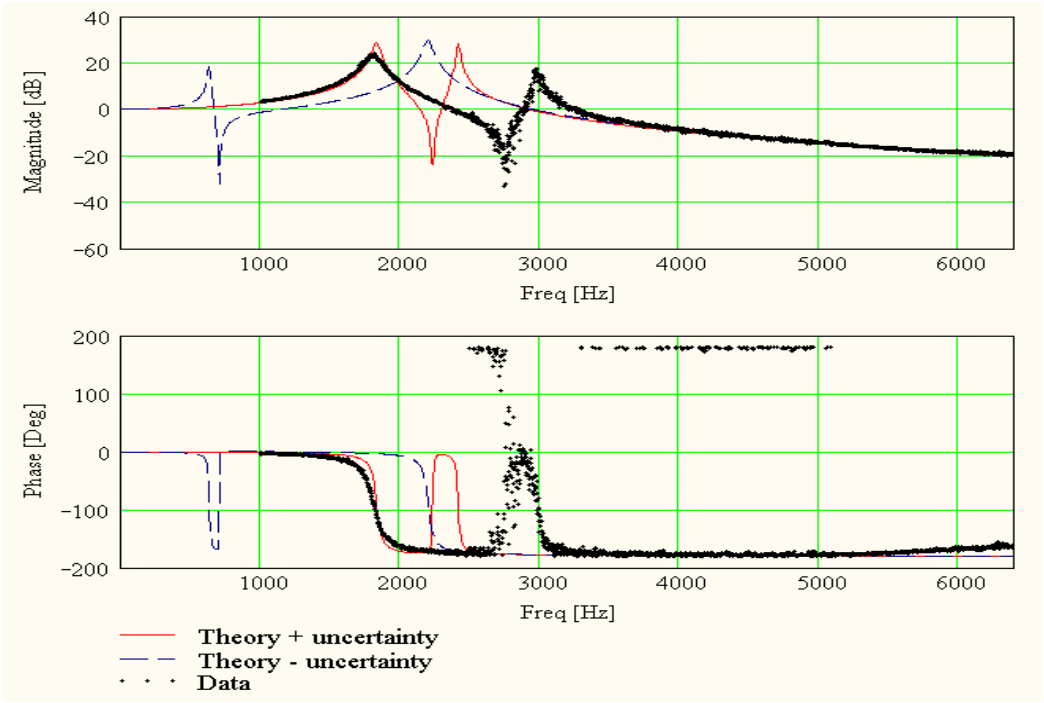

Figure 20: Magnitude and phase of pressure amplification spectrum for Helmholtz resonator with 0.001 in., brass backplate clamped at 0.5 in. diameter.

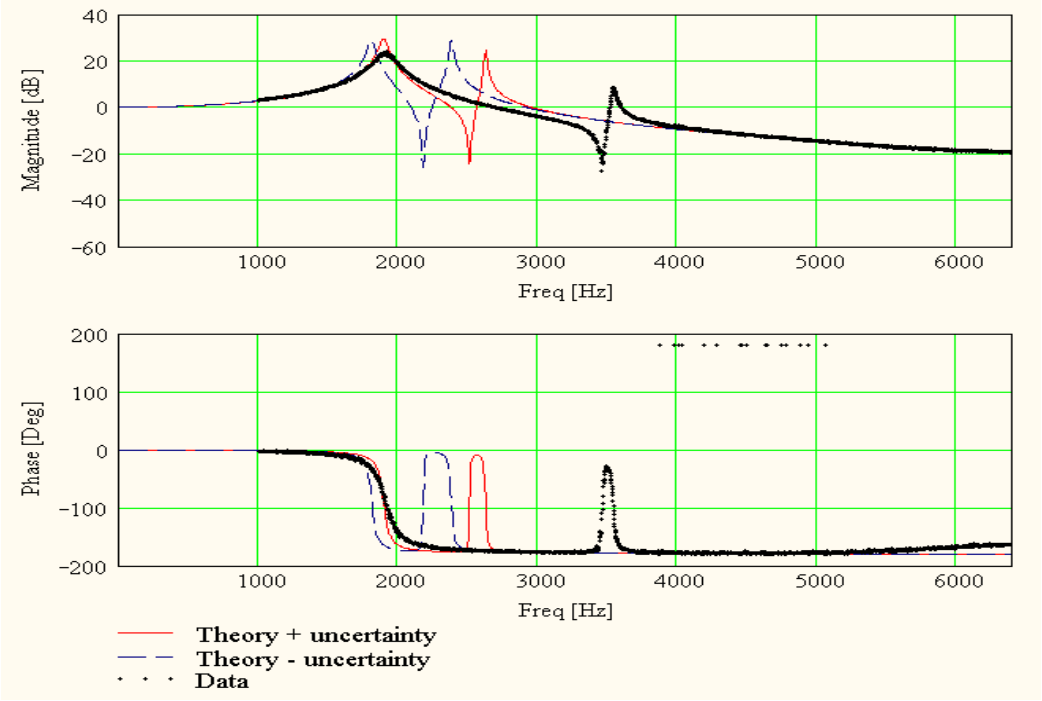

Figure 21: Magnitude and phase of pressure amplification spectrum for Helmholtz resonator with 0.002 in., brass backplate clamped at 0.5 in. diameter.

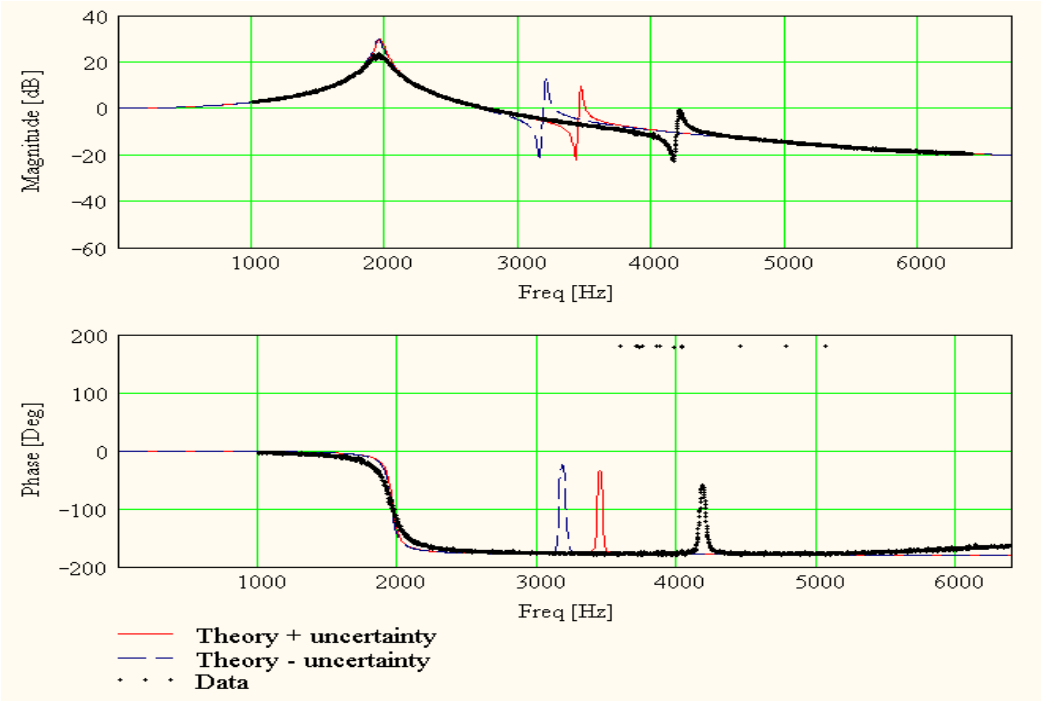

Figure 22: Magnitude and phase of pressure amplification spectrum for Helmholtz resonator with 0.003 in., brass backplate clamped at 0.5 in. diameter.

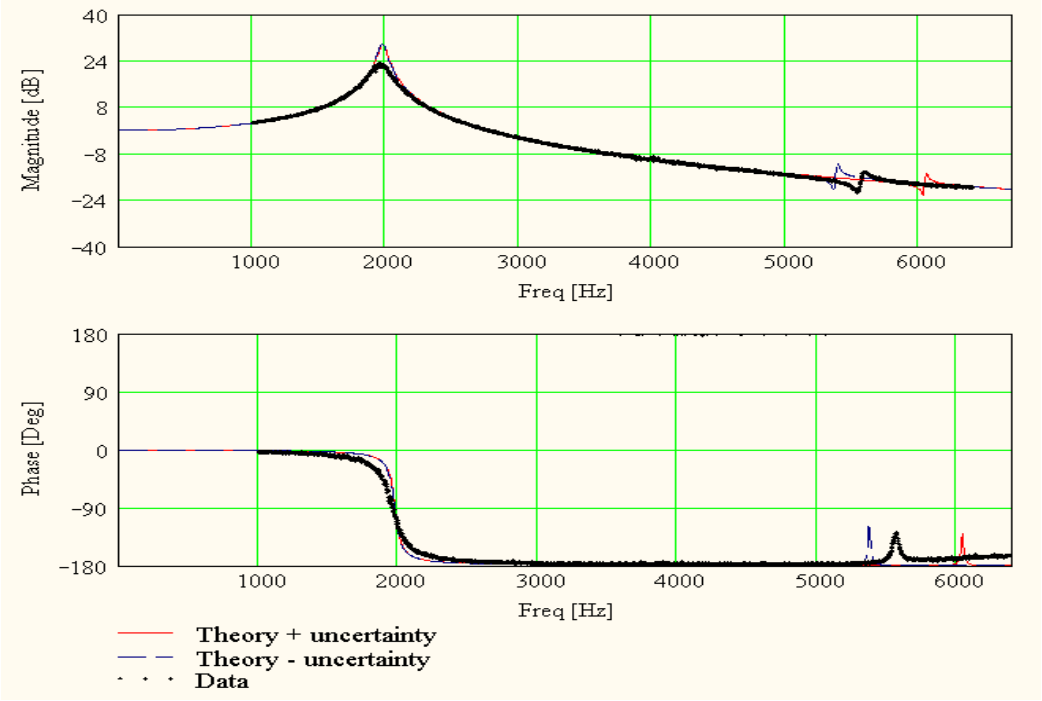

Figure 23: Magnitude and phase of pressure amplification spectrum for Helmholtz resonator with 0.005 in., brass backplate clamped at 0.5 in. diameter.

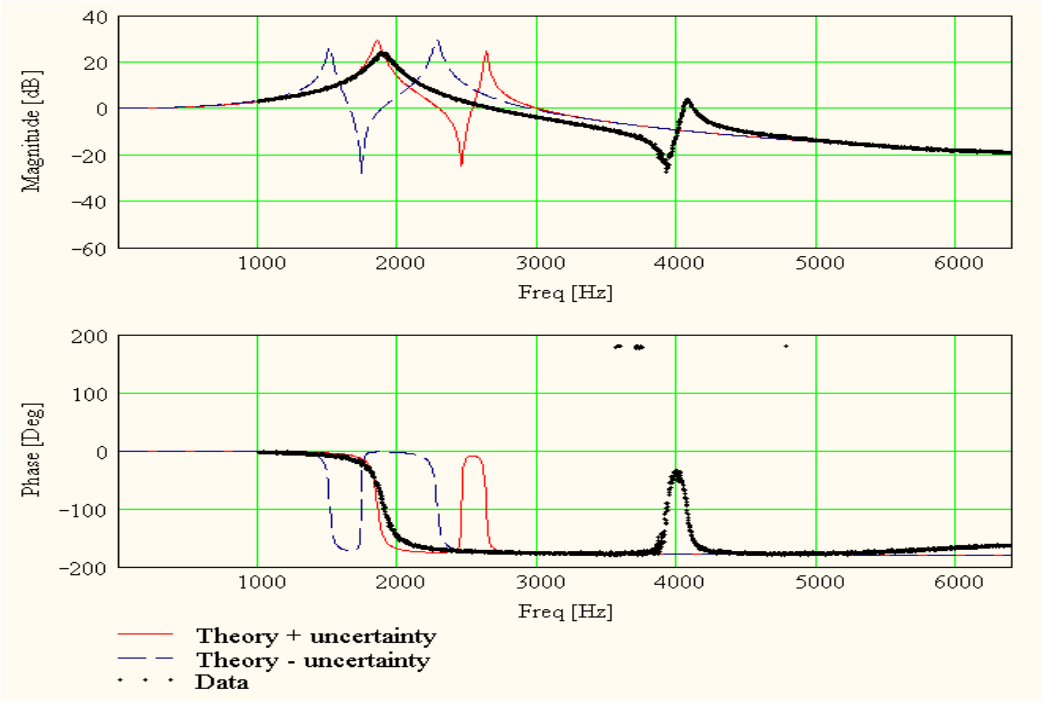

Figure 24: Magnitude and phase of pressure amplification spectrum for Helmholtz resonator with 0.001 in., stainless steel backplate clamped at 0.5 in. diameter.

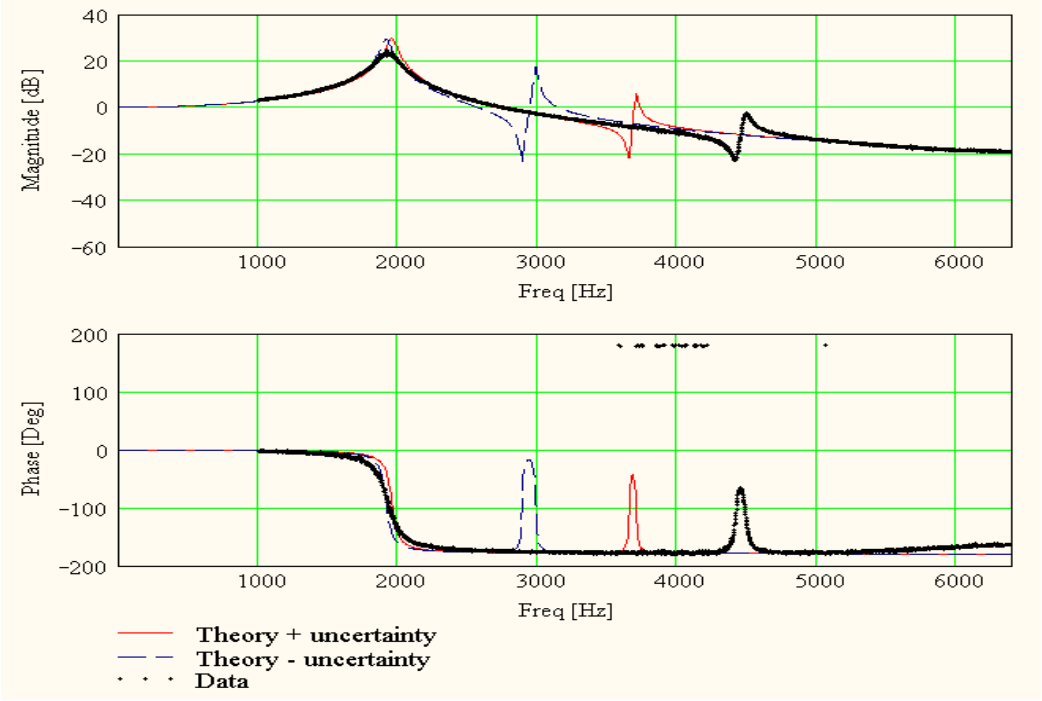

Figure 25: Magnitude and phase of pressure amplification spectrum for Helmholtz resonator with 0.002 in., stainless steel backplate clamped at 0.5 in. diameter.

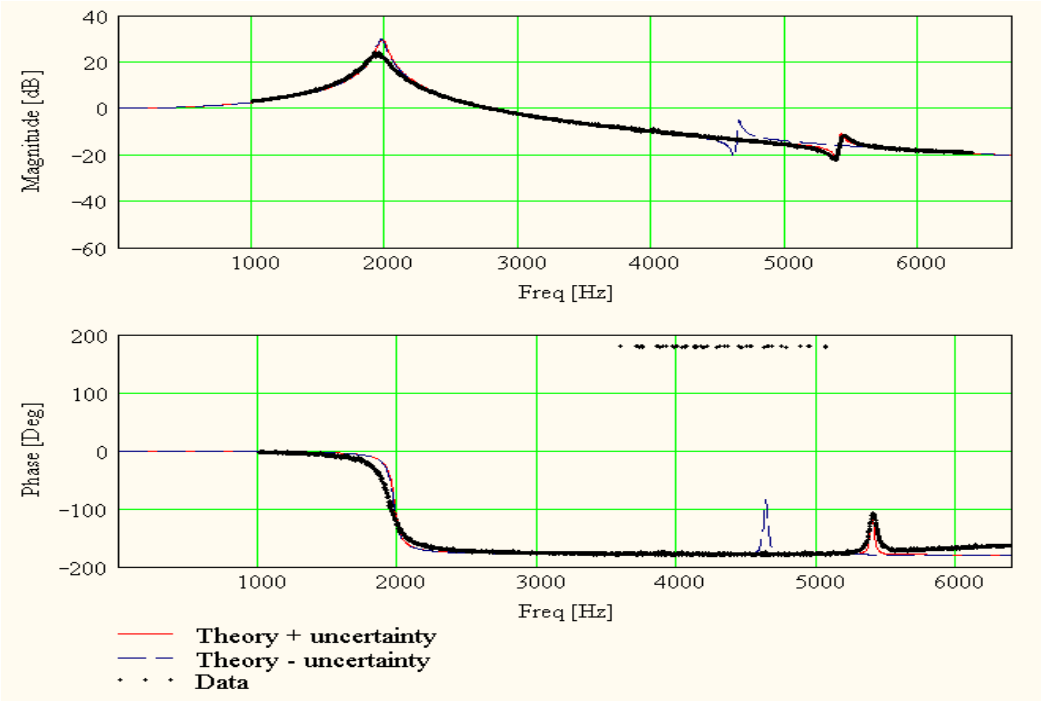

Figure 26: Magnitude and phase of pressure amplification spectrum for Helmholtz resonator with 0.003 in., stainless steel backplate clamped at 0.5 in. diameter.

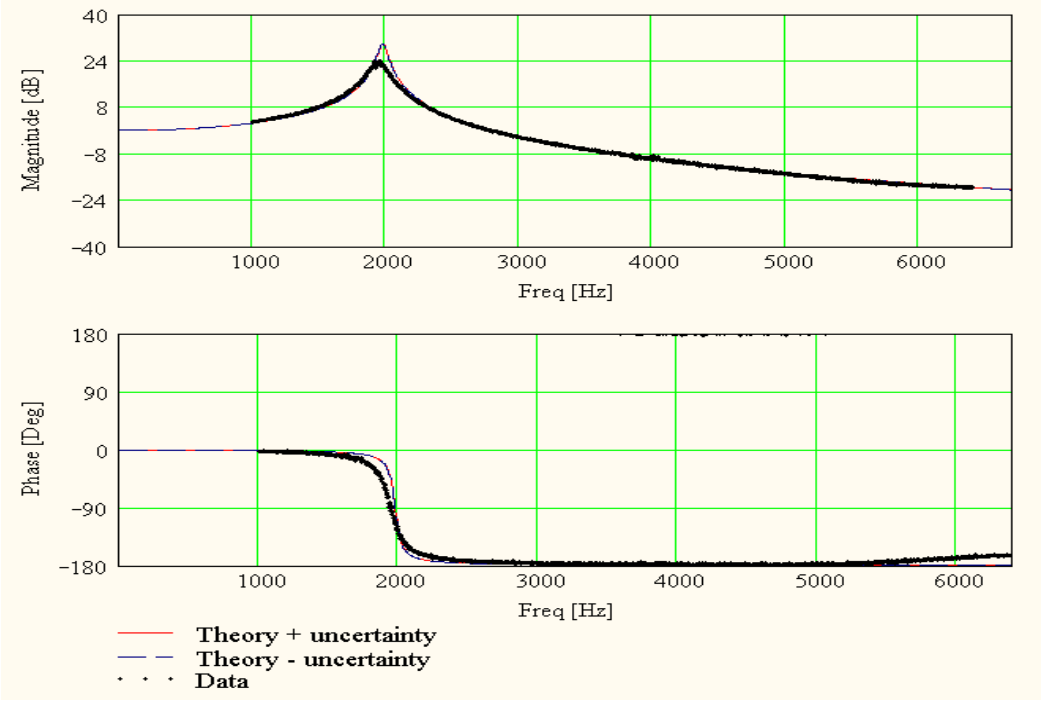

Figure 27: Magnitude and phase of pressure amplification spectrum for Helmholtz resonator with 0.005 in., stainless steel backplate clamped at 0.5 in. diameter.

The results shown in Figure 16 through Figure 27 show fairly good agreement between theory and data for the 0.003 in. and 0.005 in. thick backplates, regardless of material. The first resonant peak is predicted well for these configurations. Additionally the measured anti-resonance and second resonant peak match the theory fairly well for the 0.003 in. thick backplate. The anti-resonance and second resonant peak were not measurable for most of the 0.005 in. thick plates, as they occurred outside the testable frequency range.

The thinner plates did follow the expected trend of lower anti-resonant and second resonant frequencies compared to the thicker plates, however, these did not occur at frequencies quite as low as predicted. This indicates they were stiffer than predicted and is believed to be due to two factors, the uncertainty in their thickness measurement, and

possible in-plane tension applied as an inadvertent effect of the clamping. Many of the stiffer-than-expected plates had a raised lip on the inside edge of the holes that allow the clamping screws to pass through. The raised lip indicated they were catching on the threads of the clamping screws, which may be adding tension to the plate. The in-plane tension would raise the stiffness of the plates, thereby increasing the resonant frequency.

To further investigate this possibility, real-time pressure amplification measurements were taken of some of the compliant backplates, while the clamping screws were adjusted. It was found that the resonant frequency of each backplate increased as the screws were tightened. This effect continued up to the maximum torque that was achievable with the ratchet on hand. If no in-plane tension was occurring, then the resonant frequency would not rise with increasing torque on the screws, therefore, these results indicate the likely presence of in-plane tension. A redesign of the clamping setup would be necessary to reduce or eliminate this effect.

Despite the quantitative discrepancies in the thinnest backplates, the actual qualitative behavior of the compliant-backplate Helmholtz resonator does follow the lumped element models of a coupled resonator system. This is evidenced by the shift in first resonant peak due to the presence of the anti-resonance introduced by the backplate.

The coherence for these measurements typically were near one, except at frequencies around the anti-resonance. The coherence for the pressure amplification measurements of the Helmholtz resonator with 0.001 in. thick aluminum backplate is shown in Figure 28. On the plates where an anti-resonance was not within the frequency range tested, the coherence stayed above 0.98 as shown in Figure 29.

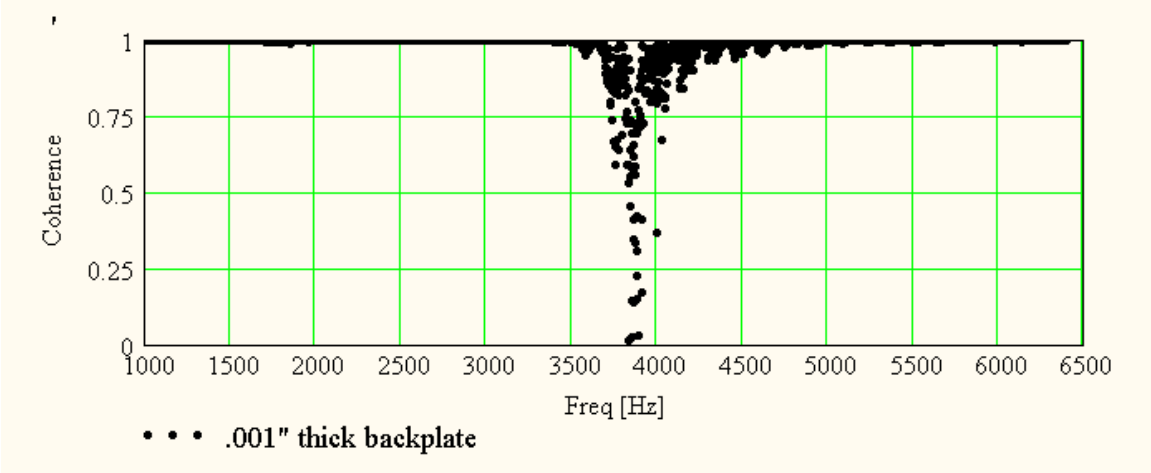

Figure 28: Coherence between cavity and incident microphone for Helmholtz resonator with 0.001 in. thick aluminum backplate clamped at 0.5 in. diameter.

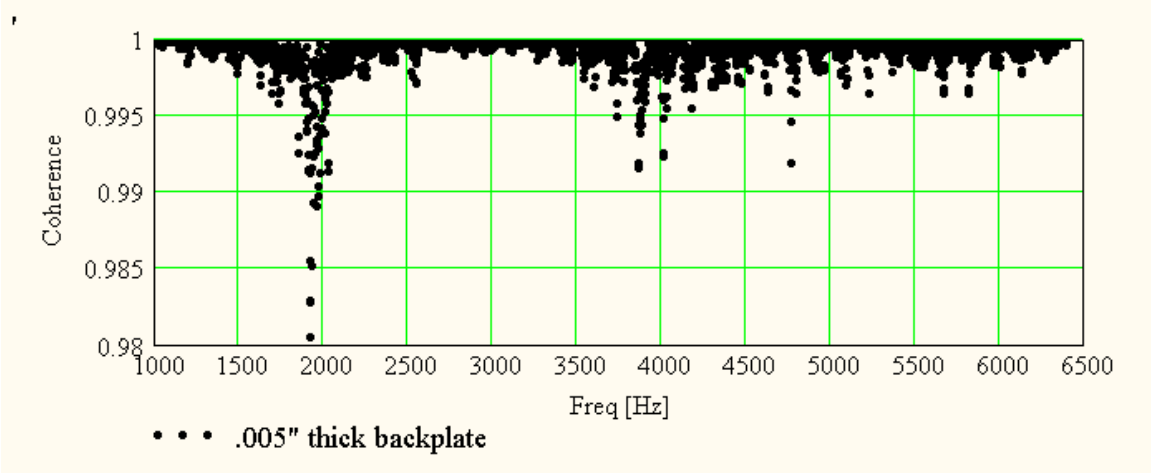

Figure 29: Coherence between cavity and incident microphone for Helmholtz resonator with 0.005 in. thick stainless steel backplate clamped at 0.5 in. diameter.

Helmholtz Resonator with One-Inch Diameter, Clamped Backplates

Pressure amplification spectra were also obtained for the Helmholtz resonator with one-inch diameter, clamped backplates. Overall, these backplates showed better agreement with the theoretical models. The improvement is believed to be due to the thicker plates that were used in these experiments. This improved the percentage

uncertainty in the thickness measurement, leading to more accurate predictions. The spectra are shown below in Figure 30 through Figure 41.

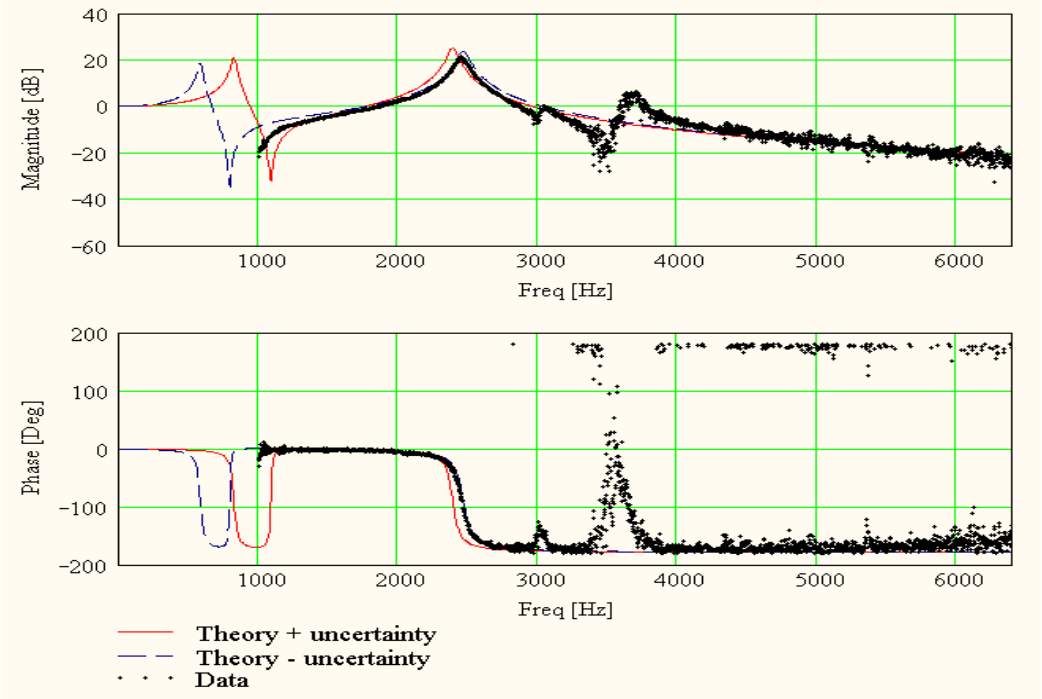

Figure 30: Magnitude and phase of pressure amplification spectrum for Helmholtz resonator with 0.002 in., aluminum backplate clamped at 0.96 in. diameter.

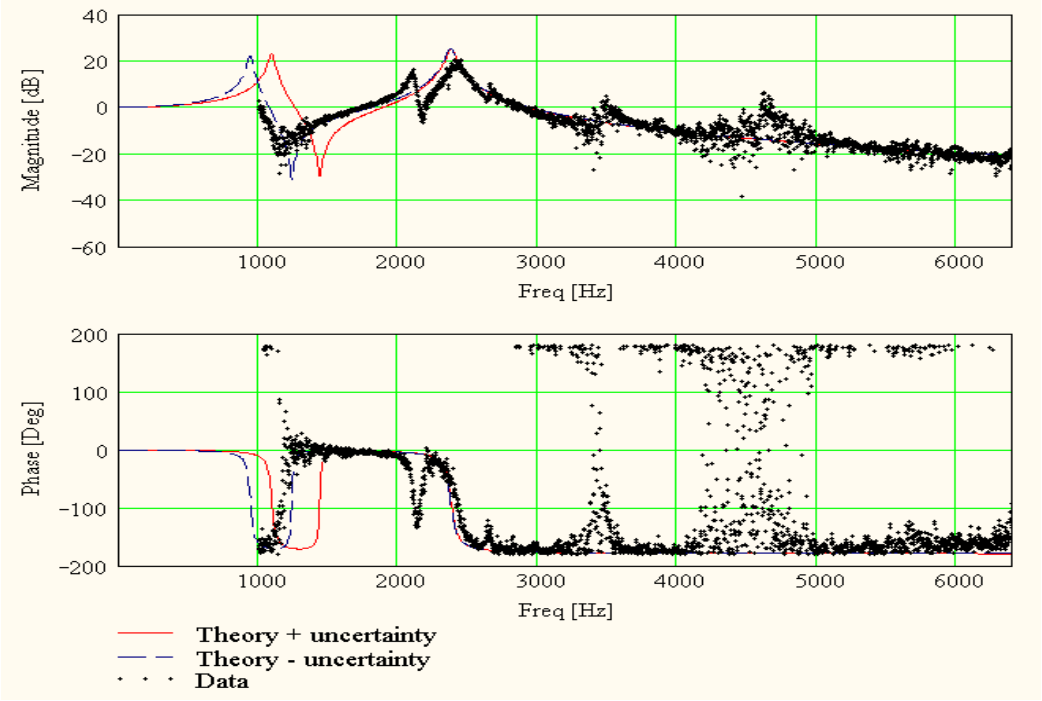

Figure 31: Magnitude and phase of pressure amplification spectrum for Helmholtz resonator with 0.003 in., aluminum backplate clamped at 0.96 in. diameter.

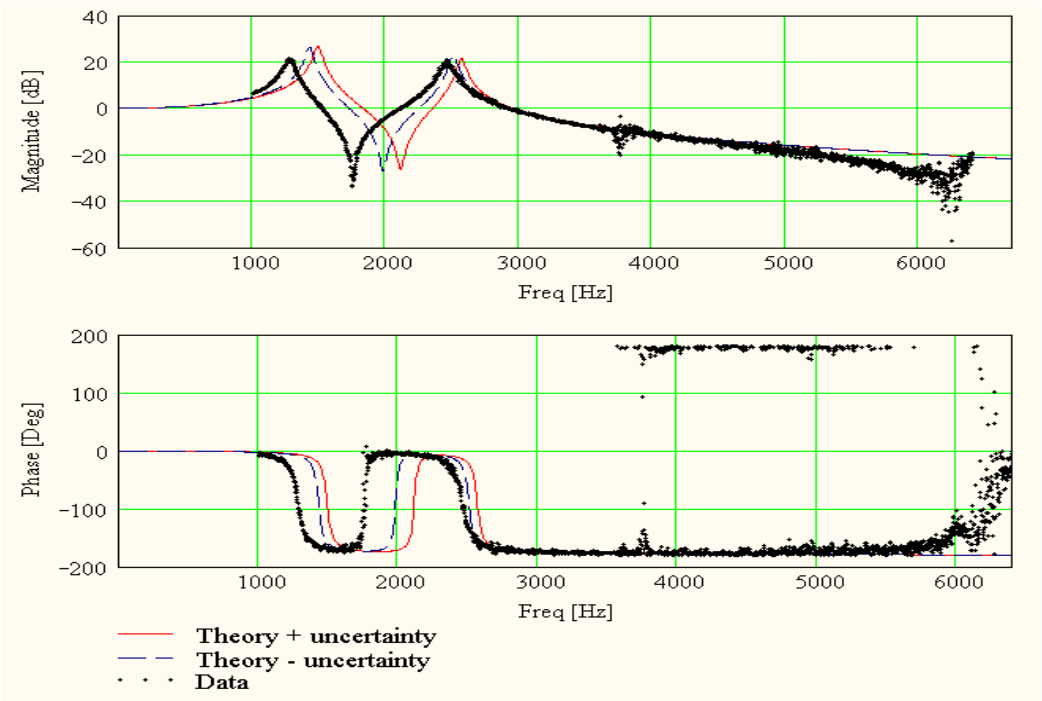

Figure 32: Magnitude and phase of pressure amplification spectrum for Helmholtz resonator with 0.005 in., aluminum backplate clamped at 0.96 in. diameter.

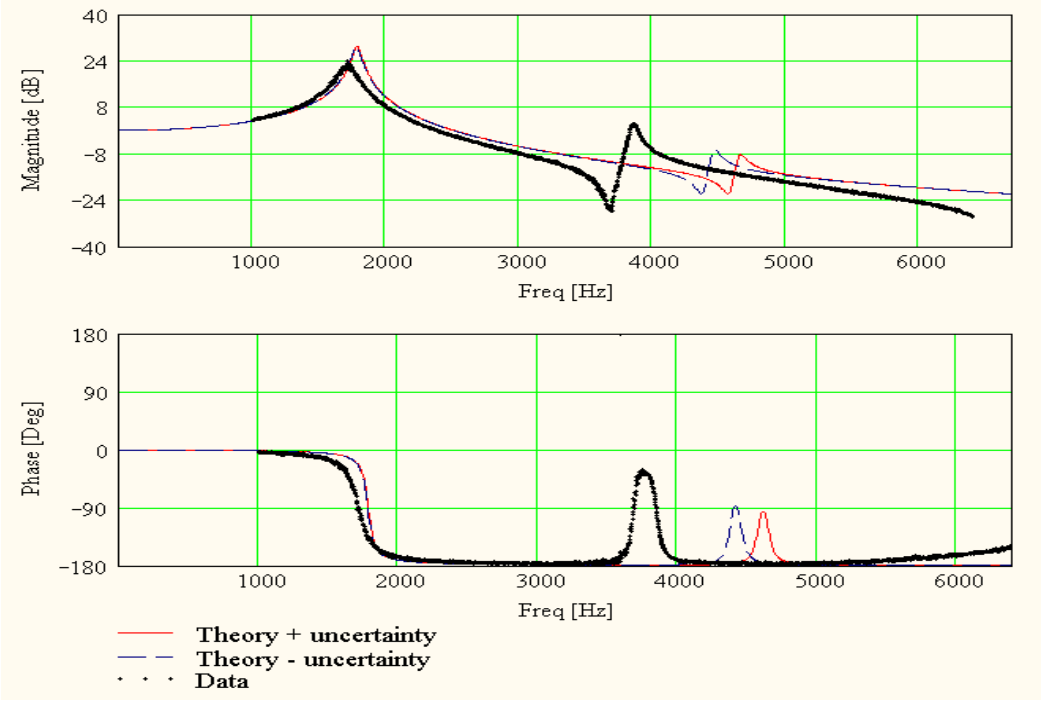

Figure 33: Magnitude and phase of pressure amplification spectrum for Helmholtz resonator with 0.010 in., aluminum backplate clamped at 0.96 in. diameter.

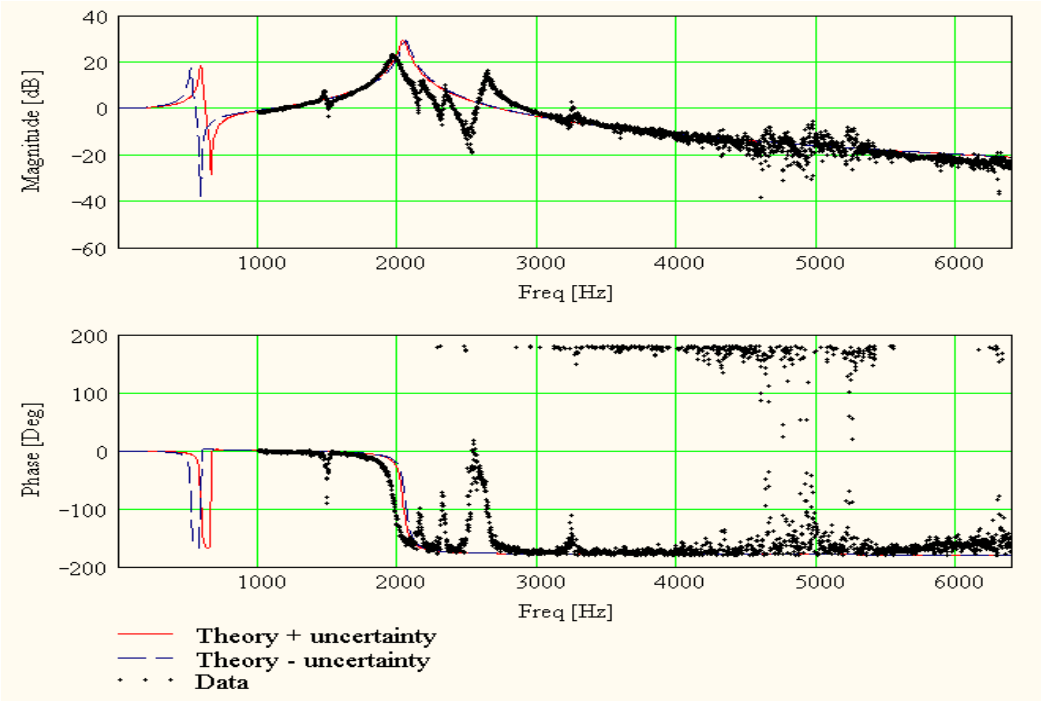

Figure 34: Magnitude and phase of pressure amplification spectrum for Helmholtz resonator with 0.002 in., brass backplate clamped at 0.96 in. diameter.

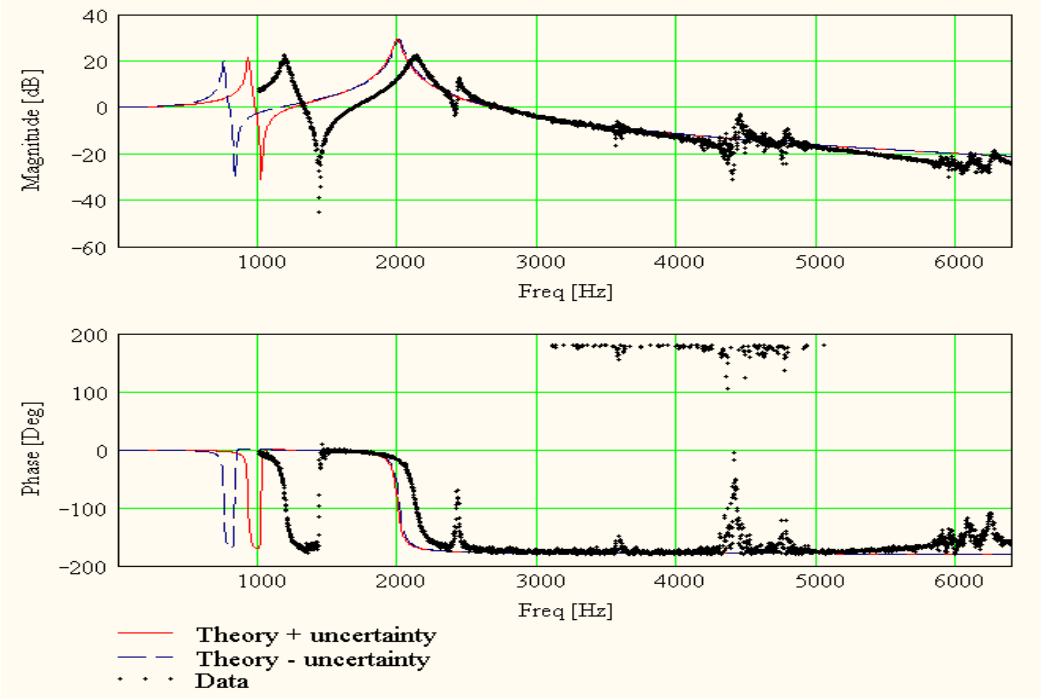

Figure 35: Magnitude and phase of pressure amplification spectrum for Helmholtz resonator with 0.003 in., brass backplate clamped at 0.96 in. diameter.

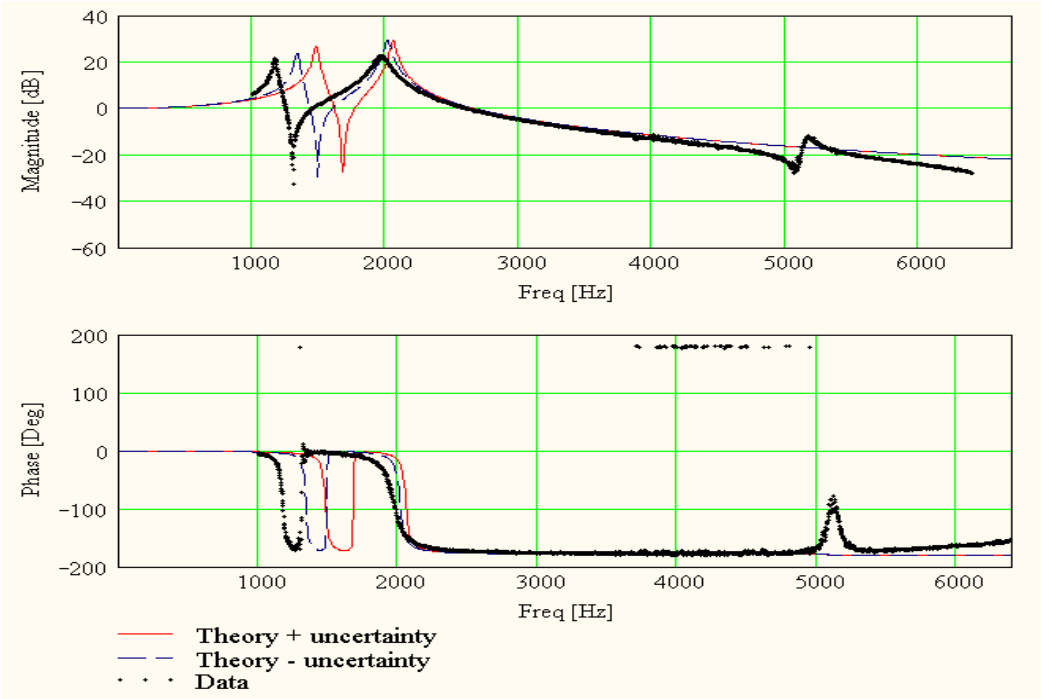

Figure 36: Magnitude and phase of pressure amplification spectrum for Helmholtz resonator with 0.005 in., brass backplate clamped at 0.96 in. diameter.

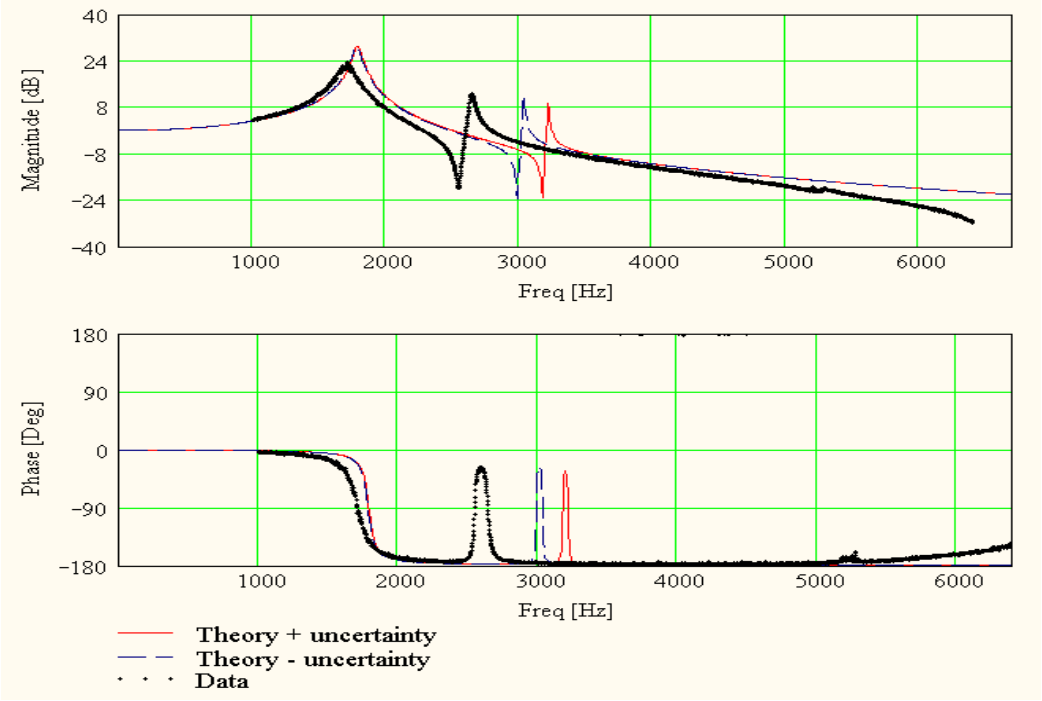

Figure 37: Magnitude and phase of pressure amplification spectrum for Helmholtz resonator with 0.010 in., brass backplate clamped at 0.96 in. diameter.

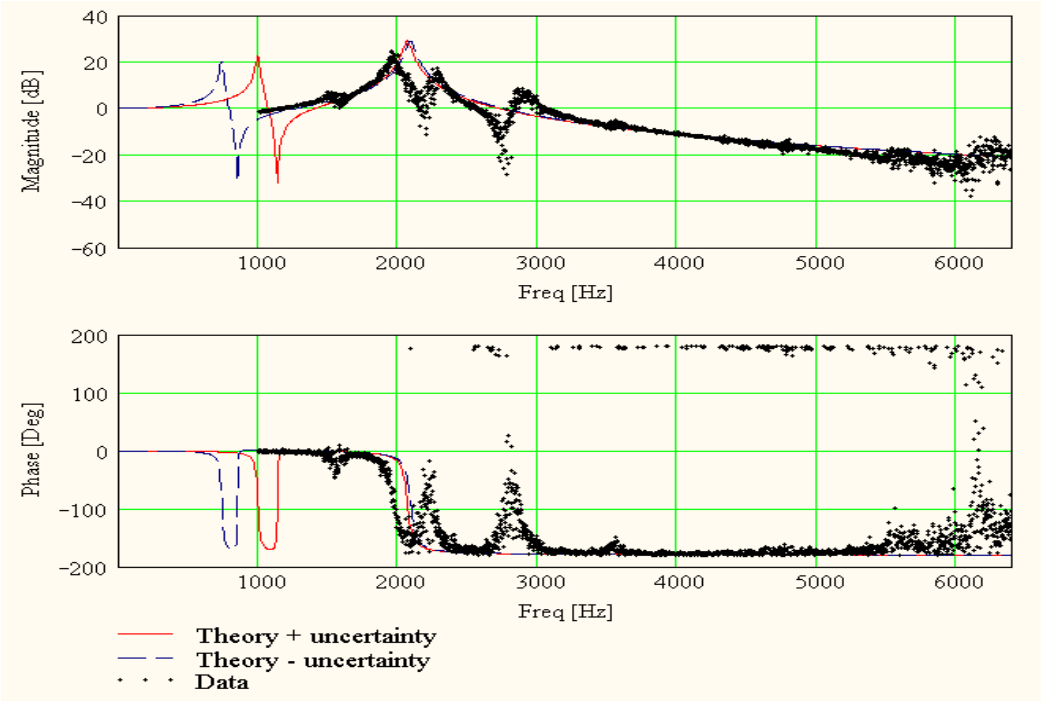

Figure 38: Magnitude and phase of pressure amplification spectrum for Helmholtz resonator with 0.002 in., stainless steel backplate clamped at 0.96 in. diameter.

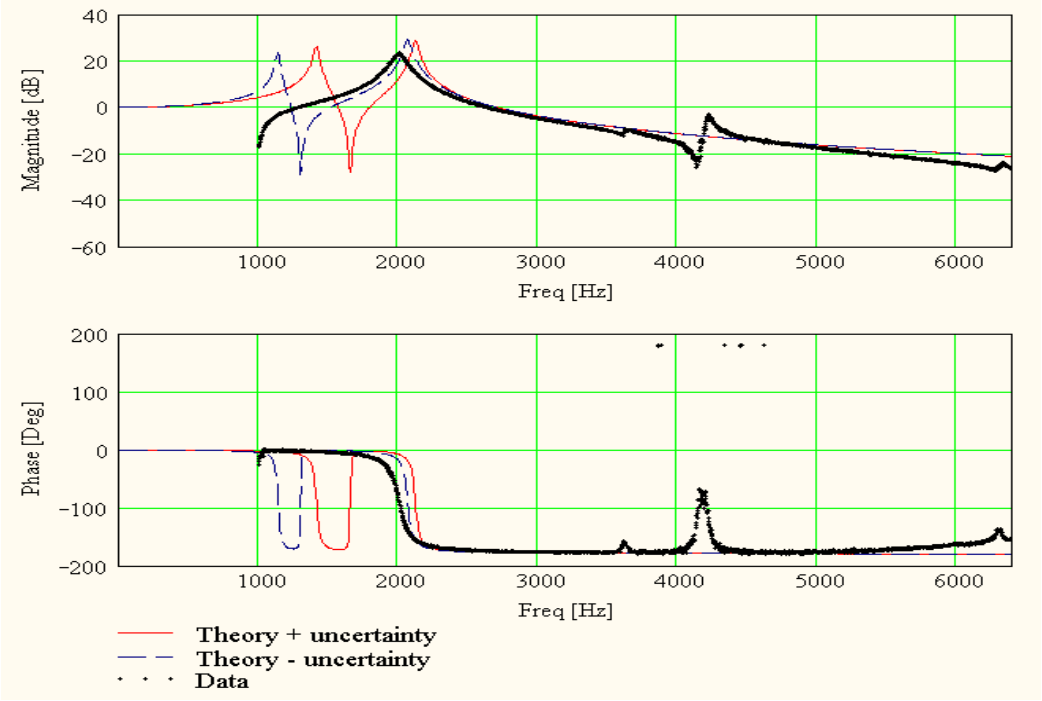

Figure 39: Magnitude and phase of pressure amplification spectrum for Helmholtz resonator with 0.003 in., stainless steel backplate clamped at 0.96 in. diameter.

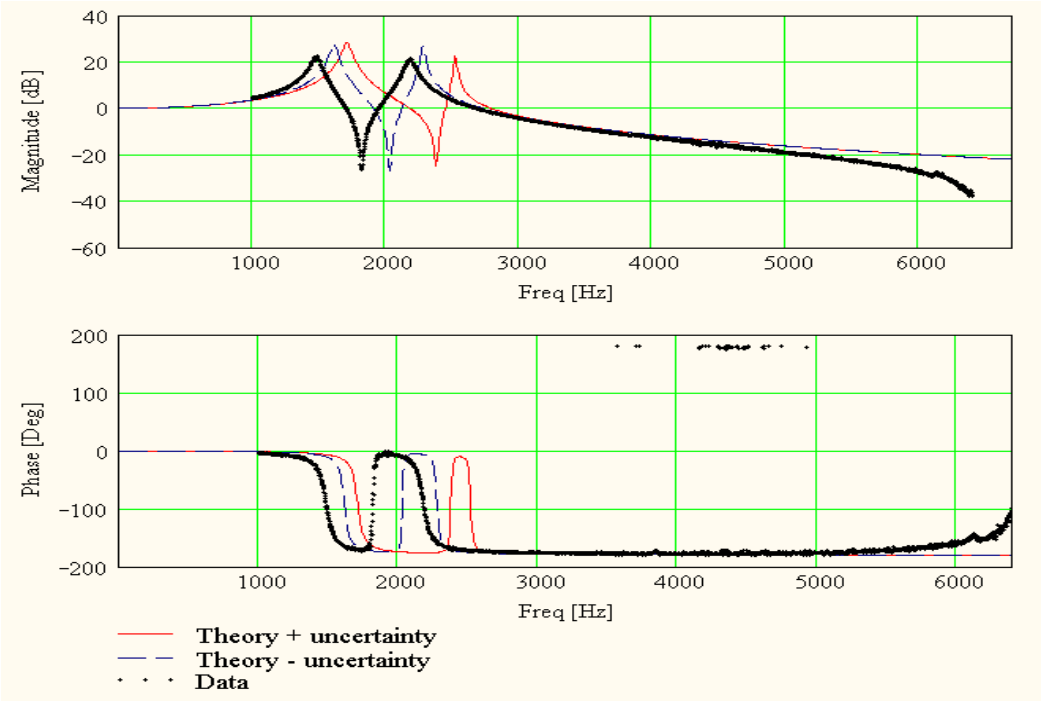

Figure 40: Magnitude and phase of pressure amplification spectrum for Helmholtz resonator with 0.005 in., stainless steel backplate clamped at 0.96 in. diameter.

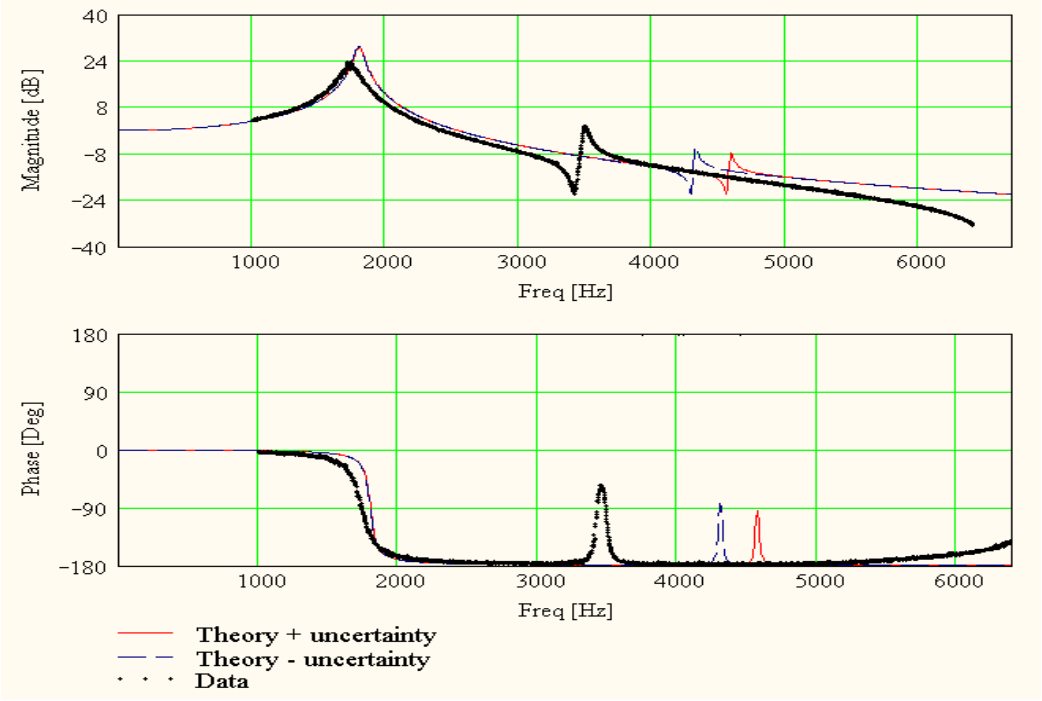

Figure 41: Magnitude and phase of pressure amplification spectrum for Helmholtz resonator with 0.010 in., stainless steel backplate clamped at 0.96 in. diameter.

Compared to the other backplates, the one-inch diameter clamped backplates exhibited better agreement between theory and measurement. The first and second resonant peaks and anti-resonance that fell within the testable frequency range were predicted fairly well, for the most part. However, some of the experimentally measured backplate resonant frequencies were lower than the predicted resonant frequencies. This can easily result from the lack of a perfectly clamped boundary condition. Any compliance in that boundary will lead to an increase in effective radius, resulting in a lower resonant frequency. In addition to these larger features of the measured spectra, smaller peaks were also visible. These smaller peaks are believed to be due to the presence of higher-order modes and their coupled interaction with the acoustic resonance. These peaks only occurred on the larger diameter backplates because the higher order

modes for these backplates fell within the testable frequency range and began encroaching on the original acoustic resonant frequency near 2 kHz, where coupling with the acoustic resonance is strongest.

Input Impedance

As previously discussed in the experimental setup, the specific acoustic impedance at the input to the compliant-backplate Helmholtz resonator was found from measurements of the reflection coefficient, obtained via the multi-point method.

Helmholtz Resonator with Half-Inch Diameter, Clamped Backplates

Impedance measurements were obtained for the 12 configurations that were clamped at 0.5 in. diameter and are shown in Figure 42 through Figure 53. The impedance data for each configuration is shown in terms of resistance (real) and reactance (imaginary) components.

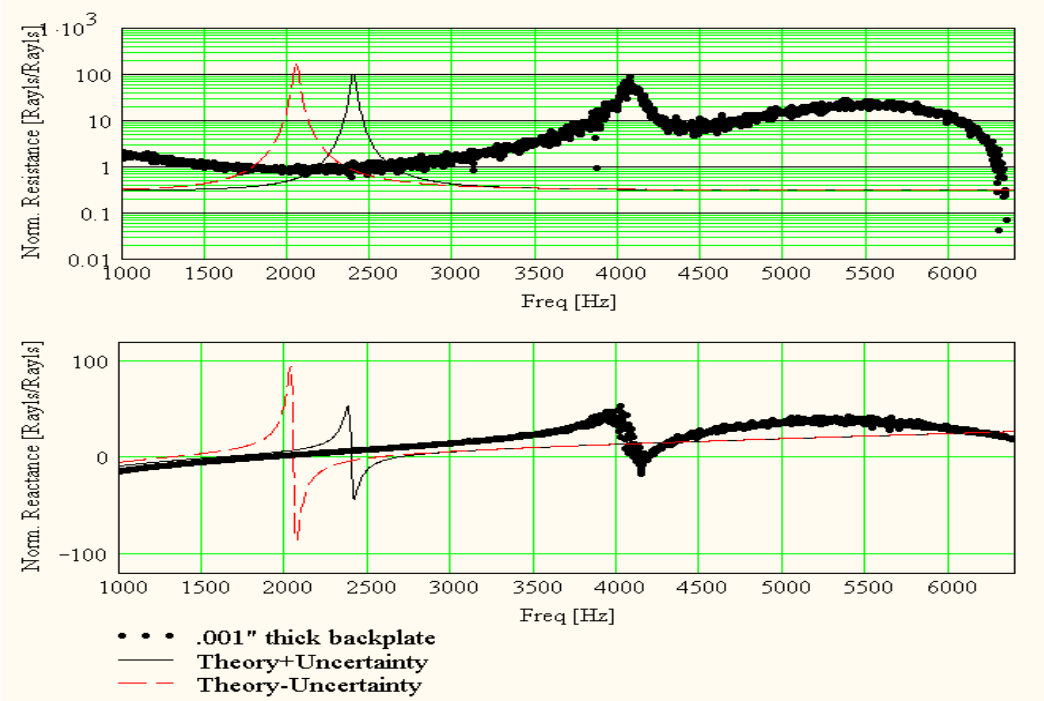

Figure 42: Normalized resistance and reactance for Helmholtz resonator with 0.001 in. aluminum backplate clamped at 0.5 in. diameter.

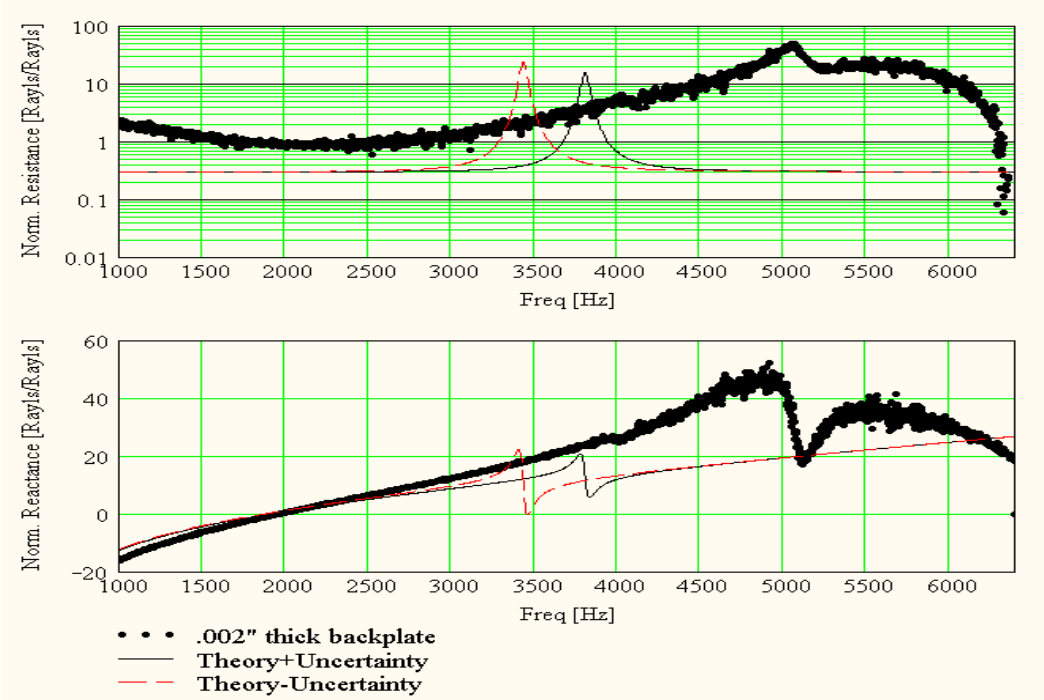

Figure 43: Normalized resistance and reactance for Helmholtz resonator with 0.002 in., aluminum backplate clamped at 0.5 in. diameter.

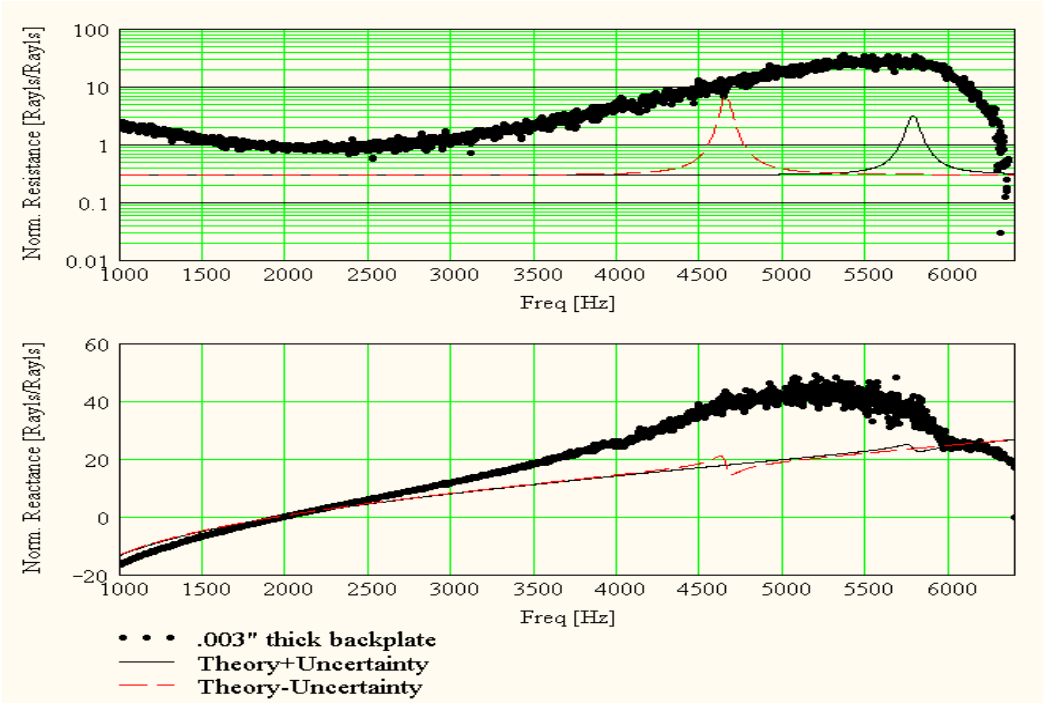

Figure 44: Normalized resistance and reactance for Helmholtz resonator with 0.003 in., aluminum backplate clamped at 0.5 in. diameter.

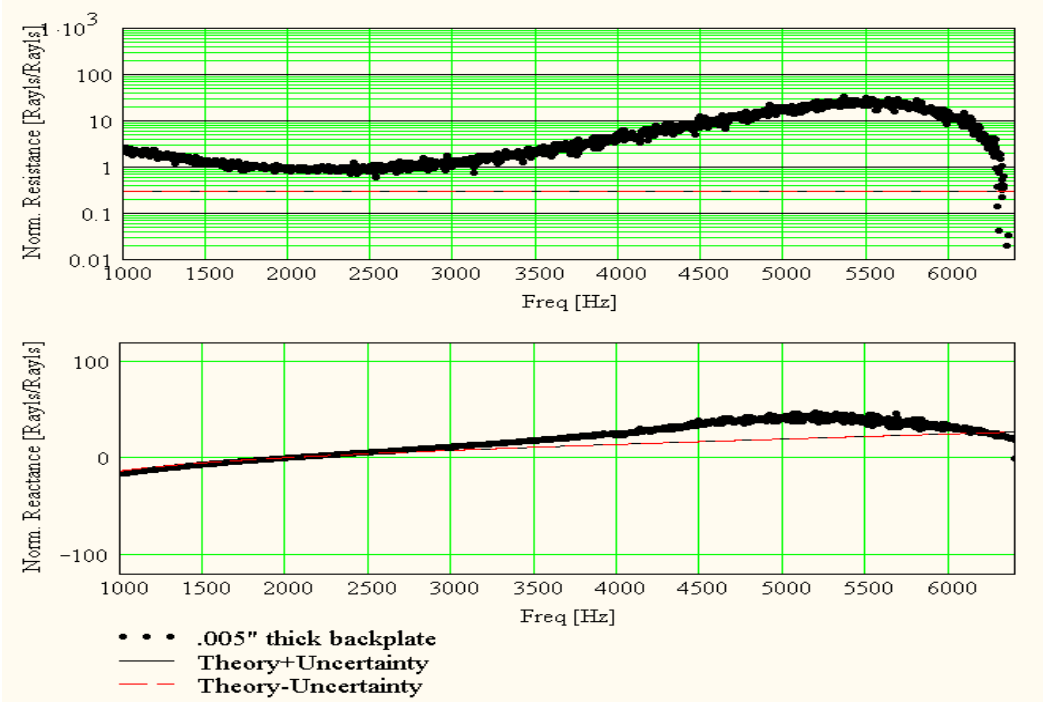

Figure 45: Normalized resistance and reactance for Helmholtz resonator with 0.005 in., aluminum backplate clamped at 0.5 in. diameter.

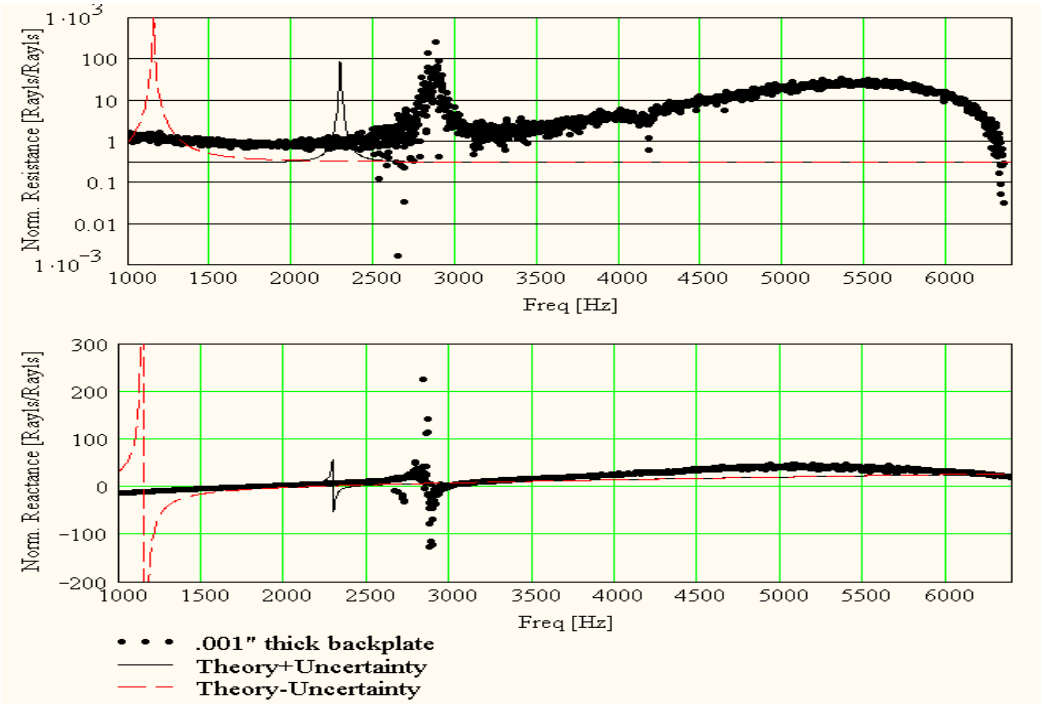

Figure 46: Normalized resistance and reactance for Helmholtz resonator with 0.001 in., brass backplate clamped at 0.5 in. diameter.

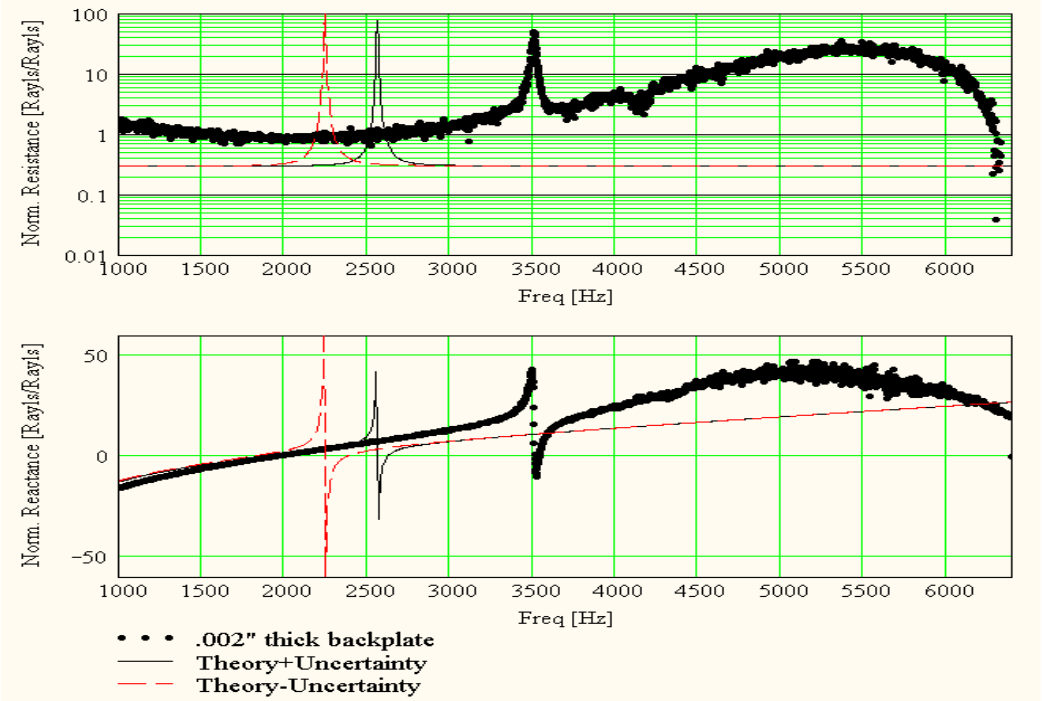

Figure 47: Normalized resistance and reactance for Helmholtz resonator with 0.002 in., brass backplate clamped at 0.5 in. diameter.

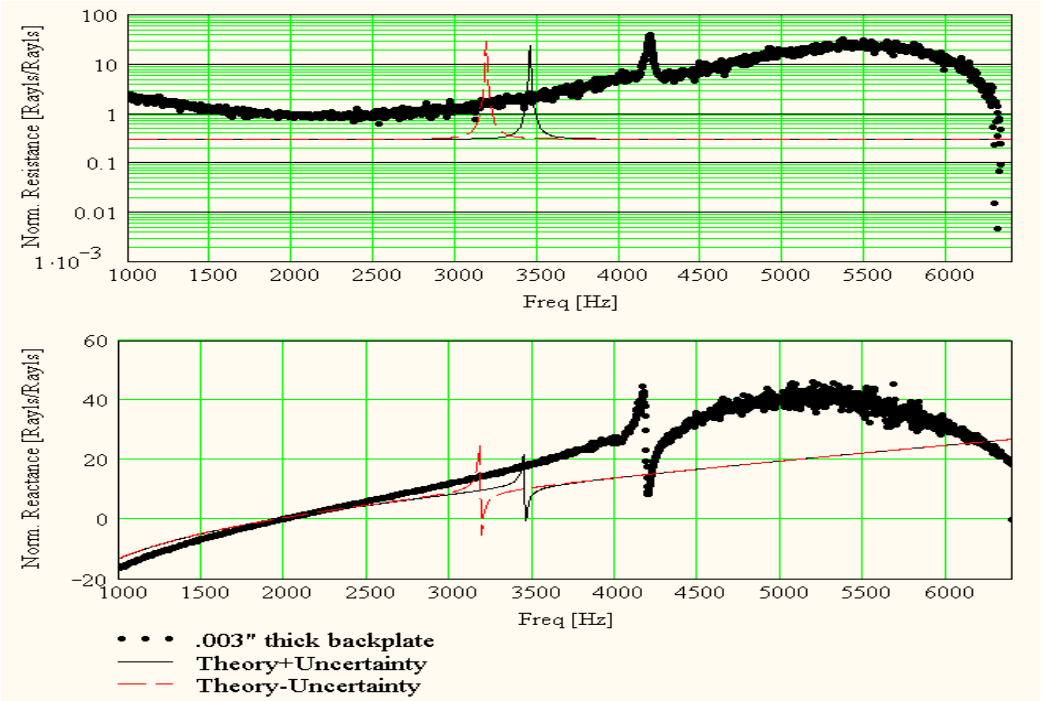

Figure 48: Normalized resistance and reactance for Helmholtz resonator with 0.003 in., brass backplate clamped at 0.5 in. diameter.

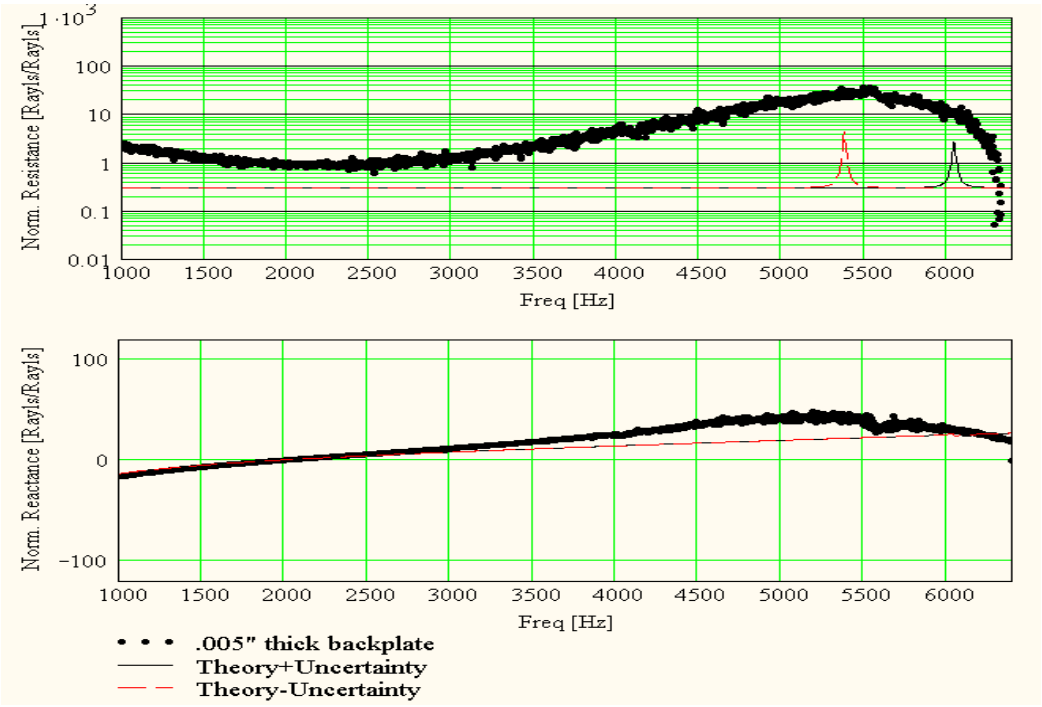

Figure 49: Normalized resistance and reactance for Helmholtz resonator with 0.005 in., brass backplate clamped at 0.5 in. diameter.

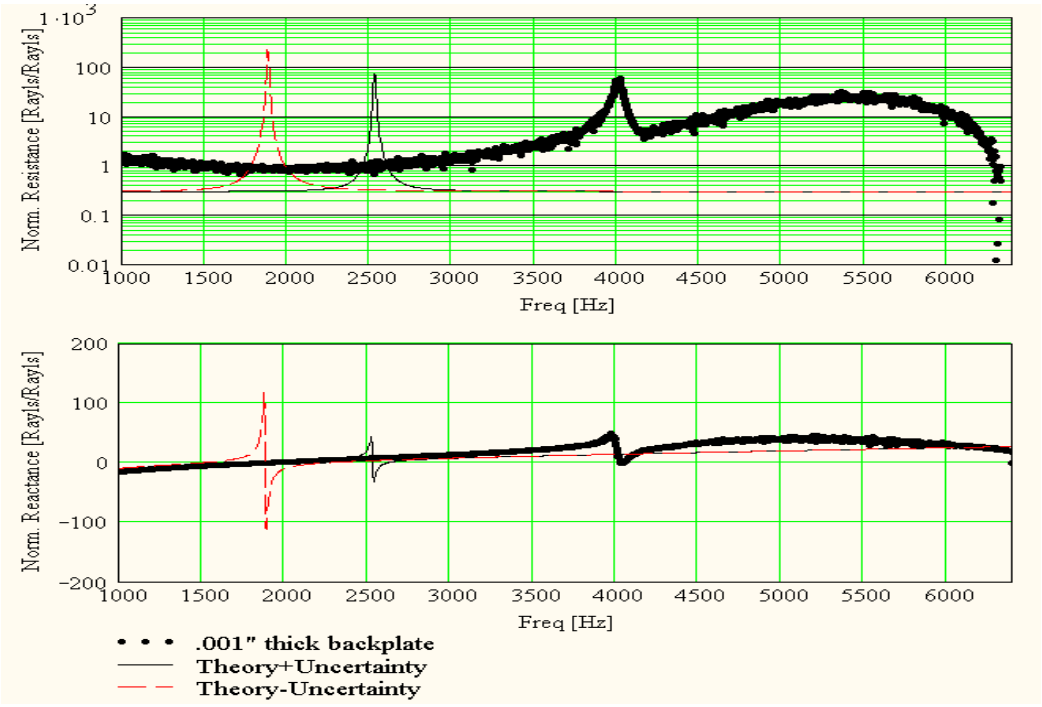

Figure 50: Normalized resistance and reactance for Helmholtz resonator with 0.001 in., stainless steel backplate clamped at 0.5 in. diameter.

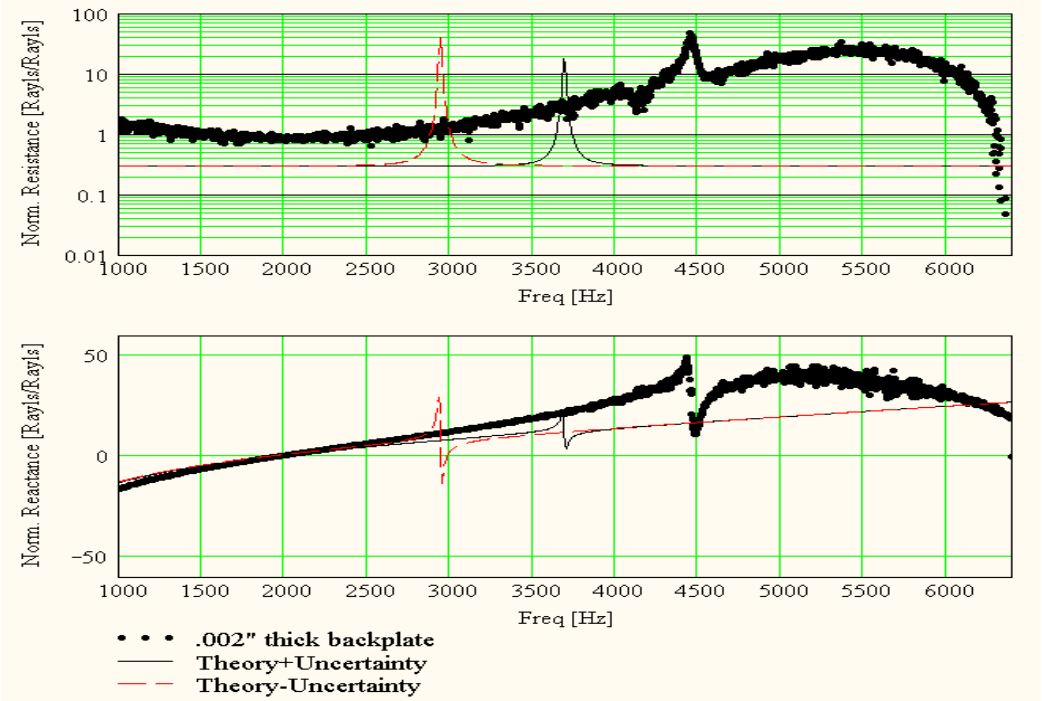

Figure 51: Normalized resistance and reactance for Helmholtz resonator with 0.002 in., stainless steel backplate clamped at 0.5 in. diameter.

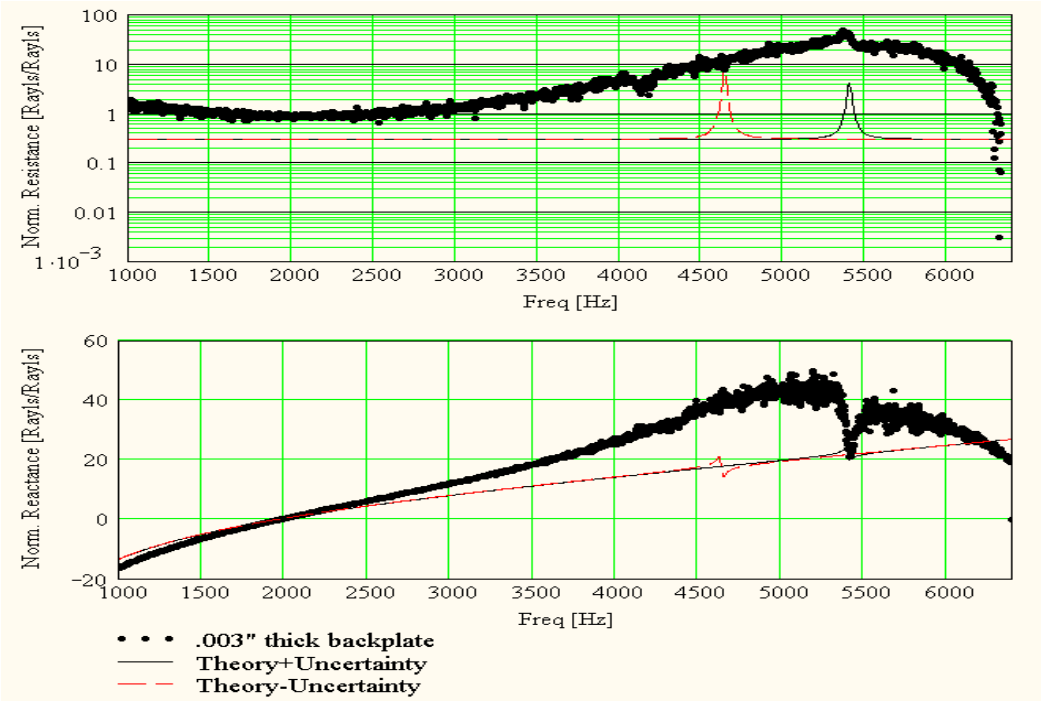

Figure 52: Normalized resistance and reactance for Helmholtz resonator with 0.003 in., stainless steel backplate clamped at 0.5 in. diameter.

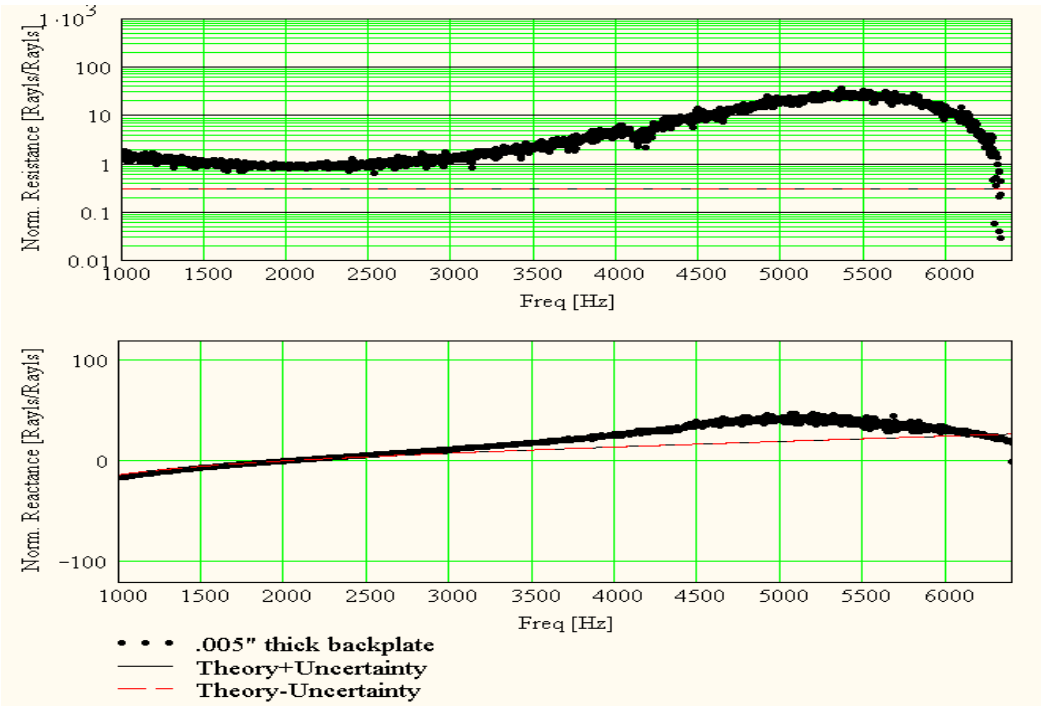

Figure 53: Normalized resistance and reactance for Helmholtz resonator with 0.005 in., stainless steel backplate clamped at 0.5 in. diameter.

Helmholtz Resonator with One-Inch Diameter, Clamped Backplates

Impedance measurements were also obtained for the 12 configurations that were clamped at 1 in. diameter and are shown in Figure 54 through Figure 65. The impedance data for each configuration is shown in terms of resistance (real) and reactance (imaginary) components.

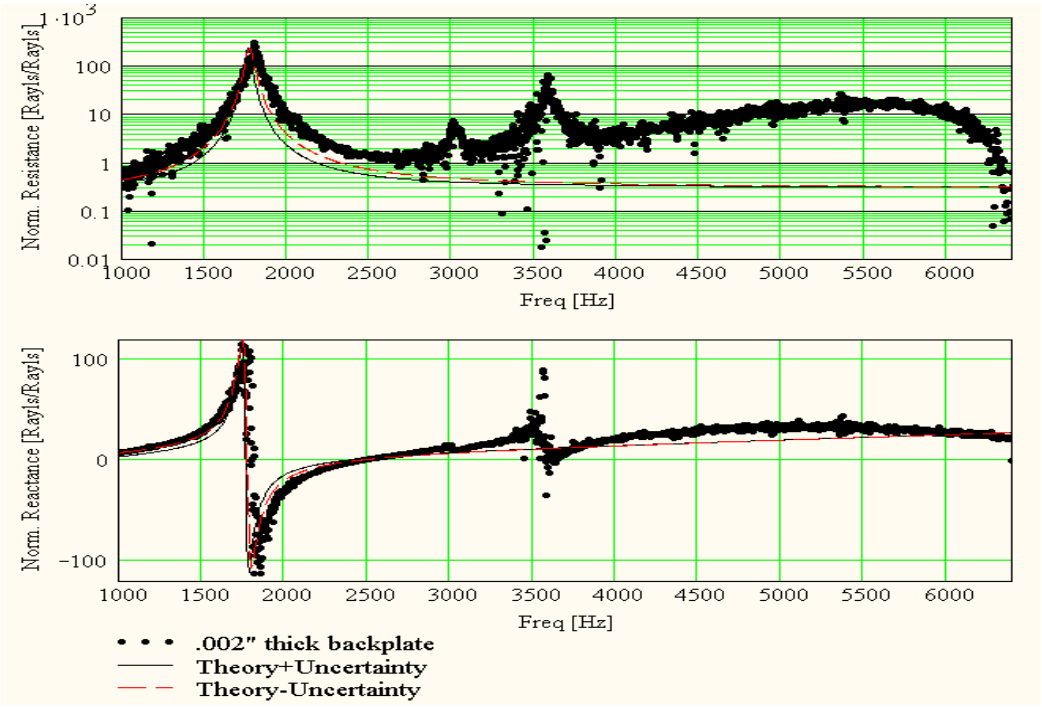

Figure 54: Normalized resistance and reactance for Helmholtz resonator with 0.002 in. aluminum backplate clamped at 0.96 in. diameter.

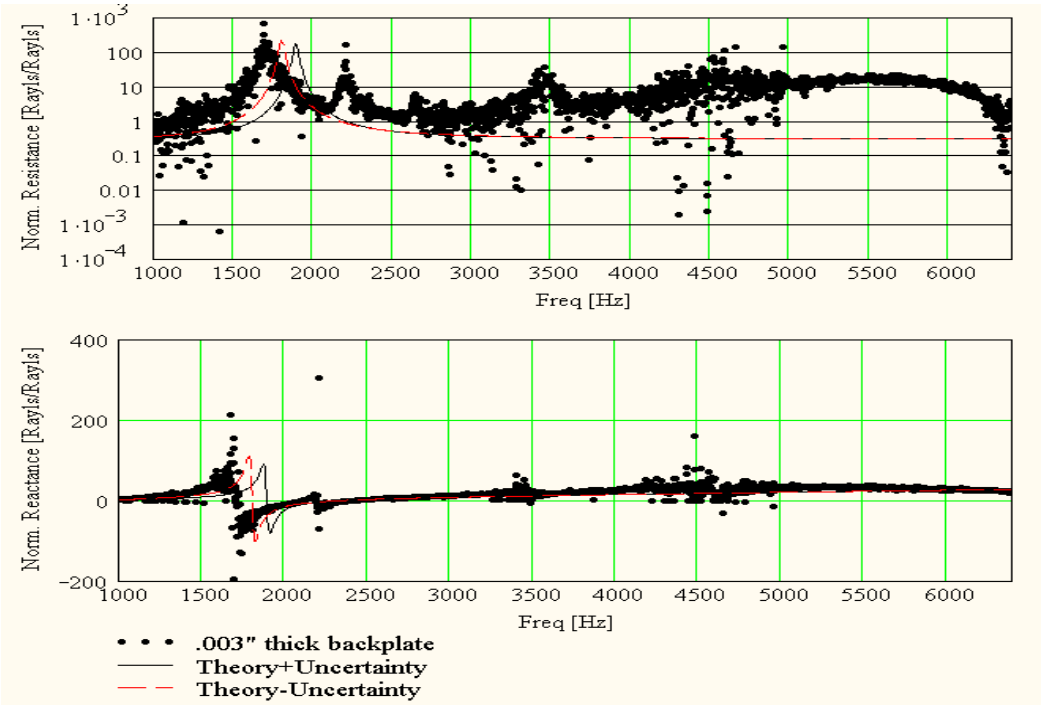

Figure 55: Normalized resistance and reactance for Helmholtz resonator with 0.003 in. aluminum backplate clamped at 0.96 in. diameter.

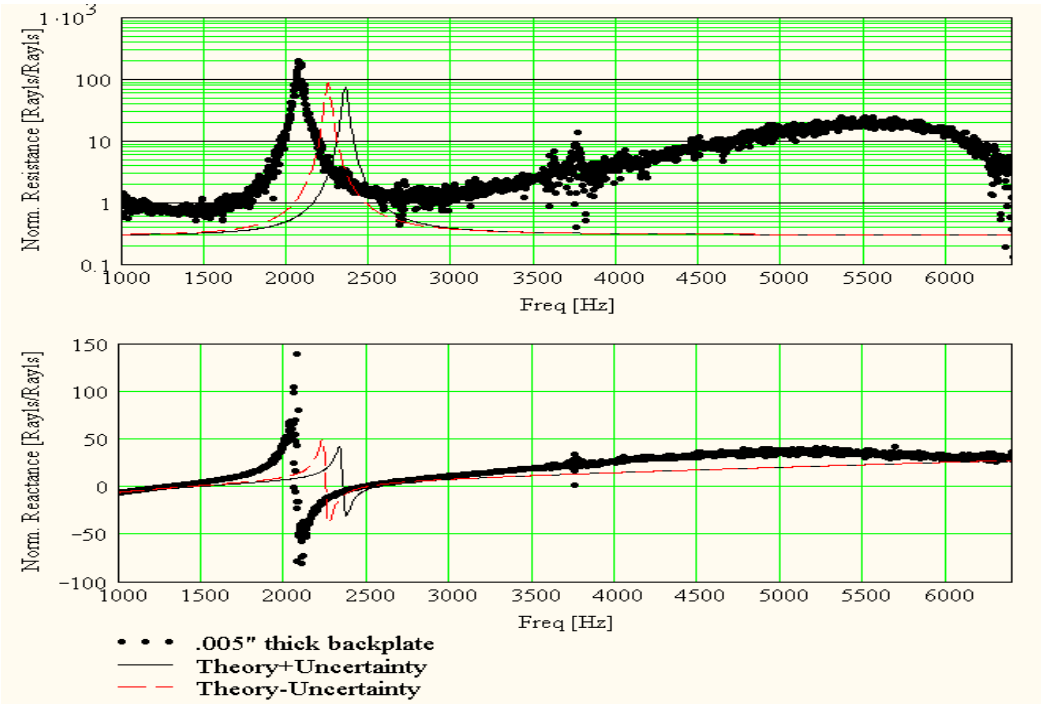

Figure 56: Normalized resistance and reactance for Helmholtz resonator with 0.005 in. aluminum backplate clamped at 0.96 in. diameter.

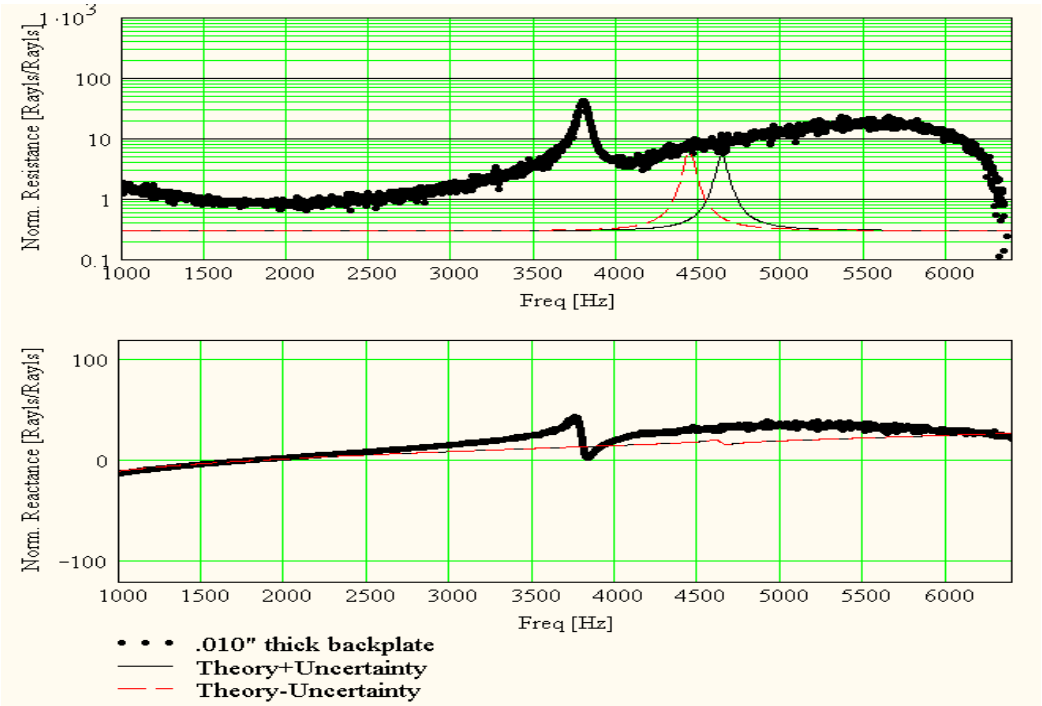

Figure 57: Normalized resistance and reactance for Helmholtz resonator with 0.010 in. aluminum backplate clamped at 0.96 in. diameter.

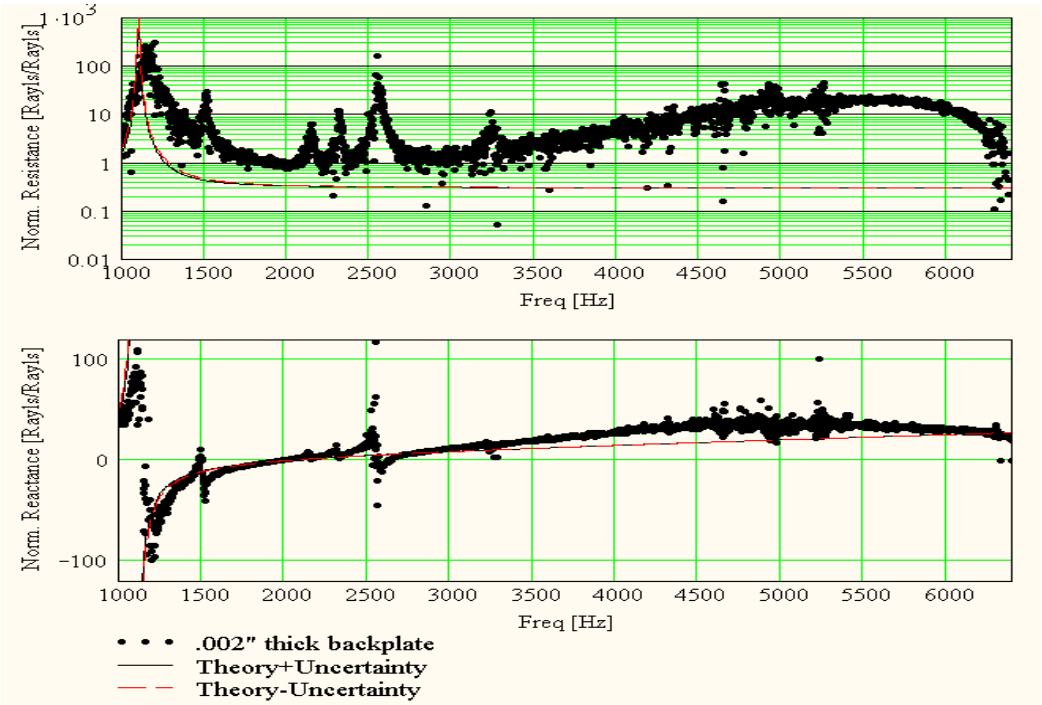

Figure 58: Normalized resistance and reactance for Helmholtz resonator with 0.002 in. brass backplate clamped at 0.96 in. diameter.

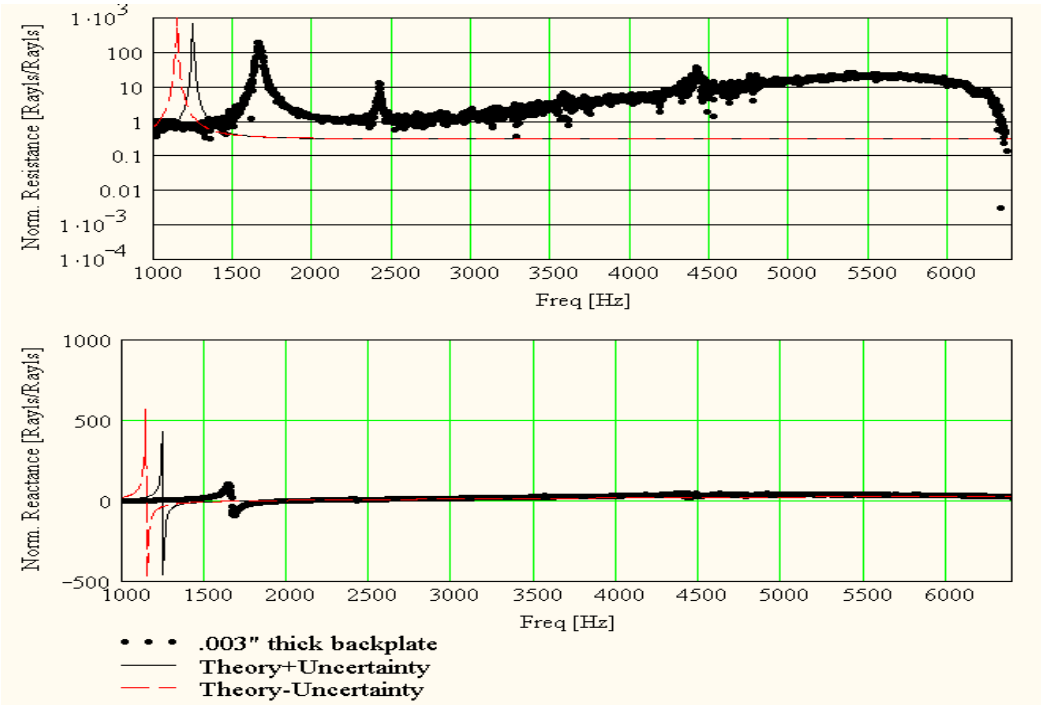

Figure 59: Normalized resistance and reactance for Helmholtz resonator with 0.003 in. brass backplate clamped at 0.96 in. diameter.

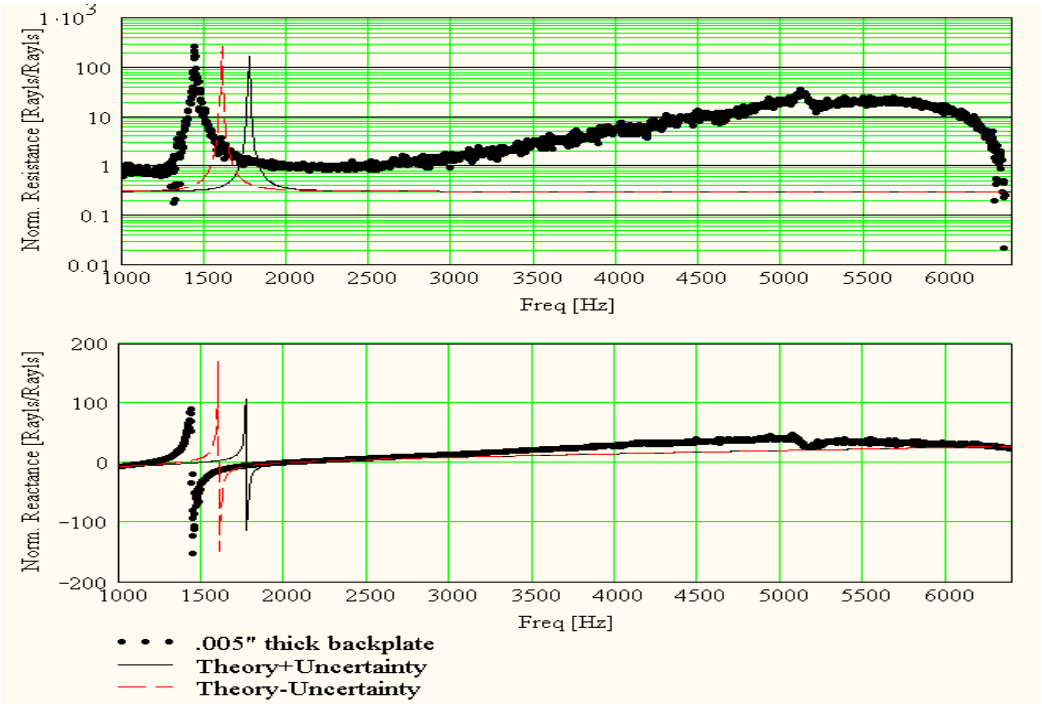

Figure 60: Normalized resistance and reactance for Helmholtz resonator with 0.005 in. brass backplate clamped at 0.96 in. diameter.

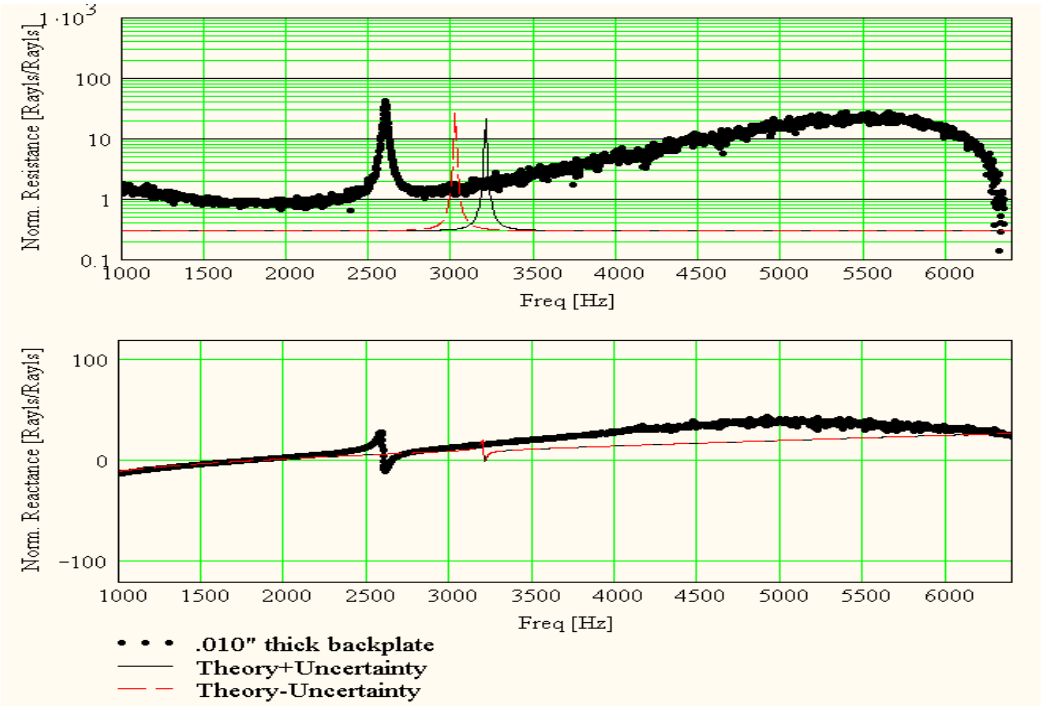

Figure 61: Normalized resistance and reactance for Helmholtz resonator 0.010 in., brass backplate clamped at 0.96 in. diameter.

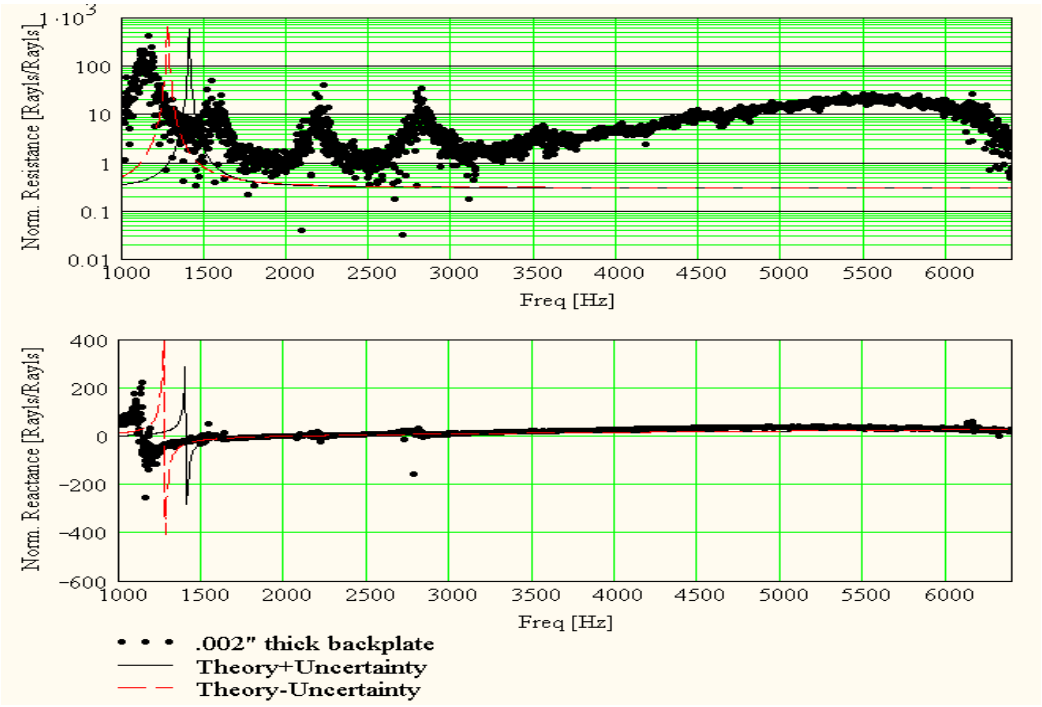

Figure 62: Normalized resistance and reactance for Helmholtz resonator with 0.002 in., stainless steel backplate clamped at 0.96 in. diameter.

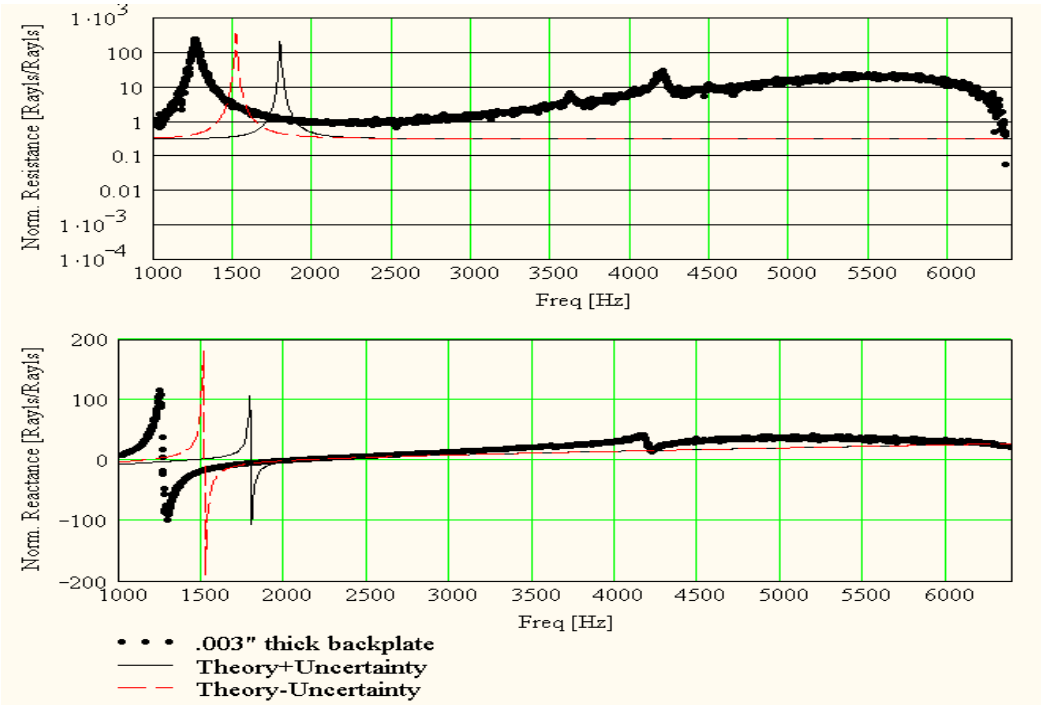

Figure 63: Normalized resistance and reactance for Helmholtz resonator with 0.003 in., stainless steel backplate clamped at 0.96 in. diameter.

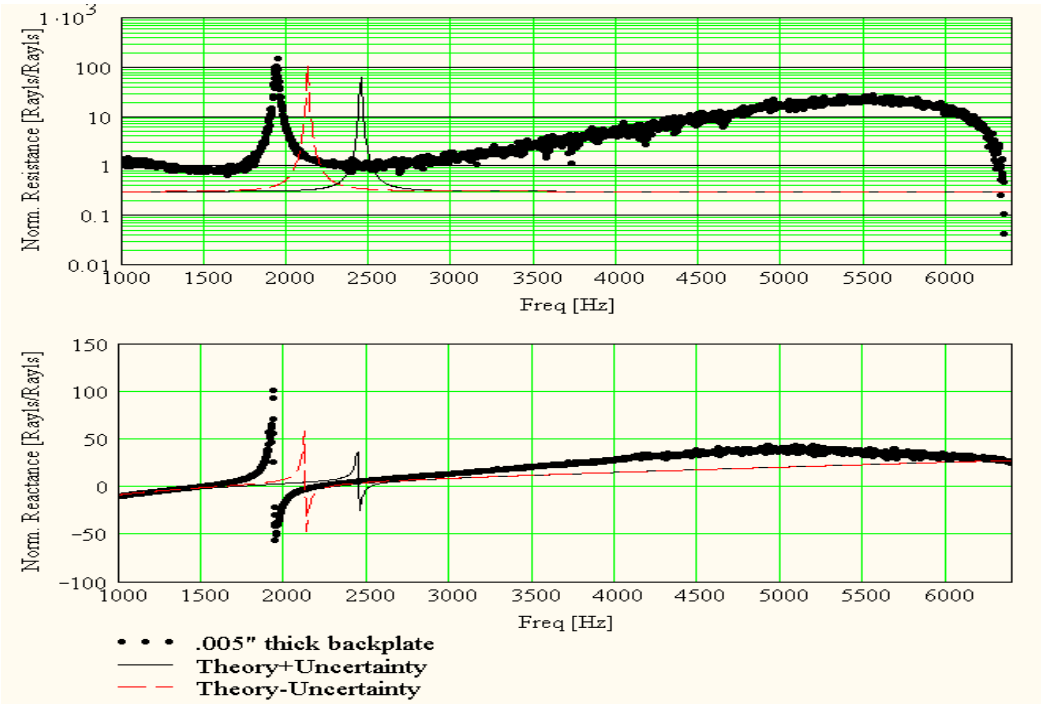

Figure 64: Normalized resistance and reactance for Helmholtz resonator with 0.005, stainless steel backplate clamped at 0.96 in. diameter.

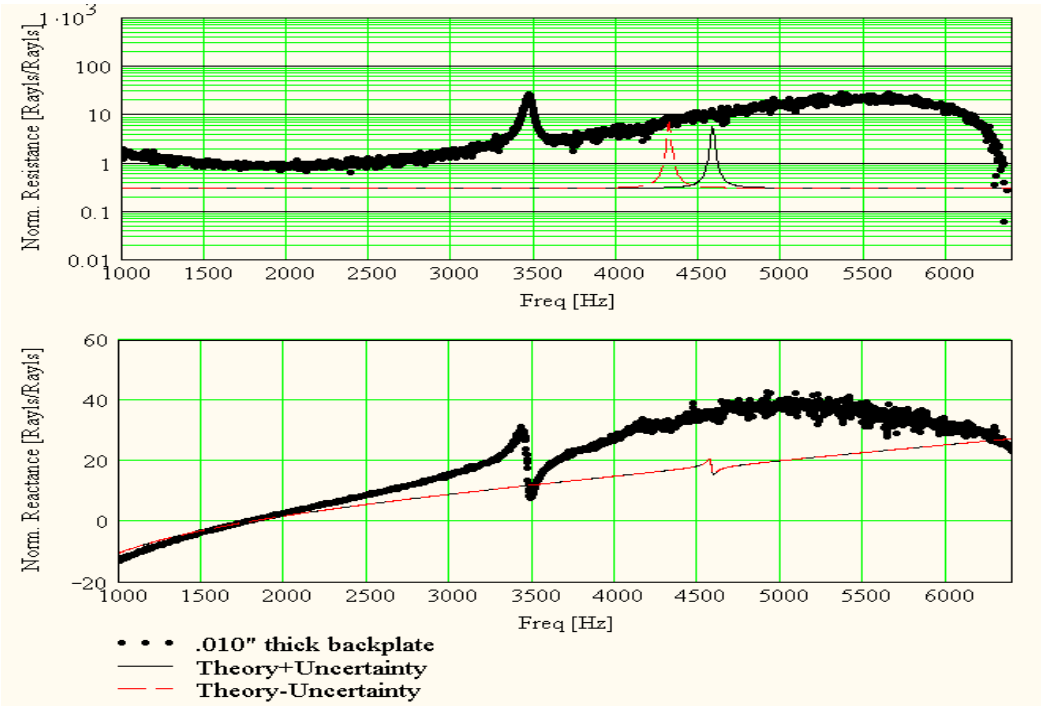

Figure 65: Normalized resistance and reactance for Helmholtz resonator with 0.010 in., stainless steel backplate clamped at 0.96 in. diameter.

Discussion of Results

For all 24 configurations tested, the measured specific acoustic impedance at the input to the Helmholtz resonator was consistent with the pressure amplification measurements. In other words, the reactance consistently passed through zero, as expected, at the same frequency as a resonant peak in the corresponding pressure amplification spectrum. Furthermore, the reactance reached a maximum, as expected, at the same frequency as a measured anti-resonance in the corresponding pressure amplification spectrum. This serves as further reassurance of the measurements, as both types of measurements were obtained from different sets of microphones and computed using different algorithms.

Some of the second resonant peaks were not clearly seen as a zero crossing in the reactance. Occasionally, a significant drop in the reactance was seen, at this frequency, but did not cross zero. This is believed to be due to the proximity of this resonance to the anti-resonance and the limited frequency resolution of the measurements. The approach of the reactance towards infinity followed closely in frequency by the rise from negative infinity through zero proved difficult to measure explicitly, although the general trend is visible in all measurements.

The microphone measurements used to obtain the impedance data exhibited good coherence for all backplates tested. All of this coherence data was measured to be above 0.9. Shown in Figure 66 is a graph of the coherence between the two microphones in the rotating plug when the Helmholtz resonator with a 0.001 in. thick aluminum backplate was mounted to the termination of the impedance tube.

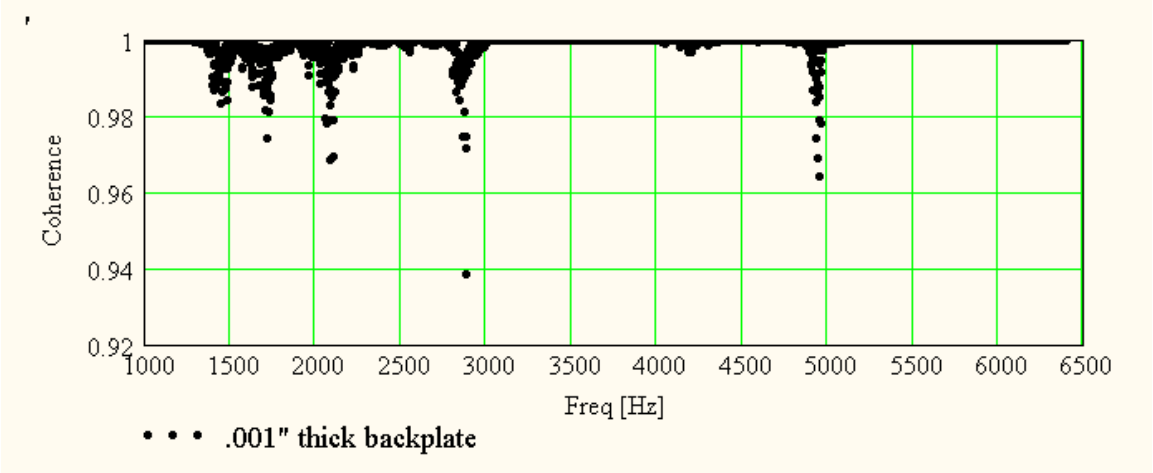

Figure 66: Coherence between rotating microphones for Helmholtz resonator with 0.001 in. thick aluminum backplate clamped at 0.5 in. diameter.

Low-Frequency Mode Shapes

The mode shapes of one set of clamped circular backplates, as measured by a laser vibrometer, is shown in Figure 67. The figure shows normalized deflection as a function of normalized radius. The backplates tested had a clamped diameter of .5 in., ranged in thickness from .001 in. to .005 in. and were all made of aluminum. The mode shape was measured with a sinusoidal acoustic signal of 125dBSPL in the cavity at a frequency of 1000Hz.

The measured mode shapes were seen to match fairly well to predictions for a static clamped circular plate, thus verifying proper clamping and plate behavior. The agreement between the theoretical mode shape of clamped circular plate and the measured mode shapes validate the use of a clamped circular plate model in the lumped element theory. The mode shape measurements, shown above, were not repeated for all 24 backplates, however all backplates were clamped usually a common method, and similar results are expected.

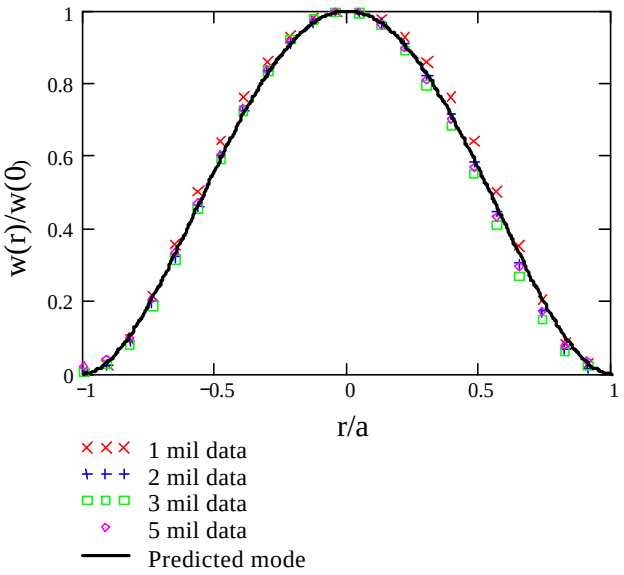

Figure 67: Measured mode shapes for each backplate along with a theoretical mode shape for a clamped circular plate, as given by Equation 2.10.

CHAPTER 5
CONCLUSION

Summary of Results

An analytical, lumped-element model was developed for a compliant-backplate Helmholtz resonator. A prototype Helmholtz resonator was constructed and characterized. Pressure amplification and normal-incidence acoustic impedance measurements were taken with 24 different compliant backplates. The impedance characterization serves as a basis for the design of a tunable Helmholtz resonator, using a piezoelectric-composite plate in place of the isotropic plates presented in this thesis.

A quantitative deviation between the analytical models and the experimental work did exist, due to unintended in-plane tension, and the presence of higher-order modes. However, the overall qualitative behavior of the compliant-backplate Helmholtz resonator was well predicted with theory. The interaction between the acoustic and mechanical elements of the compliant-backplate Helmholtz resonator followed the general trends predicted by the lumped element models despite differences in the absolute frequency of mechanical resonance.

The quantitative differences were believed to be due to several factors. First, the actual thickness of the compliant backplates was difficult to obtain accurately. Over the surface of one of the “1 mil” plates, for example, the thickness was measured at various

locations from anywhere between 0.001 in. and 0.0015 in.. To improve the estimate of the thickness, measurements were taken at several locations on the surface and averaged. Besides inaccuracies in the thickness, other factors may have contributed. Inadvertent in-plane tension as a result of the clamping configuration is believed to be increasing the stiffness. The presence of damage to the plates, near the screw holes, and the continual increase in resonant frequency with applied torque to the screws indicates this is a factor.

Future Work

The work performed to-date focused on the analytical development and experimental verification of Helmholtz resonators possessing a compliant cavity wall. To avoid the issue of in-plane tension, a new design for the clamping setup is necessary. Careful consideration of the design is required to ensure that only normal forces are applied to the boundary of the plate. Future work, beyond the redesign of the clamping setup, will seek to extend this knowledge towards an electromechanical acoustic liner capable of impedance tuning. To achieve this goal, a rigorous analytical model of a piezoelectric-composite clamped circular plate is currently under development. Optimal designs based on this analysis will then be constructed. An appropriate tunable electrical network will then be connected to the plate for tuning the impedance. Impedance tests will then proceed to characterize the impedance tuning range of the constructed devices. Pending success with these devices, an array of them can be constructed to create the electromechanical liner.

APPENDIX A
DRAWINGS

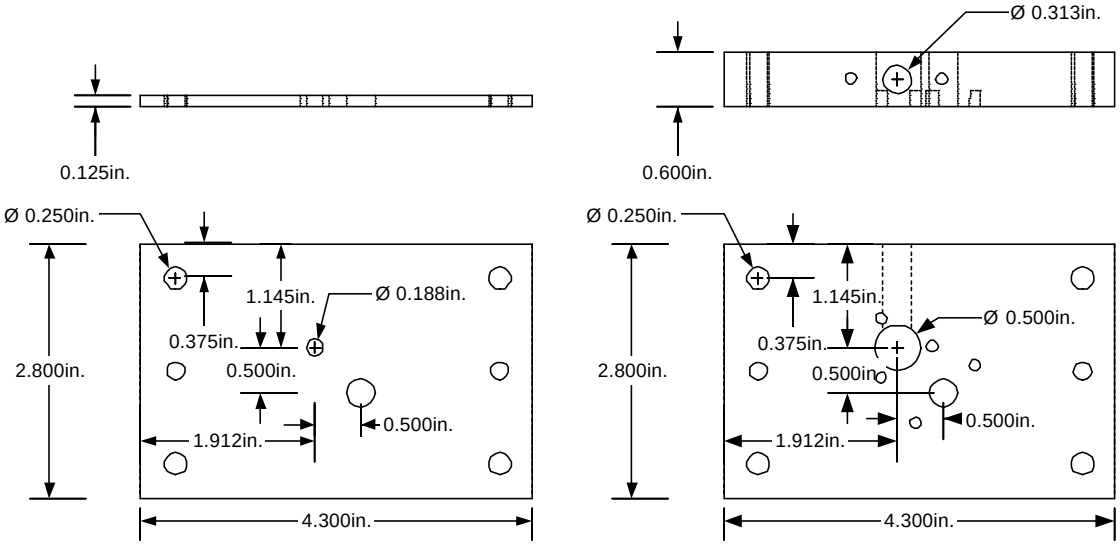

Figure 68 : Schematic of neck and cavity plate for 0.5 in. diameter compliant backplate Helmholtz resonator.

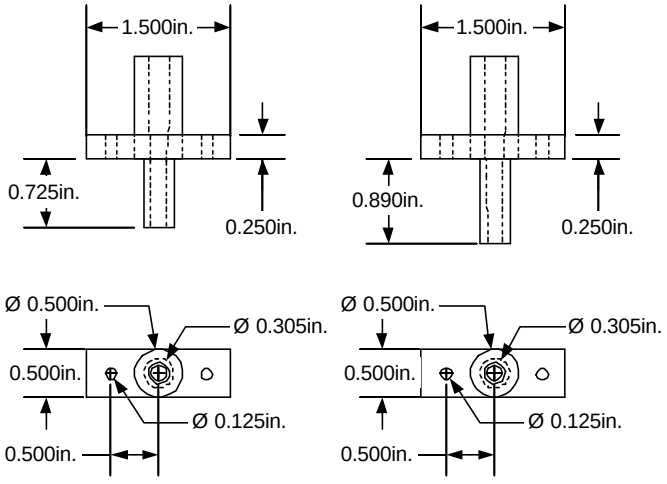

Figure 69: Schematic of incident microphone (Left) and cavity microphone (Right).

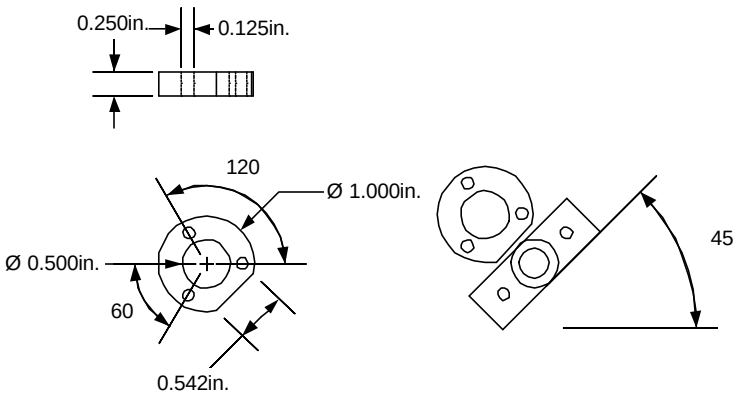

Figure 70: Schematic of 0.5 in. clamping ring and placement of clamping ring with incident microphone.

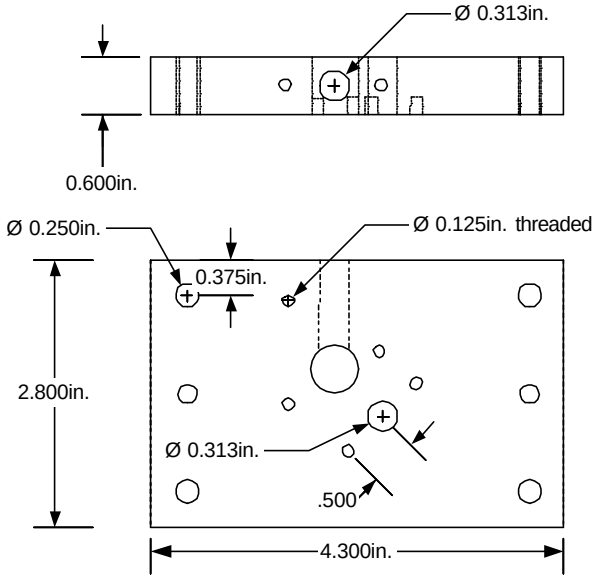

Figure 71: Schematic of cavity plate for 0.96 in. diameter compliant backplate Helmholtz resonator.

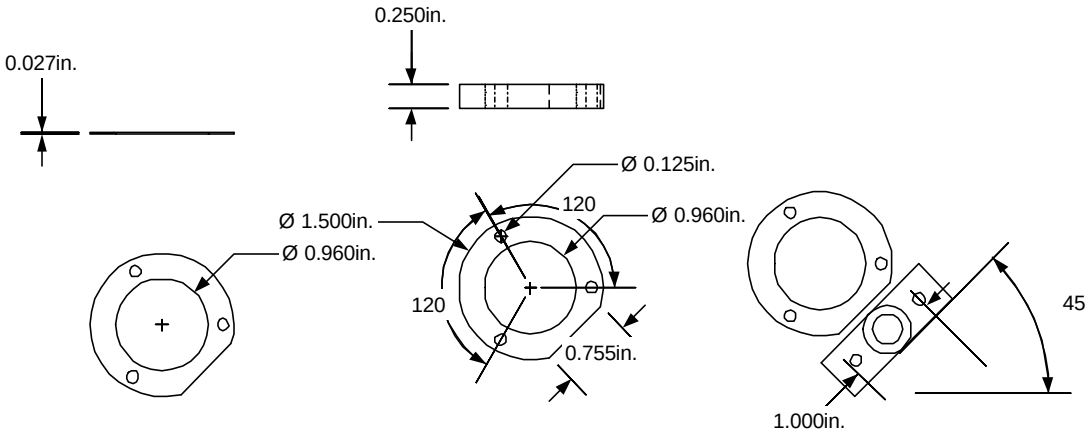

Figure 72: Schematic of spacer ring, clamping ring, and placement of rings relative to incident microphone for 0.96 in. diameter compliant backplate Helmholtz resonator.

APPENDIX B
MATHCAD CODE

Constants

$\rho := 1.165 \cdot \frac{kg}{m^3}$ air density $\quad c := 344 \cdot \frac{m}{s}$ air sound speed

$\mu := 1.789 \cdot 10^{-5} \cdot \frac{kg}{m \cdot s}$ viscosity

$\nu_{poisson} := .33 \quad E_d := 69 \cdot 10^9 \, Pa \quad \rho_d := 2.71 \cdot \frac{gm}{(cm)^3}$ aluminum diaphragm

$\nu_{poisson} := .324 \quad E_d := 103 \cdot 10^9 \, Pa \quad \rho_d := 8.47 \cdot \frac{gm}{(cm)^3}$ brass diaphragm

$\nu_{poisson} := .3 \quad E_d := 1.93 \cdot 10^{11} \, Pa \quad \rho_d := 7.86 \cdot \frac{gm}{(cm)^3}$ stainless steel diaphragm

Impedance Tube

$Atube := 1 \, in \cdot 1 \, in$ area of tube

$Ztube := \frac{\rho \cdot c}{Atube} \quad Ztube = 6.212 \cdot 10^5 \, \frac{kg}{m^4 \cdot s}$ acoustic impedance of tube

Resonator Neck

$L := .123 \cdot in$ length of neck $\quad d_{neck} := .186 \, in$

$a_{neck} := \frac{d_{neck}}{2}$ neck radius $\quad a_{neck} = 2.362 \cdot mm \quad Area_{neck} := a_{neck}^2 \cdot \pi$

$Leff := L + 1.6 \cdot a_{neck} \quad Leff = 6.904 \cdot mm$ effective length of neck

Resonator Cavity

$d_{cavity} := .501 \, in \quad a_{cavity} := \frac{d_{cavity}}{2} \quad a_{cavity} = 0.25 \cdot in$ radius of cavity

$depth := .602\,in$ $depth = 15.291\,mm$ depth of cavity

$SpacerHeight := .00\,in$ $SpacerRad := \frac{.96}{2}\,in$ spacers for 1" backplate only

$ExtraV := SpacerHeight \cdot \pi \cdot SpacerRad^2$

$Area_{cavity} := \pi \cdot a_{cavity}^2$ $Area_{cavity} = 127.184\,mm^2$

$Volume := \pi \cdot \left(a_{cavity}^2 \cdot depth\right) + ExtraV$ $Volume = 1.945 \cdot 10^3\,mm^3$ volume of cavity

Resonator Backplate

$radius := \frac{.501}{2}\,in$ radius of clamped boundary for backplate

Lumped Element Models - Acoustic Components

$M_A(radius) := \frac{\rho \cdot Leff}{\pi \cdot a_{neck}^2}$ $M_A(.5\,in) = 458.803\,\frac{kg}{m^4}$ acoustic mass of neck

$C_a(radius) := \frac{Volume}{\rho \cdot c^2}$ $C_a(.5\,in) = 1.411 \cdot 10^{-11}\,\frac{m^4 \cdot s^2}{kg}$ acoustic compliance of cavity

$f_{res}(radius) := \frac{1}{2 \cdot \pi \cdot \sqrt{M_A(radius) \cdot C_a(radius)}}$ $f_{res}(2) = 1.978 \cdot 10^3\,Hz$ resonance frequency

$R_a(radius) := \frac{40 \cdot 8 \cdot \mu \cdot L}{\pi \cdot a_{neck}^4}$ $R_a(.5\,in) = 1.828 \cdot 10^5\,\frac{kg}{m^4 \cdot s}$ acoustic resistance of neck (viscous)

$A_{eff}(radius) := \frac{1}{3} \cdot \pi \cdot radius^2$ effective area of a/m xduction

Lumped Element Models - Mechanical Components

$M_m(thick, radius) := \frac{\pi \cdot (radius)^2 \cdot (thick) \cdot \rho_d}{5 \cdot \left(A_{eff}(radius)\right)^2}$ mechanical mass of backplate

$C_m(thick, radius) := \frac{\overrightarrow{9 \cdot (radius)^2 \cdot \left(1 - \nu_{poisson}^2\right) \cdot \left(A_{eff}(radius)\right)^2}}{16 \cdot \pi \cdot E_d \cdot ((thick))^3}$ mechanical compliance of backplate

Equivalent Circuit

Input Impedance

$$Zin(s, thick, radius) := \frac{\left\{s \cdot M_m(thick, radius) + \frac{1}{s \cdot C_m(thick, radius)}\right\} \cdot \left\{\frac{1}{s \cdot C_a(radius)}\right\}}{s \cdot M_m(thick, radius) + \frac{1}{s \cdot C_m(thick, radius)} + \left\{\frac{1}{s \cdot C_a(radius)}\right\}} + \left(s \cdot M_A(radius) + R_a(radius)\right)$$

Pressure Amplification

$$PA(s, thick, radius) := \frac{\left\{\frac{1}{s \cdot C_a(radius)}\right\}}{Zin(s, thick, radius)} \cdot \left[\frac{s \cdot M_m(thick, radius) + \frac{1}{s \cdot C_m(thick, radius)}}{s \cdot M_m(thick, radius) + \frac{1}{s \cdot C_m(thick, radius)} + \left\{\frac{1}{s \cdot C_a(radius)}\right\}}\right]$$

Backplate Deflection

$$W(P, s, thick, radius) := \frac{P \cdot PA(s, thick, radius)}{s \cdot \left\{s \cdot M_m(thick, radius) + \frac{1}{s \cdot C_m(thick, radius)}\right\} \cdot A_{eff}(radius)}$$

Normalized Backplate Deflection

$$W_{norm}(s, thick, radius) := \frac{1}{s \cdot \left\{s \cdot M_m(thick, radius) + \frac{1}{s \cdot C_m(thick, radius)}\right\} \cdot A_{eff}(radius)}$$

Reflection coefficient

$$r(s, thick, radius) := \frac{Zin(s, thick, radius) - Ztube}{Zin(s, thick, radius) + Ztube}$$

Absorption coefficient

$$alpha(s, thick, radius) := 4 \cdot \frac{\left\{\frac{Re(Zin(s, thick, radius))}{Ztube}\right\}}{\left\{\frac{Re(Zin(s, thick, radius))}{Ztube} + 1\right\}^2 + \left\{\frac{Im(Zin(s, thick, radius))}{Ztube}\right\}^2}$$

LIST OF REFERENCES

[1] R. E. Motsinger and R. E. Kraft, "Design and Performance of Duct Acoustic Treatment," in *Aeroacoustics of Flight Vehicles: Theory and Practice, Volume 2: Noise Control*, H. H. Hubbard, Ed.: NASA Reference Publication 1258, 1991, pp. 165-206.

[2] H. W. Kwan, "Bias Flow Adaptive Acoustic Liner Program Review," NASA-LaRC, 1998.

[3] J. F. Betts, J. I. Follet, J. Kelly, and H. Wood, "An Improved Impedance Model for Perforates Including the Effect of Bias Flow," presented at 39th AIAA Aerospace Sciences Meeting and Exhibit, Reno, NV, 2001.

[4] G. W. Bielak, J. W. Premo, and A. S. Hersh, "Advanced Turbofan Duct Liner Concepts," NASA-LaRC NASA/CR-1999-209002, 1999.

[5] G. Bielak and J. Premo, "Boeing Impedance Model for Perforates with Extension to Bias Flow," . NASA AST Lining Workshop, 1999.

[6] W. R. Watson, S. E. Tanner, and T. L. Parrott, "Optimization Method for Educing Variable-Impedance Liner Properties," *AIAA Journal*, vol. 36, pp. 18-23, 1998.

[7] J. M. de Bedout, Franchek, M.A., Bernhard, R.J., Mongeau, L., "Adaptive-Passive Noise Control with Self-Tuning Helmholtz Resonators," *Journal of Sound and Vibration*, vol. 202, pp. 109-123, 1997.

[8] H. Matsuhisa, Ren, B., "Semiactive Control of Duct Noise by a Volume-Variable Resonator," *JSME International Journal*, vol. 35, pp. 223-228, 1992.

[9] R. E. Kraft, B. A. Janardan, G. C. Kontos, and P.R.Gliebe, "Active Control of Fan Noise-Feasiblity Study, Volume 1: Flyover System Noise Studies," NASA - Lewis Research Center NASA CR-195392, 1994.

[10] A. S. Hersh and B. Walker, "Fluid Mechanical Model of the Helmholtz Resonator," NASA Contractor Report NASA CR-2904, 1977.

[11] A. P. Dowling and J. E. FFowcs Williams, *Sound and Sources of Sound*. Chichester, Eng.: Ellis Horwood Limited, 1983.

[12] J. F. Lindsay and S. Katz, *Dynamics of Physical Circuits and Systems*. Champaign, Illinois: Matrix Publishers, Inc., 1978.

[13] M. Rossi, *Acoustics and Electroacoustics*. Norwood, MA: Artech House, 1988, pp. 245-308.

[14] F. V. Hunt, *Electroacoustics: The Analysis of Transduction, and Its Historical Background*. New York, NY: Acoustical Society of America, 1982.

[15] D. T. Blackstock, *Fundamentals of Physical Acoustics*. New York, NY: John Wiley & Sons, Inc., 2000.

[16] W. T. Chu, "Extension of the Two-Microphone Transfer Function Method for Impedance Tube Measurements," *Journal of the Acoustical Society of America*, vol. 80, pp. 347-349, 1986.

[17] J. Y. Chung and D. A. Blaser, "Transfer Function Method of Measuring In-Duct Acoustic Properties. I. Theory," *Journal of the Acoustical Society of America*, vol. 68, pp. 907-921, 1980.

[18] M. G. Jones and P. E. Stiede, "Comparison of Methods for Determining Specific Acoustic Impedance," *Journal of the Acoustical Society o f America*, vol. 101, pp. 2694-2704, 1997.

[19] ASTM, "Standard Test Method for Impedance and Absorption of Acoustical Materials Using a Tube, Two Microphones, and a Digital Frequency Analysis System," ASTM E 1050-90, 1990.

[20] M. G. Jones and T. L. Parrott, "Evaluation of a Multi-Point Method for Determining Acoustic Impedance," *Mechanical Systems and Signal Processing*, vol. 3, pp. 15-35, 1989.

[21] W. T. Chu, "Transfer Function Technique for Impedance and Absorption Measurements in an Impedance Tube Using a Single Microphone," *Journal of the Acoustical Society of America*, vol. 80, pp. 555-560, 1986.

[22] Polytec-PI, *Operator's Manual for Polytec Scanning Vibrometer PSV-200*.

[23] H. W. Coleman and W. G. Steele, *Experimentation and Uncertainty Analysis for Engineers*, 2nd Edition ed. New York, NY: John Wiley & Sons, Inc., 1999.

BIOGRAPHICAL SKETCH

Stephen Brian Horowitz was born on August 3, 1977, in Pompton Plains, N.J. He attended Marjory Stoneman Douglas High School in Parkland, FL, graduating in 1995. He received his bachelor's degree in electrical engineering from the University of Florida in 1999. He is currently working towards his Master of Science degree in electrical engineering at the University of Florida. He plans to continue towards a doctoral degree at the University of Florida, concentrating his research efforts in the area of micro-electro-mechanical systems (MEMS).